Schriften des Forschungszentrums Jülich
Reihe Energie & Umwelt / Energy & Environment Band / Volume 202

Forschungszentrum Jülich GmbH
Institute of Bio- and Geosciences (IBG)
Agrosphere (IBG-3)

Full-waveform inversion of surface ground penetrating radar data and coupled hydrogeophysical inversion for soil hydraulic property estimation

Sebastian Busch

Schriften des Forschungszentrums Jülich
Reihe Energie & Umwelt / Energy & Environment Band / Volume 202

ISSN 1866-1793 ISBN 978-3-89336-930-0

Bibliographic information published by the Deutsche Nationalbibliothek.
The Deutsche Nationalbibliothek lists this publication in the Deutsche Nationalbibliografie; detailed bibliographic data are available in the Internet at http://dnb.d-nb.de.

Publisher and Distributor: Forschungszentrum Jülich GmbH
Zentralbibliothek
52425 Jülich
Tel: +49 2461 61-5368
Fax: +49 2461 61-6103
Email: zb-publikation@fz-juelich.de
www.fz-juelich.de/zb

Cover Design: Grafische Medien, Forschungszentrum Jülich GmbH

Printer: Grafische Medien, Forschungszentrum Jülich GmbH

Schriften des Forschungszentrums Jülich
Reihe Energie & Umwelt / Energy & Environment, Band / Volume 202

D 82 (Diss.,RWTH Aachen University, 2013)

ISSN 1866-1793
ISBN 978-3-89336-930-0

The complete volume is freely available on the Internet on the Jülicher Open Access Server (JUWEL) at www.fz-juelich.de/zb/juwel

This dissertation is based on following manuscripts, which are submitted to or already published by scientific journals:

Busch, S., J. van der Kruk, J. Bikowski, and H. Vereecken, 2012, Quantitative conductivity and permittivity estimation using full-waveform inversion of on-ground GPR data, Geophysics, 77, H79–H91, doi: 10.1190/GEO2012-0045.1.
Contribution: full-waveform inversion for the analysis of reflected waves; effective source wavelet estimation; combined sequential and simultaneous model and wavelet optimization; application to synthetic and measured CMP data.

Busch, S., J. van der Kruk, and H. Vereecken, 2012, Improved characterization of fine texture soils using on-ground GPR full-waveform inversion, IEEE Transactions on Geoscience and Remote Sensing, accepted, doi: 10.1109/TGRS.2013.2278297.
Contribution: full-waveform inversion for the analysis of the direct ground wave; airwave filtering; combined geophysical measurements; interpretation and correlation of the results.

Busch, S., L. Weihermüller, J. A. Huisman, C. M. Steelman, A. L. Endres, H. Vereecken, and J. van der Kruk, 2013, Coupled hydrogeophysical inversion of time-lapse surface GPR data to estimate hydraulic properties of a layered subsurface, Water Resources Research, accepted.
Contribution: coupled hydrogeophysical inversion; application to synthetic and measured data; interpretation of the results.

Kalogeropoulos, A., J. van der Kruk, J. Hugenschmidt, S. Busch, and K. Merz, 2011, Chlorides and moisture assessment in concrete by GPR full-waveform inversion: Near Surface Geophysics, 9, 277–285.
Contribution: off-ground GPR methodology as outlook to further applications.

Table of Contents

Kurzfassung

Die Verwendung elektromagnetischer Verfahren zur zerstörungsfreien Untersuchung gewinnt zunehmend an Bedeutung, insbesondere in der Ingenieursgeophysik, im Bauwesen, in den Umweltwissenschaften sowie bei hydrologischen Fragestellungen. Eine Vielzahl von geophysikalischen Methoden ermöglicht dabei die Bestimmung wichtiger Materialeigenschaften. Durch das Monitoring oberflächennaher Bodenschichten können zudem Aussagen über den Wassergehalt und die hydraulischen Parameter des Bodens gemacht werden, die für das Verständnis der dynamischen hydrologischen Prozesse von großer Bedeutung sind.

Die herkömmliche Berechnung des Bodenwassergehaltes basiert auf der Permittivität, der elektrischen Leitfähigkeit des Untergrundes und dem petrophysikalischen Complex Refractive Index Model (CRIM) oder den empirischen Topp's und Archie Gleichungen. Eine schnelle und effektive Bestimmung der Permittivität und der Leitfähigkeit ermöglicht insbesondere das Bodenradar (GPR) in Verbindung mit strahlen-basierten Auswerte-verfahren. Da diese Verfahren nur Teilinformationen des gemessenen GPR-Signals sowie ein vereinfachtes Modell der Wellenausbreitung verwenden, sind insbesondere die elektrischen Eigenschaften nicht repräsentativ für den Boden. Im Gegensatz zu den strahlen-basierten Verfahren werden bei der Inversion des gesamten Wellenfeldes (FWI, Full-waveform inversion) alle Informationen in den Daten sowie ein exaktes Modell der elektromagnetischen Wellenausbreitung für die Bestimmung quantitativer Permittivitäts- und Leitfähigkeitswerte verwendet.

Ziel der vorliegenden Arbeit ist die Entwicklung einer Wellenfeld Inversion für das Bodenradar zur Bestimmung quantitativer Permittivitäts- und Leifähigkeitswerte. Das Verfahren basiert auf der exakten Lösung der Maxwell Gleichung im Frequenzbereich (Nah- bis Fernfeld) für einen geschichteten Halbraum und benötigt ein Startmodell der Bodenparameter sowie eine Abschätzung des Quellsignals (Wavelet). Obwohl die FWI weitgehend unabhängig von einem Startmodell für die Permittivität des Untergrundes ist, bewirkt ein ungenaues Startmodell der Leitfähigkeiten fehlerhafte Wavelet-Amplituden und somit eine fehlerhaftes Inversionsergebnis. Daher werden die Permittivitäten und Leitfähigkeiten zusammen mit der Phase und Amplitude des Wavelets in einem Gradienten-freien Optimierungsverfahren aktualisiert.

Die FWI wird für die Auswertung der Bodenwelle und reflektierter Wellen angewendet. Für synthetische dispersive und nicht-dispersive GPR-Daten, bei denen sich das Startmodell stark von den angenommenen Modelleigenschaften unterscheidet, konnten sowohl die Bodenparameter als auch das Wavelet rekonstruiert werden. Für gemessene dispersive GPR-Daten resultieren unterschiedliche Startmodelle in vergleichbare Bodenparameter und identische Wavelets.

Um das FWI Verfahren auch für die Charakterisierung von fein strukturierten Böden zu validieren, wurden kombinierte geophysikalische Messungen auf einem siltigen Lehm mit

einer hohen Variabilität in der Bodentextur durchgeführt. Die aus der Analyse der Bodenwelle berechneten Bodenparameter sind konsistent mit den Ergebnissen von Theta Probe, Electromagnetic Resistivity Tomography (ERT) und Electromagnetic Induction (EMI) Messungen und ermöglichen die Formulierung eines empirischen Zusammenhanges zwischen Bodentextur und Bodenparametern. Die Permittivität und Leitfähigkeit steigt mit zunehmenden Ton- und Silt- und abnehmenden Skeleton-Anteil. Entsprechend der Abstrahlungs- und Kopplungscharakteristik der GPR-Antennen nimmt die Mittenfrequenz des Wavelets mit zunehmender Permittivität und Leitfähigkeit ab während die Wavelet-Amplitude ansteigt.
Neben der quantitativen Bestimmung der Permittivität und Leitfähigkeit ermöglicht das Bodenradar auch Rückschlüsse auf die zeitlich variierende, vertikale Verteilung des Bodenwassers. Wiederholte GPR-Messungen begünstigen dabei das Abschätzen der hydraulischen Bodeneigenschaften, die für die hydrologische Parametrisierung des Bodens notwendig sind. Um GPR-für die Bestimmung hydraulischer Parameter zu nutzen, wurde im Rahmen dieser Arbeit ein kombiniertes hydrogeophysikalischen Inversionsverfahren entwickelt, das ein hydrologisches Modell des Bodens mit der Auswertung von GPR-Daten verbindet. Das Verfahren wird auf synthetische und gemessenen GPR-Daten für einen geschichteten sandigen Boden angewendet. Um nicht-kapillare Strömung unter trockenen Bedingungen zu berücksichtigen wird Filmströmung durch zwei zusätzlich Parameter in das hydrologische Modell implementiert.
Für synthetische Daten liefert das Verfahren einen hervorragenden Datenanpassung auch bei einer falschen Parametrisierung des hydrologischen Modells. Die Vernachlässigung der Filmströmungs-Parameter wird durch fehlerhafte hydraulische Parameter kompensiert. Wird Film- und Kapillarströmung berücksichtigt, können die hydraulischen Parameter eindeutig rekonstruiert werden wodurch die Bedeutung einer geeigneten Konzeptualisierung des hydrologischen Modells verdeutlicht wird.
Für gemessene GPR-Daten kann der Datenanpassung im Vergleich zu einem nicht kalibrierten Modell der hydraulischen Parameter auf Grundlage von Labordaten insbesondere für tiefer liegende Bodenschichten verbessert werden. Die Verwendung von Filmströmung in der oberflächennahe Schicht führt zu keinem besseren Inversionsergebnis. Weitere Ansätze sind notwendig um die Prozesse zu beschreiben, z.B. die Auswirkung von Wärmetransport und Wasserdampf, die den Wassergehalt unter trockenen Bedingungen beeinflussen.

Die Anwendung der neuen Wellenfeld- und kombinierten hydrogeophysikalischen Inversionen zeigen das Potential von Bodenradar Messungen zur quantitative Bestimmung von Permittivitäts- und Leitfähigkeitswerten, der Charakterisierung des dynamischen Bodenwasser und der hydraulischen Bodenparameter. Die vorgestellten Verfahren können für eine Vielzahl von Untersuchung zur verbesserten Charakterisierung des Untergrundes angewandt werden.

Abstract

Non-invasive electromagnetic methods are increasingly applied for a wide range of applications in geophysical engineering, infrastructure characterization and environmental and hydrological studies. A variety of geophysical techniques are routinely used to estimate medium properties, monitor shallow soil conditions and provide valuable estimates of soil water content and the soil hydraulic parameters needed for the understanding of the highly dynamic hydrological processes in the subsurface.

Traditionally, estimates of the soil water content are obtained using the subsurface permittivity and conductivity in combination with petrophysical relationships such as the Complex Refractive Index Model (CRIM) or empirical relationships such as Topp's equation and Archie's law. Here, especially surface ground penetrating radar (GPR) is a technique that enables a quick and effective mapping of the subsurface dielectric permittivity. Although GPR has the potential to return permittivities and conductivities for the same sensing volume at the field scale, estimates of the conductivity based on conventional ray-based techniques that only use part of the measured data and simplified approximations of the reality contain relatively large errors. Full-waveform inversion (FWI) overcomes these limitations by using an accurate forward modeling and inverts significant parts of the measured data to return reliable quantitative estimates of both permittivity and conductivity.

In this work, we introduce a novel full-waveform inversion scheme that is able to reliably estimate permittivity and conductivity values from surface GPR data. It is based on a frequency-domain solution of Maxwell’s equations including far-, intermediate- and near-fields assuming a three-dimensional, horizontally layered model of the subsurface, and requires a starting model of the subsurface properties as well as the estimation of a source wavelet. Although the full-waveform inversion is relatively independent of the permittivity starting model, inaccuracies in the conductivity starting model result in erroneous effective wavelet amplitudes and therefore in erroneous inversion results, since the conductivity and wavelet amplitudes are coupled. Therefore, the permittivity and conductivity are updated simultaneously with the phase and amplitude of the source wavelet. Here, optimizing the medium properties and reducing the misfit is carried out using a gradient free approach.

This novel FWI is applied the analysis of ground waves and reflected waves. In the case of synthetic single layered and waveguide data, where the starting model differs significantly from the true model parameter, we were able to reconstruct the obtained model properties and the effective source wavelet. For measured waveguide data, different starting values returned the same quantitative medium properties and a data-driven effective source wavelet.

To further verify the FWI for a fine texture soil, combined geophysical measurements were carried out over a silty loam with significant variability in the soil texture. Analyzing the direct ground wave, the obtained medium properties are consistent with Theta probe,

electromagnetic resistivity tomography (ERT) and electromagnetic induction (EMI) results and enable the formulation of an empirical relationship between soil texture and soil properties. The permittivities and conductivities increase with increasing clay and silt content and decreasing skeleton content. Moreover, with increasing permittivities and conductivities the wavelet center frequency shifts to lower frequencies, whereas the wavelet amplitude increases, which is consistent with radiation pattern and antenna coupling characteristics.

Besides the quantitative estimation of the subsurface permittivity and conductivity, surface GPR is also eminently suited to obtain accurate information on the temporal changes of the vertical soil water distribution. Monitoring the shallow soil conditions using time-lapse GPR measurements may provide valuable estimates of soil hydraulic parameters needed for hydrological model parameterization. To evaluate the feasibility of using surface GPR data for subsurface hydraulic parameter characterization, a coupled hydrogeophysical inversion, that combines a hydrological model of the subsurface with the analysis of GPR data, was developed and applied to a synthetic data set and a field data set obtained from a layered sandy soil environment. Film flow was included in the hydrological model by two additional fitting parameters to account for non-capillary water flow during dry conditions.

In the case of synthetic data, the coupled inversion resulted in excellent fits to the GPR data even when a wrong model formulation was used. Errors introduced by neglecting the film flow parameters can be compensated by different hydraulic parameters. Accounting for film flow during the inversion process led to an accurate estimation of the soil hydraulic properties, which showed the importance of an appropriate model conceptualization when using 75 time-lapse measurements in a coupled inversion.

For field data, the coupled inversion reduced the overall misfit compared to an uncalibrated model using hydraulic parameters obtained from laboratory data. Although the data fit improved significantly for water content in the deeper soil layers, accounting for film flow in the uppermost subsurface layer did not lead to a better fit of the GPR data. Here, further research is needed to improve the modeling by including the processes controlling water content in the dry range, in particular coupled heat and vapor transport.

The application of the novel FWI and the coupled hydrogeophysical inversion illustrates the potential of surface GPR to estimate quantitative permittivity and conductivity values for the same sensing volume, provide reliable information about soil water dynamics and soil hydraulic parameters, respectively. The proposed inversion approaches can be applied to a wide range of studies for an improved subsurface characterization.

Chapter 1

Introduction

1.1 Research Topic

The characterization of the subsurface with various geophysical electromagnetic methods is of growing importance. Since ground penetrating radar (GPR) techniques (crosshole, off-ground and surface GPR) are capable of producing high-resolution images of the shallow subsurface, they are applied increasingly for a wide range of applications such as geophysical engineering, environmental studies and infrastructure characterization.

Conventional surface GPR systems consist of two antennas; a transmitting antenna, which emits an electromagnetic wave into the subsurface, and a receiving antenna, which detects the back-travelling waves. The travel time of the measured wave is influenced by the electromagnetic wave speed that depends on the permittivity, whereas the amplitude of the measured wave is influenced by the attenuation due to the electrical conductivity, reflection and transmission coefficients, vectorial radiation patterns, and polarization properties.

Three measurement modes can be used: crosshole, off-ground and surface GPR, that have their own drawbacks, benefits and need for specific processing steps.

Crosshole GPR operates between two parallel boreholes at a distance in which the transmitting and receiving antenna are located. Thereby, the emitted energy propagates from the source antenna to the receiver antenna and commonly the first arrival times are used for a large number of source and receiver position to obtain velocity information from between the boreholes. Although crosshole GPR is widely used (e. g. Binley et al., 2001, Kuroda et al., 2009), the method is evidently restricted by the availability of borehole installations.

Due to their non-invasive nature, off-ground and surface GPR overcome this limitation and are applied more often. Off-ground GPR uses air launched antennas installed at a sufficient height above the surface and is often used for soil characterization (e.g. Redman et al., 2002; Lambot et al., 2004a; Weihermüller et al., 2007) and high speed measurements for asphalt characterization (e.g. Saarenketo and Scullion, 2000; Hugenschmidt, 2002). Since mainly vertical wave propagation occurs, the applied measurement setup often consists of a constant offset between the source and receiver antenna. To interpret and invert the measured waves, horizontal layers are often assumed. However, the relatively large reflection occurring at the interface between the air and ground results in a relative shallow

penetration depth. Moreover, the measurement setup is sensitive to the surface roughness (Lambot et al., 2006a).

In contrast to off-ground GPR, surface GPR antennas are optimized to emit the energy into the subsurface to a significant higher penetration depth. Due to the relatively wide radiation patterns, commonly measured waves include the air and ground wave travelling directly from transmitting to receiver antenna along the surface, and reflected and refracted waves emerging from the subsurface. In addition to the common-offset source receiver setup, commonly used setups are the common-midpoint (CMP) or the wide-angle reflection-refraction (WARR) method (Huisman et al., 2003), where the midpoint or source position remains fixed, respectively.

Whereas the common-offset method enables the mapping over larger areas, the CMP and WARR method enable an improved characterization of the subsurface since the different wave types, such as direct air and ground waves, and reflected and refracted waves, can be clearly distinguished when increasing the distance between the source and receiver antennas. Common processing steps are velocity- or semblance analysis where the velocity of the electromagnetic waves can be estimated using ray-based techniques such as ground wave picking (Galagedara et al., 2003; Steelman and Endres, 2010), reflected wave analysis (Tillard and Dubois, 1995; Greaves et al, 1996; Endres et al., 2000; Garambois et al., 2002; Jacob and Hermance, 2004; Bradford, 2008), refracted wave analysis (Bohidar and Hermance, 2002) or a combined analysis of ground, reflected and refracted waves (van Overmeeren et al., 1997; Huisman et al., 2003). Most of these techniques have been developed for the processing of seismic data and to determine the seismic wave velocity (Yilmaz, 1987). The advantage of these ray-based methods is that the medium properties can be easily computed from the measured data. However, since only the phase information of the GPR data is used, these methods only yield reliable values for the permittivity of the subsurface when far-field approximations are valid. Although GPR measurements contain information about the permittivity and conductivity of the subsurface through the travel time and amplitudes, estimating the conductivity using far-field approximations comes with large errors. Therefore, the simultaneous quantitative permittivity and conductivity characterization of the subsurface is not possible using ray-based techniques.

For an improved characterization of the subsurface, the vector phenomenon of GPR needs to be honored. The amplitudes and phases of the received signal depend on the antenna orientation and wave propagation paths, such that it is necessary to account for the antenna radiation patterns (Annan et al., 1975; Engheta et al., 1982), the vector characteristics of the GPR data (van der Kruk, 2001, Streich and van der Kruk, 2007a) as well as angle-dependent reflection coefficients. Several authors showed that these vectorial radiation characteristics and polarization effects play an important role to describe the amplitudes of the electromagnetic field (Jiao et al., 2000; Radzevicius and Daniels, 2000; van der Kruk, 2001).

Accounting for the exact radiation characteristics becomes more important as the subsurface becomes more complex. A promising step to improve the inversion of GPR data

is to include advanced modeling tools that are able to calculate the propagation of electromagnetic waves in complicated media configurations and have become more and more possible due to the increased computing power available. Here, the full-waveform inversion (FWI) is one of the most promising but also challenging data-fitting techniques (Virieux and Operto, 2009) that is able to use these advanced modeling programs to derive quantitative medium properties. Numerous methods of the full-waveform inversion have been developed and applied for seismic data including finite-difference and finite-element approaches of the acoustic-, elastic-, viscoelastic-, and anisotropic-wave equations in time-domain (Tarantola, 1984a; b; Gauthier et al., 1986; Mora, 1987; Crase et al., 1990) and frequency-domain (Pratt and Worthington, 1990; Pratt, 1990a; b; 1999, Shin and Cha, 2008; Brossier et al., 2009; Hu et al., 2009; Ben-Hadj-Ali et al., 2011).
Although there are various full-waveform inversion methods for seismic data, comparable inversion approaches of FWI are limited because they are not directly applicable on GPR data and must be adapted for accounting for the vectorial character of the source and receiver radiation characteristics and the electromagnetic wave propagation.
Recent developments in full-waveform inversion of crosshole (Ernst et al., 2007a; Meles et al., 2010; Klotzsche et al., 2010; Klotzsche et al., 2012) and off-ground GPR (Lambot et al., 2004b; Kalogeropoulos et al., 2011), where significant information of the measured data is used, indicate the benefits of FWI inversion approach to estimate quantitative permittivity and conductivity values. All full-waveform inversions need knowledge about the emitted field which can be described by an effective source wavelet. For off-ground GPR, the emitted electric field can be considered as independent from the subsurface (Slob et al., 2010). For crosshole GPR, the radiation characteristics for the antennas can be approximated by the radiation patterns in a homogeneous space. Here, the exact radiation patterns are well described by the far-field expressions (van der Kruk et al., 2003).
For surface GPR radiation patterns, far-field expressions still differ from the exact radiation patterns at a distance of seven wavelengths (Streich and van der Kruk, 2007a). Moreover, the coupling of the antennas and therefore the shape and amplitude of the wavelet strongly depend on the underlying medium (Smith, 1984). Consequently, the estimation of the effective source wavelet and therefore the application of the FWI is less straight forward.

Since the dielectric permittivity is highly correlated to the soil water content (Topp et al., 1980; Wharton et al., 1980; Tabbagh et al., 2000) and the electric conductivity depends on material properties such as water content, ion concentration and soil texture (Rhoades et al., 1976), especially surface GPR has become a fundamental technique for mapping the surface permittivity into soil water content using common offset and CMP/WARR data (e.g. Huisman et al., 2003). Recently, Gerhards et al. (2008) and Pan et al. (2012) proposed and optimized multichannel surface GPR to measure simultaneously the reflector depth and average soil-water content of the subsurface and to quantify the soil water dynamics at the field scale. Additionally, Buchner et al. (2012) introduced a novel inversion scheme for multichannel common-offset GPR measurements based on a Finite Difference Time

Domain (FDTD) simulation to estimate the soil water content and the geometry of layer interfaces. The proposed approach is intermediate between inverting of picked reflectors using ray based techniques and the more advanced full-waveform inversion (Busch et al., 2012).

Due to the strong correlation with the soil water content, geophysical tools also have the potential to estimate the soil hydraulic properties. Obtaining accurate estimates of soil hydraulic properties is essential for the prediction of water flow through the system and its interaction with the atmosphere and ground water, respectively, and are required to simulate these processes. Nevertheless, modeling of hydrological processes is not straightforward due to the highly dynamical nature of processes such as evaporation, precipitation and the spatial variability of the soil hydraulic properties (Ersahin and Brohi, 2006; Behaegel et al., 2007) which also limits the understanding of the system.
Promising techniques to characterize dynamic processes in the subsurface are time-lapse geophysical surveys in combination with coupled inversion schemes where a hydrological model of the subsurface is combined with a geophysical forward model.
Cross-borehole GPR has been used successfully in a number of studies for estimating soil hydraulic properties using coupled inversion schemes (Rucker and Ferré, 2004; Kowalsky et al., 2005; Looms et al., 2008). Lambot et al. (2004c, 2006b and 2009) developed a hydrological inversion scheme to estimate the soil hydraulic properties of the shallow subsurface using off-ground GPR data. Given their non-invasive nature and potential depth of investigation, surface GPR methods such as reflection profiling and CMP sounding are promising hydrogeophysical methods for obtaining hydrological information. However, there have been no previous studies examining the application of coupled inversion for hydrological parameter estimation to actual surface GPR field data acquired using these methods.

1.2 Thesis objectives and outline

The principal objective of this research is the development and application of advanced inversion methods for surface GPR to reliably estimate permittivity and conductivity, as well as the soil hydraulic properties of a layered subsurface from time-lapse measurements.

In this framework, the thesis is organized as follows:
First, I will describe in Chapter 2 a three-dimensional frequency-domain solution of Maxwell's equations for wave propagation in horizontally layered media representing the subsurface.
In Chapter 3, I introduce a novel full-waveform inversion for surface GPR CMP data for a horizontally layered subsurface. Optimizing the source wavelet's amplitude and phase simultaneously with the medium properties returns a data-driven effective source wavelet.

Changes in the subsurface properties and therefore the wavelet characteristics are explicitly taken into account during the inversion process. Since a two-dimensional approach would not accurately describe the geometrical spreading of true measurements, and commonly used 3D to 2D conversion approaches again introduce errors, I use a 3D full-waveform forward model for a horizontally layered model of the subsurface (van der Kruk et al., 2006). The novel approach is applied and verified for synthetic single-layer and waveguide data and for experimental data recorded across a single-layer low-velocity waveguide. For the experimental data, a signal-to-noise threshold is introduced above which the frequency components are used.

In Chapter 4 I extend and verify the surface GPR full-waveform inversion for the analysis of the direct ground wave. Therefore, combined Theta probe, electromagnetic resistivity tomography (ERT), electromagnetic induction (EMI) and ground penetrating radar (GPR) measurements were carried out over a silty loam with a significant variability in the soil texture. The isolated ground wave present in the GPR data was inverted using the FWI and the obtained permittivities and conductivities are consistent with the Theta probe, ERT and EMI results. Moreover, I correlate the obtained medium permittivities and conductivities with the soil texture and the wavelet center frequency and amplitude, respectively, and further formulate a linear relationship that describes the close relationship between the subsurface clay, silt and skeleton content and the permittivity and conductivity values obtained from the GPR FWI.

Besides the full-waveform inversion, the high information content present in GPR data can also be used for a coupled inversion of time lapse GPR measurements. Therefore, in order to invert for the hydraulic properties of a layered subsurface, I propose in Chapter 5 a coupled hydrogeophysical inversion of time-lapse surface GPR data by coupling measured interval velocities and travel times with a hydrological model of the subsurface. The hydrological model uses the classical Mualem-van Genuchten model (Mualem, 1976; van Genuchten, 1980) in combination with the film flow model by Peters and Durner (2008). A synthetic case study was carried out to analyze if the GPR data contain enough information for the estimation of the soil hydraulic properties of a multi-layered medium. The coupled inversion approach was applied to the measured data set of Steelman et al. (2012). Since the largest mismatch was observed in the dry range, I test how the different parameterizations of the subsurface model and the unsaturated hydraulic conductivity function affect the estimation of the hydraulic properties and the data fit, especially for relatively dry conditions.

Chapter 6 summarizes the results of the novel full-waveform and coupled hydrogeophysical inversions described in Chapter 3-5 and provides an outlook on future research.

In Appendix A I give an example for the wide applications of the FWI methodology by describing the full-waveform inversion approach by Kalogeropoulos et al. (2011) to evaluate the effect of chlorides and moisture on off-ground GPR signals.

Chapter 2

Theory

In this Chapter, the basic concepts are formulated that are necessary to describe the propagation of electromagnetic waves in a layered medium. First, Maxwell's equations are presented in time- and frequency-domain. Next, far-field expressions are shown for a horizontal electric dipole in a homogeneous space and in a homogeneous half-space. Finally, an exact forward modeling approach is introduced for a horizontally layered earth that describes all wave-propagation phenomena including the near-, intermediate-, far-field contributions to the antenna radiation pattern.

2.1 Maxwell's equations

The electromagnetic wave propagation is described by Maxwell's equations. Here, the electromagnetic field is described by the electric field intensity E, the electric displacement D, the magnetic induction B and the magnetic field intensity H. In time-domain, the Maxwell's equations are given by

$$\nabla \times H = \frac{\partial D}{\partial t} + J, \tag{2.1a}$$

$$\nabla \times E = -\frac{\partial B}{\partial t}, \tag{2.1b}$$

$$\nabla \cdot D = \rho, \tag{2.1c}$$

$$\nabla \cdot B = 0, \tag{2.1d}$$

where J is the conduction current density and ρ is the electric charge density. In order to derive the fundamental GPR equation (telegraph equation), describing the propagation of electromagnetic waves in a medium, we first substitute $D = \varepsilon E$, $B = \mu H$ and $J = \sigma E$ in equations (2.1a) and (2.1b). Here, $\varepsilon = \varepsilon_r \varepsilon_0$ is the dielectric permittivity with the relative permittivity ε_r [-] and the permittivity of free space $\varepsilon_0 = 8.88542 \cdot 10^{-12}$ [F/m]. The magnetic permeability $\mu = \mu_r \mu_0$ is described by the relative magnetic permeability μ_r and the free-space value $\mu_0 = 4\pi \cdot 10^{-7}$ [H/m]. The electric conductivity is given by σ [S/m].

After eliminating the magnetic field H and carrying out a temporal Fourier transformation, the general solution for the electric field in the space-frequency domain at a certain position x can be formulated as (van der Kruk et al., 2003)

$$\hat{E}_k(x,\omega) = \int \hat{G}_{kr}^{EJ}(x,\omega)\hat{J}_r^e(x,\omega)dV, \tag{2.2}$$

where $\hat{G}_{kr}^{EJ}(x,\omega)$ is the Green's function describing the propagation of an electric field from a known electric source $\hat{J}_r^e$, $\omega = 2\pi f$ is the angular frequency and f is the frequency, respectively.

2.1.1 Electromagnetic properties in earth materials

Table 2.1 shows the relative permittivity ε_r [-], the electric conductivity σ [mS/m], the electromagnetic wave velocity v [m/ns] and the attenuation α [dB/m] for selected materials at a frequency of 100 MHz (Davis and Annan, 1989). The relative permittivity of water is 80, whereas the permittivity for air is 1 and for most other materials in between 10 - 40. The significant contrast in the permittivities clearly indicates the effect of water on the GPR wave velocity and explains the success of soil water content measurements using electromagnetic methods (Huisman et al., 2003). Moreover, the conductivities of the materials shown in Table 2.1 cause a different attenuation of the GPR signal and clearly shows the ability of GPR techniques to obtain two independent medium property estimates for the same sensing volume (see also Chapter 1 and Chapter 3 and 4).

2.1.2 Electromagnetic field in homogeneous space

For a horizontal electric dipole in a homogeneous space, the Green's function $\hat{G}_{kr}^{EJ}(x,\omega)$ of the electric field in equation (2.2) can be written as (de Hoop, 1995; van der Kruk et al., 2003)

$$\hat{G}_{kr}^{EJ}(x,\omega) = \eta^{-1}\left[\partial_k \partial_r - \gamma^2 \delta_{kr}\right]\hat{G}(x,\omega), \tag{2.3}$$

where k is the wavenumber, r is the spatial variable in polar coordinates,

$$\hat{G}(R,\omega) = \frac{\exp(-\gamma|x|)}{4\pi R}, \tag{2.4}$$

and γ is the complex propagation factor

$$\gamma = \sqrt{j\omega\mu(\sigma + j\omega\varepsilon)} \tag{2.5}$$

with the imaginary unit $j = \sqrt{-1}$. Due to the spatial derivatives, different radiation characteristics arise which depend on the orientation of the electric source and the direction of the observation. Analyzing the amplitudes to investigate the differences in the closed-form representations of the radiation characteristics, van der Kruk et al. (2003) showed that, compared to the far-field contributions, the near- and intermediate-field have low amplitudes at a distance of 3.3λ and can be neglected in a homogeneous space.

Table 2.1 Relative permittivity ε_r, conductivity σ, velocity v and attenuation α observed for selected materials at a frequency of 100 MHz (Davis and Annan, 1989).

	ε_1 [-]	σ [mS/m]	v [m/ns]	α [dB/m]
Air	1	0	0.30	0
Distilled water	80	0.01	0.033	$2x10^{-3}$
Fresh water	80	0.5	0.033	0.1
Sea water	80	$3x10^4$	0.01	10^3
Dry sand	3-5	0.01	0.15	0.01
Saturated sand	20-30	0.1-1.0	0.06	0.03-0.3
Limestone	4-8	0.5-2	0.12	0.4-1
Shales	5-15	1-100	0.09	1-100
Silts	5-30	1-100	0.07	1-100
Clays	5-40	2-1000	0.06	1-300
Granite	4-6	0.01-1	0.13	0.01-1
Dry salt	5-6	0.01-1	0.13	0.01-1
Ice	3-4	0.01	0.16	0.01

2.1.3 Electromagnetic field in a homogeneous halfspace

For a lossless halfspace the far-field, asymptotic solutions of the Green's function in equation (2.2) can be formulated as (Engheta et al., 1982; Smith et al. 1984)

$$\hat{G}_{kr}^{EJ}(x,\omega) = j\omega\hat{A}_{kr}\hat{G}(x,\omega), \tag{2.6}$$

where $\hat{A}_{kr}$ is an angle-dependent amplitude factor. Analyzing the electromagnetic field where the horizontal electric dipole is located on the interface between two homogeneous half spaces with ε_0 and ε_1 (see Figure 2.1), the intermediate-field has larger amplitudes than in a homogeneous space (van der Kruk et al., 2003) and therefore cannot be neglected. Here, since closed-form analytic solutions of Maxwell's equations are not available in the space-frequency domain (Annan, 1973), exact-field solutions are necessary to describe the propagation of the electric field sufficiently (e.g. van der Kruk, 2001).

2.2 Exact-field electromagnetic forward model

Exact-field solutions for a horizontally layered earth involve the numerical evaluations of integral equations. The forward modeling of CMP/WARR data is based on the work of van der Kruk et al. (2006), who considered the transverse electric (TE) and transverse magnetic (TM) modes of GPR propagation (Figure 2.1), where the electric and magnetic fields are polarized perpendicular to the plane of incidence.

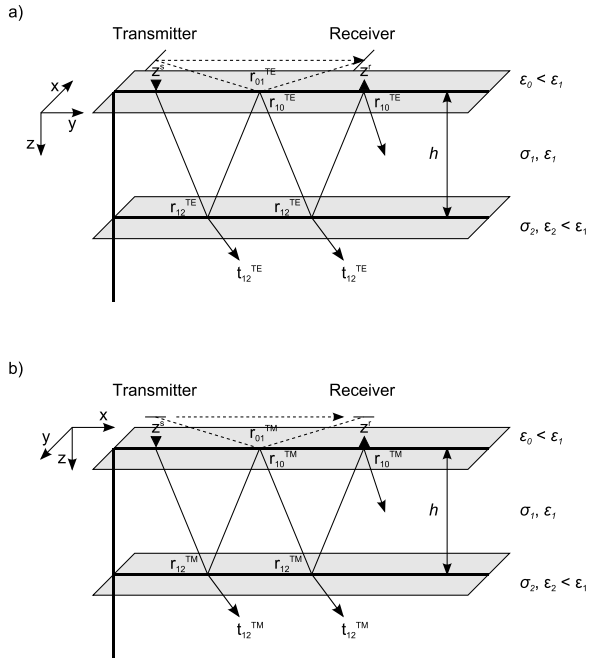

Figure 2.1 Diagram of the (a) TE and (b) TM source-receiver configurations. For both configurations the *x*-axis is oriented parallel to the long axes of the antennas. r_{ab}^{TE}, t_{ab}^{TE}, r_{ab}^{TM}, and t_{ab}^{TM} are the reflection and transmission coefficients for the TE- and TM-GPR at the interface between layer *a* and *b*, respectively.

The expression for the exact electric field $\widetilde{E}_x$ due to a transmitting dipole with a source wavelet $\widetilde{W}_x$ is described in the horizontal wavenumber frequency-domain as

$$\widetilde{E}_x = \left[\widetilde{G}_{xx}^{TE} + \widetilde{G}_{yy}^{TM}\right] \cdot \widetilde{W}_x, \tag{2.7}$$

where $\widetilde{G}_{xx}^{TE}$ and $\widetilde{G}_{yy}^{TM}$ describe the Green's functions and can be written as

$$\widetilde{G}_{xx}^{TE} = \frac{k_y^2 \varsigma_0}{2\Gamma_0 \kappa^2}\left[\exp\left[-\Gamma_0\left(z^r - z^s\right)\right] + \left(r_{01}^{TE} + \frac{t_{10}^{TE} t_{12}^{TE} t_{01}^{TE} \beta}{1 - r_{12}^{TE} r_{10}^{TE} \beta}\right)\exp\left[-\Gamma_0\left(z^r + z^s\right)\right]\right], \tag{2.8a}$$

$$r_{ab}^{TE} = \frac{\varsigma_b \Gamma_a - \varsigma_a \Gamma_b}{\varsigma_b \Gamma_a + \varsigma_a \Gamma_b}, \text{ with } r_{ba}^{TE} = -r_{ab}^{TE}, \tag{2.8b}$$

$$t_{ab}^{TE} = \frac{2\varsigma_b \Gamma_a}{\varsigma_b \Gamma_a + \varsigma_a \Gamma_b}, \text{ with } t_{ba}^{TE} = 2 - t_{ab}^{TE}, \tag{2.8c}$$

and

$$\widetilde{G}_{yy}^{TM} = \frac{k_x^2 \Gamma_0}{2\eta_0 \kappa^2}\left[\exp\left[-\Gamma_0\left(z^r - z^s\right)\right] + \left(r_{01}^{TM} + \frac{t_{10}^{TM} t_{12}^{TM} t_{01}^{TM} \beta}{1 - r_{12}^{TM} r_{10}^{TM} \beta}\right)\exp\left[-\Gamma_0\left(z^r + z^s\right)\right]\right], \tag{2.9a}$$

$$r_{ab}^{TM} = \frac{\varsigma_a \Gamma_b - \varsigma_b \Gamma_a}{\varsigma_a \Gamma_b + \varsigma_b \Gamma_a}, \text{ with } r_{ba}^{TM} = -r_{ab}^{TM}, \tag{2.9b}$$

$$t_{ab}^{TM} = \frac{2\varsigma_a \Gamma_b}{\varsigma_a \Gamma_b + \varsigma_b \Gamma_a}, \text{ with } t_{ba}^{TM} = 2 - t_{ab}^{TM}. \tag{2.9c}$$

Here,

$$\beta = \exp\left(-2\Gamma_1 h\right), \tag{2.10}$$

$$\kappa = \sqrt{k_x^2 + k_y^2}, \tag{2.11}$$

$$\varsigma_a = i\omega\mu_a, \tag{2.12}$$

$$\Gamma_a = \sqrt{\gamma_a^2 \mu_a + \kappa^2}, \tag{2.13}$$

and Γ_0, Γ_a, Γ_b are propagation constants, r_{ab}^{TE}, r_{ab}^{TM}, t_{ab}^{TE} and t_{ab}^{TM} are the corresponding reflection and transmission coefficients, z^s and z^r define the height of the transmitting and receiving antenna, h is the thickness of layer 1 and k_x and k_y are the horizontal wave numbers, respectively. The subscripts a, b with $a < b$ represent the different layers and take values from {0, 1, 2}, where medium 0 describes the air at the surface, and medium 1 and 2 describe the subsurface layer and the underlying half space (see also Figure 2.1). Electromagnetic waves propagating in a certain layer are indicated by the first subscript and are transmitted into or reflected at the layer, indicated by the second subscript. To obtain the expression given by equations (2.8a) and (2.9a) in the space-domain, the inverse Fourier transformation of the electrical field is obtained by employing the Fourier inversion integral

$$\hat{E}_x\left(k_x, k_y, z, \omega\right) = \left(\frac{1}{2\pi}\right)^2 \int_{(k_x, k_y) \in R^2} \exp\left(-jkx\right)\widetilde{E}\left(k_x, k_y, z, \omega\right) dA. \tag{2.14}$$

Introducing polar coordinates (r,ϕ), $\hat{E}_x$ can be written as (van der Kruk, 2001)

$$\hat{E}_x = \frac{1}{2\pi}\int_{\kappa=0}^{\infty} \widetilde{E}_x J_0\left(\kappa\rho\right)\kappa d\kappa, \tag{2.15}$$

with

$$\rho = \sqrt{r\cos\left(\phi\right)^2 + r\sin\left(\phi\right)^2}, \tag{2.16}$$

where J_0 is the zeroth order Bessel function.

According to equation (2.7) the frequency domain electric field is defined by multiplying the subsurface Green's function with the source wavelet. Assuming a horizontally layered subsurface as shown in Figure 2.1, the propagation of the electromagnetic waves can be reconstructed by forward modeling with the knowledge of the medium parameters ε_0, ε_1, ε_2, σ_1, σ_2, h and the source wavelet.

Chapter 3

Quantitative conductivity and permittivity estimation using full-waveform inversion of surface GPR data*

In this Chapter we introduced the frequency-domain full-waveform inversion (FWI) approach for surface GPR data and focus on the analysis of reflected waves. Compared to common approaches of the FWI methodology in seismics, our approach requires no computations of the derivatives of the objective function, i.e. neither Jacobians matrices nor gradients are necessary. Instead of a gradient-based minimization, a complex combination of grid and simplex search is used to fit the measured data with synthetic data calculated for a horizontally layered model. Since the coupling of source and receiver antennas strongly depend on the medium properties, this approach includes an explicit wavelet optimization that is carried out simultaneously with the optimization of the medium properties and results in a robust reconstruction of the medium properties and the wavelet's phase and amplitude, respectively. In contrast to commonly used approaches where the center frequency of the antenna source wavelet is assumed to be specified by the manufacturer (Wu and Liu, 1999; Bano, 2004; Buchner et al., 2012), the full-waveform inversion returns a data-driven effective source wavelet. In this way, changes in the subsurface properties and therefore the wavelet characteristics are explicitly taken into account during the inversion process. Because a two-dimensional approach would not accurately describe the geometrical spreading of true measurements, and commonly used 3D to 2D conversion approaches again introduce errors, we use a 3D full-waveform forward model for a horizontally layered model of the subsurface (van der Kruk et al., 2006, see Chapter 2.2).

First, we will describe the 3D full-waveform forward model for a horizontally layered subsurface which is used to simulate the surface GPR measurements. Moreover, ray-based far-field approximations are described that are used to obtain a starting model for the conductivities. Next, since the inversion of synthetic data clearly shows that errors in the starting model conductivities result in wrong estimates of the wavelet's amplitude and therefore prevent the precise estimation of the conductivity values, we discuss the accurate estimation of the effective source wavelet from the surface GPR.

Alternating the wavelet estimation with the medium property update as commonly done in seismics showed that this approach is not robust and can get stuck in a local minimum. This is probably due to the fact that the changes in the medium properties are driving the changes in the wavelet and no explicit optimization of the wavelet is carried out. To

*Adapted from Busch, S., J. van der Kruk, J. Bikowski, and H. Vereecken, 2012, Quantitative conductivity and permittivity estimation using full-waveform inversion of on-ground GPR data, Geophysics, 77, H79–H91, doi: 10.1190/GEO2012-0045.1.

overcome these problems, we optimize the source wavelet's amplitude and phase simultaneously with the medium properties. The novel approach is successfully applied to synthetic single-layer and waveguide data and to experimental data recorded across a single-layer low-velocity waveguide.

3.1 Full-waveform inversion methodology

Full-waveform inversion is a challenging data-fitting technique to extract quantitative information (Virieux and Operto, 2009) by finding the model parameters that fit best the observed data. The method includes the calculation of the complete electrical field in the subsurface (forward model), which requires a starting model of the material properties and an estimation of the antenna source wavelet.

3.1.1 Starting model estimation using far-field forward model

In general, far-field ray-based approximations can be used to estimate the velocities for simple model configurations. Although standard ray-based techniques are widely used to estimate the permittivity and thickness of the subsurface (e.g. Huisman et al., 2003), the estimation of quantitative conductivity values is less straightforward due to the many factors that influence the amplitude (Annan, 1973; Noon et al., 1998). For crosshole GPR, where the subsurface can be approximated as a homogeneous space, the far-field expressions resemble well the velocities and amplitudes of the total-field expressions (van der Kruk et al., 2003). In case of surface GPR where the subsurface can be described as a homogeneous half-space, estimates of the conductivity can be obtained from the direct ground wave (DGW) that travels between the transmitting and receiving antenna. The DGW is described by the far-field approximation

$$E(x,t) = \frac{-\sqrt{\varepsilon_1} Z_0 \exp\left(-\frac{\sigma_1}{2} Z_1 x\right)}{2\pi(1-\varepsilon_1)x^2} W\left(t - \frac{x}{c_1}\right), \tag{3.1}$$

where ε_1, σ_1, c_1, are the relative permittivity, conductivity and velocity of the subsurface, respectively, x, t are the offset and the travel time, Z_0 is the electrical impedance of air and W equals the emitted wavelet (van der Kruk and Slob, 2002). The exponential attenuation factor describes the amplitude decay due to the conductivity and depends on the electrical impedance Z_1 which is given by

$$Z_1 = \sqrt{\frac{\mu_0}{\varepsilon_1 \varepsilon_0}}, \tag{3.2}$$

where ε_0 is the permittivity for vacuum and μ_0 is the free space magnetic permeability. The ground waves amplitude decays with $1/x^2$. For waveguide data, the amplitude decay is

reduced since the energy is trapped within the waveguide. Here, an approximate 2D geometrical spreading of $1/\sqrt{x}$ can be assumed. In this way, equation (3.1) can be used to estimate the conductivity using the amplitude decay.

3.1.2 Exact forward modeling

The full-waveform inversion that is minimizing the misfit between observed and modeled data, requires precise modeled data and hence an efficient and accurate forward model which calculates the electrical field. The time domain electrical field $E(t,x)$ for a point dipole source is a convolution of the source wavelet $W(t)$ with the Greens function $G(t,x)$. In frequency domain, this operation is equivalent to a multiplication (see also Chapter 2.2)

$$\hat{E}(f,\mathbf{x},\mathbf{m}) = \hat{G}(f,\mathbf{x},\mathbf{m})\cdot\hat{W}(f), \tag{3.3}$$

where ^ indicates the corresponding functions in frequency-domain, f is frequency, $\mathbf{x}$ is a three-dimensional space variable and $\mathbf{m}$ describes the parameters of the medium. Because we only consider several receiver positions in one direction, the space variable $\mathbf{x}$ is reduced to offset x_m and f is limited to a discrete set of frequencies f_n. Assuming point dipole antennas, a homogeneous horizontally layered medium with the medium properties $\mathbf{m} = [\varepsilon_1, \varepsilon_2, \sigma_1, \sigma_2, h]$ and a constant magnetic permeability, the Greens function can be calculated by evaluation of the exact integral equations that include the near-, intermediate and far-field as well as angle- and frequency-dependent reflection coefficients (van der Kruk, 2001; van der Kruk et al., 2006).

3.1.3 Source wavelet estimation

To enable a full-waveform inversion, a wavelet must be determined that describes the transmitting and receiving antenna wavelets by a point dipole transmitter and receiver. Since a GPR antenna has a finite length and the forward model of the Green's function considers point dipole antennas, an effective source wavelet is estimated from the data that effectively includes the influence of the finite length. With the medium properties $\mathbf{m}$, a Greens function, $\hat{G}(f_n, x_m, \mathbf{m})$, can be calculated and an effective wavelet can be determined by deconvolution of the observed electrical field $\hat{E}_{obs}(f_n, x_m)$ with the Greens function. Since the measured data consists of several offsets, the best-fit effective source wavelet $\hat{W}_{est}(f_n)$ for a specific frequency f_n can be obtained by applying a least squares technique to solve the over-determined system of equations (Ernst et al., 2007a; Streich and van der Kruk, 2007b; Klotzsche et al., 2010)

$$\hat{G}(f_n, x_m, \mathbf{m})\cdot\hat{W}_{est}(f_n) = \hat{E}_{obs}(f_n, x_m). \tag{3.4}$$

Equation (3.4) indicates the close relationship between the Greens function $\hat{G}(f_n, x_m, \mathbf{m})$, the medium properties $\mathbf{m}$ and the effective source wavelet $\hat{W}_{est}(f_n)$. In case of approximate or

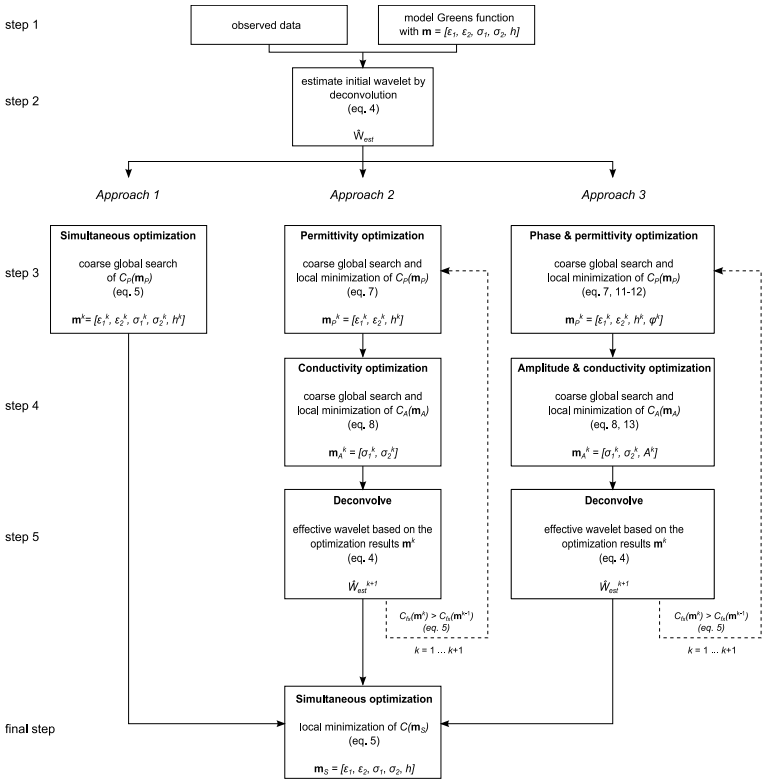

Figure 3.1 Outline of the full-waveform *Approach 1* (left column), *Approach 2* (middle column) and *Approach 3* (right column).

erroneous medium properties this will directly affect the wavelet shape and amplitude. Therefore, it is necessary to integrate the wavelet estimation within the full-waveform inversion. Since such an integration is not straightforward for gradient based inversion algorithms, we use here a combined global and local optimization approach.

3.1.4 Full-waveform inversion

For the minimization of the misfit between the observed and modeled data, several optimization approaches can be used. Starting from straightforward model optimization, we

successively describe the complications of this method and describe the benefits of more complicated approaches.

Approach 1: simultaneous model optimization

Using far-field ray-based approximations, an initial model can be estimated and an initial effective wavelet can be calculated (Figure 3.1, left column, steps 1-3, final step). A straightforward approach to update the initial model parameters $\mathbf{m}^k = [\varepsilon_1, \varepsilon_2, \sigma_1, \sigma_2, h]$ is a combined global search and a local minimization. The global search (Figure 3.1, left column, step 3) is carried out by calculating the objective function C_{fx} at each grid point of an equidistant grid for $\mathbf{m}^k$ in the interval $[\mathbf{m}^k - 0.01\alpha_0\mathbf{m}^k,\ \mathbf{m}^k + 0.01\alpha_0\mathbf{m}^k]$, where α_0 is a defined percentage deviation to the initial starting model, by

$$C_{fx}\left(\mathbf{m}^k\right) = \frac{1}{M \cdot N} \sum_{m=1}^{M} \sum_{n=1}^{N} C\left(f_n, x_m, \mathbf{m}^k\right), \text{ with} \tag{3.5}$$

$$C\left(f_n, x_m, \mathbf{m}^k\right) = \left| \frac{\hat{E}_{mod}\left(f_n, x_m, \mathbf{m}^k\right) - \hat{E}_{obs}\left(f_n, x_m\right)}{\hat{E}^{\max}(x_m)} \right|, \tag{3.6}$$

where $\hat{E}_{mod}(f_n,x_m,\mathbf{m}^k)$ and $\hat{E}_{obs}(f_n,x_m)$ are the modeled and observed data, M and N are the number of offsets and frequencies, respectively. Note, to avoid the irregular weighting of different offsets, equation (3.6) is trace-normalized by the maximum spectral amplitude, $\hat{E}^{max}(x_m) = max\{|\hat{E}_{obs}(f_n,x_m)|,\ n=1,\ldots,N\}$, of each offset. The parameter combination with the smallest value for the objective functions serves as a starting model for the local minimization (Figure 3.1, final step). The minimization of the objective function C_{fx} is carried out using a simplex search algorithm (Lagarias et al., 1998) which belongs to the direct search methods and solves nonlinear unconstrained optimization problems. The method does not require any gradients and finds the minimum of multivariable functions, starting at an initial estimate.

The source wavelet is directly affected by the permittivities and electrical conductivities of the initial model, i.e. especially a low value for σ_1 increases the wavelet amplitude whereas a high value for σ_1 decreases the wavelet amplitude. Since the effective source wavelet is fixed during the entire optimization process, and inaccuracies in the initial starting model are propagated due to the deconvolution (3.4) into the source wavelet, the simultaneous optimization returns erroneous inversion results. Therefore, the source wavelet needs to be updated within the inversion algorithm.

Approach 2: combined sequential and simultaneous model optimization

To optimize the subsurface properties and the wavelet, an iterative sequential and simultaneous optimization approach is implemented. The approach consists of an iterative, sequential optimization of the permittivities and thickness followed by a sequential

optimization of the conductivities (Figure 3.1, middle column, step 3 & 4). Next, the update of the effective source wavelet is obtained by the deconvolution approach (3.4) using the optimized medium properties (Figure 3.1, middle column, step 5), followed by a simultaneous optimization of the model parameters while keeping the wavelet fixed (Figure 3.1, final step).

Permittivity and conductivity optimization (Figure 3.1, middle column, step 3 & 4) – First, a coarse global search is carried out by calculating the objective function of the phase C_P

$$C_P\left(\mathbf{m}_P^k\right) = \frac{1}{M \cdot N} \sum_{m=1}^{M} \sum_{n=1}^{N} \left(\left| \frac{\hat{E}_{mod}\left(f_n, x_m, \mathbf{m}_P^k\right)}{\left|\hat{E}_{mod}\left(f_n, x_m, \mathbf{m}_P^k\right)\right|} - \frac{\hat{E}_{obs}\left(f_n, x_m\right)}{\left|\hat{E}_{obs}\left(f_n, x_m\right)\right|} \right| \right), \tag{3.7}$$

at each grid point of an equidistant grid for $\mathbf{m}_P^k = [\varepsilon_1, \varepsilon_2, h]$ in the interval $[\mathbf{m}^{k-1} - (\alpha_0 - 0.1k)\ \mathbf{m}^{k-1}, \mathbf{m}^{k-1} + (\alpha_0 - 0.1k)\ \mathbf{m}^{k-1}]$. The parameter combination of $\mathbf{m}_P^k$ with the smallest value for C_P serves as a starting model for the local minimization. Note that the conductivities σ_1, σ_2 are fixed. Next, the objective functions for the amplitude C_A

$$C_A\left(\mathbf{m}_A^k\right) = \frac{1}{M \cdot N} \sum_{m=1}^{M} \sum_{n=1}^{N} \left(\left| \frac{\left|\hat{E}_{mod}\left(f_n, x_m, \mathbf{m}_A^k\right)\right| - \left|\hat{E}_{obs}\left(f_n, x_m\right)\right|}{\hat{E}^{\max}(x_m)} \right| \right), \tag{3.8}$$

are calculated at each grid point of an equidistant grid for $\mathbf{m}_A^k = [\sigma_1, \sigma_2]$. Here, the spectral components in equation (3.8) are normalized by the maximum spectral amplitude at each offset and the medium properties ε_1, ε_2, and h are fixed. Again, the parameter combination with the smallest value for the objective functions serves as a starting model for a local minimization. To enable separate frequency and offset analyses of the objective function, we define the objective functions $C_f(f_n, \mathbf{m}^k)$, the average over all offsets, and $C_x(x_m, \mathbf{m}^k)$, the average over all frequencies, by

$$C_f\left(f_n, \mathbf{m}^k\right) = \frac{1}{M} \sum_{m=1}^{M} C\left(f_n, x_m, \mathbf{m}^k\right) \text{ and} \tag{3.9}$$

$$C_x\left(x_m, \mathbf{m}^k\right) = \frac{1}{N} \sum_{n=1}^{N} C\left(f_n, x_m, \mathbf{m}^k\right). \tag{3.10}$$

Deconvolution of the effective source wavelet based on the optimization results (Figure 3.1, middle column, step 5) - In the preceding steps, the model parameters were optimized sequentially. However, the close relationship between the entire starting model $\mathbf{m}^k = [\varepsilon_1^k, \varepsilon_2^h, \sigma_1^k, \sigma_1^k, h^k]$ and the wavelet makes a new estimation of the effective source wavelet necessary. Therefore, the Greens function is calculated for the parameters m^k and the new estimated wavelet $\hat{W}_{est}^{k+1}(f_n)$ is obtained by deconvolution (3.4).

The optimized model properties and the new estimated wavelet serve as starting values for the next iteration. This process is repeated until the objective function (3.5) fulfils the termination criteria $C_{fx}(\mathbf{m}^k) > C_{fx}(\mathbf{m}^{k-1})$ or the maximum iteration number of 10 is reached.

Simultaneous model optimization (Figure 3.1, final step) - Although the iterative optimization process considers the permittivity and conductivity values, the coupling between these parameters is not explicitly taken into account. Therefore, the final step of the full-waveform inversion consists of a simultaneous model optimization for the parameters $\mathbf{m}_s = [\varepsilon_1, \varepsilon_2, \sigma_1, \sigma_2, h]$ while keeping the wavelet fixed. The local minimization of the objective function $C_{fx}(\mathbf{m}^k)$ given in equation (3.5), consisting of a summation of all frequency and offset components, returns the final inversion result. Within this combined sequential and simultaneous model optimization approach, changes in the permittivities and conductivities are driving the changes in the wavelet phase and amplitude whereas the wavelet optimization is not explicitly included in the optimization process. This can result in slow convergence and/or a trapping in a local minimum.

Approach 3: combined sequential and simultaneous model and wavelet optimization

To explicitly include the phase and amplitude of the wavelet within the overall optimization we introduce additional wavelet optimization parameters and extend the phase and amplitude optimization of *Approach 2* given in equation (3.7) and (3.8).

Phase and permittivity optimization (Figure 3.1, right column, step 3) – Since, the phase of the electric field is mostly influenced by ε_1, ε_2, h and the phase of the wavelet, we introduce an additional parameter υ to explicitly optimize the phase of the effective source wavelet. Therefore, we substitute $\hat{E}_{mod}(f_n, x_m, \mathbf{m}_P^k)$ in the objective function C_P (3.7) with

$$\hat{E}_{mod}\left(f_n, x_m, \mathbf{m}_P^k\right) = \hat{G}\left(f_n, x_m, [\varepsilon_1, \varepsilon_2, h]\right) \cdot \left|\hat{W}_{est}^k(f_n)\right| \cdot \exp\left(i\varphi^k\right), \tag{3.11}$$

where υ^k is the optimized phase of the wavelet $\hat{W}_{est}^k(f_n)$ and k is the iteration number. In this way, the four parameter $\mathbf{m}_P^k = [\varepsilon_1, \varepsilon_2, h, \upsilon]$ are optimized, whereas the conductivity values σ_1, σ_2 are fixed. Finally, the optimized value for υ^k is used to correct the phase of the wavelet

$$\hat{W}_P^k(f_n) = \left|\hat{W}_{est}^k(f_n)\right| \cdot \exp\left(i\varphi^k\right). \tag{3.12}$$

Amplitude and conductivity optimization (Figure 3.1, right column, step 4) - In the next step, we introduce the wavelet amplitude factor A and rewrite the forward model $\hat{E}_{mod}(f_n, x_m, \mathbf{m}_A^k)$ in the objective function C_A (3.8) as

$$\hat{E}_{mod}\left(f_n, x_m, \mathbf{m}_A^k\right) = \hat{G}\left(f_n, x_m, [\sigma_1, \sigma_2]\right) \cdot A^k \cdot \hat{W}_P^k(f_n), \tag{3.13}$$

where the factor A^k enables the optimization of the amplitude of the wavelet $\hat{W}_A^k(f_n)$. Now, the parameters $\mathbf{m}_A^k = [\sigma_1, \sigma_2, A]$ are optimized whereas ε_1^k, ε_2^k, h^k remain constant.

3.2 Application to synthetic data

Two single-layer configurations with different thickness (Figure 3.2) were modeled to investigate the reliability of the far-field conductivity estimation and the full-waveform inversion. The electrical fields at the receiver positions depend on the vectorial radiation patterns (dashed circles) and the angle-dependent reflection coefficients at the layer boundaries (dotted circles). Figure 3.3 shows the corresponding calculated electric fields at the receiver positions, where in (a) the individual reflections can be distinguished and in (b) interfering multiples occur due to the presence of a waveguide. The modeled source wavelet is defined as a Ricker wavelet with a center frequency f_c = 70 MHz and the red and blue colors show the positive and negative amplitudes. Figure 3.3a shows a horizontally, single-layered subsurface with a relative permittivity ε_1 = 19.20, a electric conductivity σ_1 = 6.00 mS/m and a height h = 1.60 m overlying a halfspace with ε_2 = 8.60, and σ_2 = 12.00 mS/m. The second dataset shown in Figure 3.3b shows a complex low-velocity waveguide with the subsurface properties ε_1 = 26.80, ε_2 = 13.40, σ_1 = 12.00 mS/m, σ_2 = 6.00 mS/m and h = 0.16 m. Here, the thickness h is on the order of a wavelength and since $\varepsilon_0 < \varepsilon_2 < \varepsilon_1$, the electromagnetic waves are multiply reflected between the layer boundaries resulting in interfering events such that the individual ground wave, reflections and multiples cannot be distinguished anymore.

In order to estimate a conductivity value from the ground wave in Figure 3.3a, it is clear that the maximum amplitudes can only be picked between 0.9 - 3.3 m due to the interfering air wave and reflection (see black line in Figure 3.3a). Fitting the amplitude decay with the exponential decay function using equation (3.1) returns a conductivity σ_1 = 7.09 mS/m, which contains an error of 18 % compared to the true value of σ_1 = 6.00 mS/m (see also Table 3.1).

For the waveguide data shown in Figure 3.3b, the estimation of the conductivity is more complicated due to the reduced geometrical spreading since the energy is trapped within the

Table 3.1 Estimations of the conductivity σ_1 for synthetic single-layer and waveguide-layer data using the far-field expression of the antenna radiation pattern.

	$\sigma_{1,modeled}$ [mS/m]	$\sigma_{1,far\text{-}field}$ [mS/m]	*error* [%]
single-layer data	6.00	7.09	18.16
waveguide-layer data	12.00	13.14	9.50

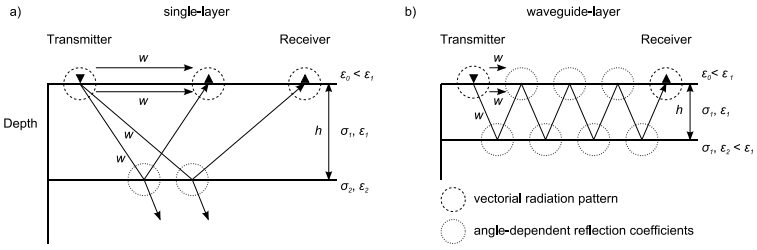

Figure 3.2 Horizontally single-layered model (a) and waveguide model (b) of the subsurface where w indicate the propagation of the electromagnetic waves, ε_0 is the relative permittivity of air; σ_1, ε_1, h are the conductivity, relative permittivity and thickness of layer whereas σ_2 and ε_2 are the electromagnetic properties of the underlying half-space.

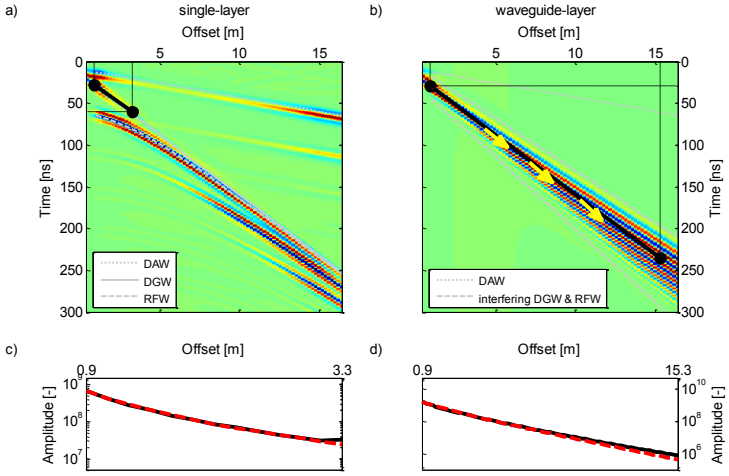

Figure 3.3 Synthetic single-layer data a) showing the direct air- and ground wave (DAW, DGW) and multiple reflections (RFW) with angle dependent reflection coefficients (see also Figure 3.2a and b) waveguide data, where the ground wave, reflected wave and multiple reflections are interfering and cannot be separately identified (see also Figure 3.2b). Solid black lines indicate the offset ranges used for the far-field conductivity estimation whereas yellow arrows (b) show the phase shift in the picked maximum amplitudes. Red and blue colors indicate low and high amplitudes which are trace normalized; c) and d) show the picked maximum amplitudes (black) and the fitted decay function (dashed red).

Table 3.2 Medium properties and objective function C_{fx} for the inversion of synthetic single-layer data.

Models	ε_1 [-]	ε_2 [-]	σ_1 [mS/m]	σ_2 [mS/m]	h [m]	C_{fx} [-]
true model	19.20	8.60	6.00	12.00	1.60	
starting model	23.00	11.00	1.00	20.00	1.80	1.01
Approach 1						
simultaneous inversion result	17.25	43.78	4.37	3.96e-11	1.47	2.55e-1
Approach 2						
sequential 1st iteration result	20.67	16.23	2.75	38.96	1.99	4.24e-1
sequential 2nd iteration result	20.68	18.23	4.62	107.96	2.02	2.94e-1
sequential 4th iteration result	20.91	20.86	5.00	190,89	2.06	2.90e-1
simultaneous inversion result	20.95	8.32	6.77	18.56	1.97	2.70e-1
Approach 3						
sequential 1st iteration result	20.67	16.24	4.38	36.61	1.99	3.08e-1
sequential 2nd iteration result	21.46	10.38	7.28	6.31	1.92	2.90e-1
sequential 4th iteration result	19.23	8.44	6.00	12.63	1.60	1.24e-2
sequential 10th iteration result	19.20	8.59	6.00	12.05	1.60	6.81e-4
simultaneous inversion result	19.20	8.60	6.00	12.01	1.60	4.66e-4

Table 3.3 Medium properties and objective function C_{fx} for the inversion of synthetic waveguide data.

Models	ε_1 [-]	ε_2 [-]	σ_1 [mS/m]	σ_2 [mS/m]	h [m]	C_{fx} [-]
true model	26.80	13.40	12.00	6.00	0.16	
starting model	23.00	11.00	20.00	1.00	0.25	0.40
Approach 1						
simultaneous inversion result	24.05	13.60	18.43	5.89	0.20	1.94e-1
Approach 2						
sequential 1st iteration result	26.57	13.39	15.64	5.67	0.16	8.36e-2
sequential 2nd iteration result	26.97	13.38	12.78	6.15	0.16	3.28e-2
sequential 6th iteration result	26.80	13.39	12.00	5.99	0.16	7.15e-5
simultaneous inversion result	26.80	13.40	12.00	6.00	0.16	1.29e-5
Approach 3						
sequential 1st iteration result	26.67	13.62	14.30	4.86	0.16	7.98e-2
sequential 2nd iteration result	26.66	13.36	11.97	5.97	0.16	6.88e-3
sequential 6th iteration result	26.79	13.39	11.99	6.00	0.16	3.80e-5
simultaneous inversion result	26.80	13.40	12.00	6.00	0.16	1.99e-5

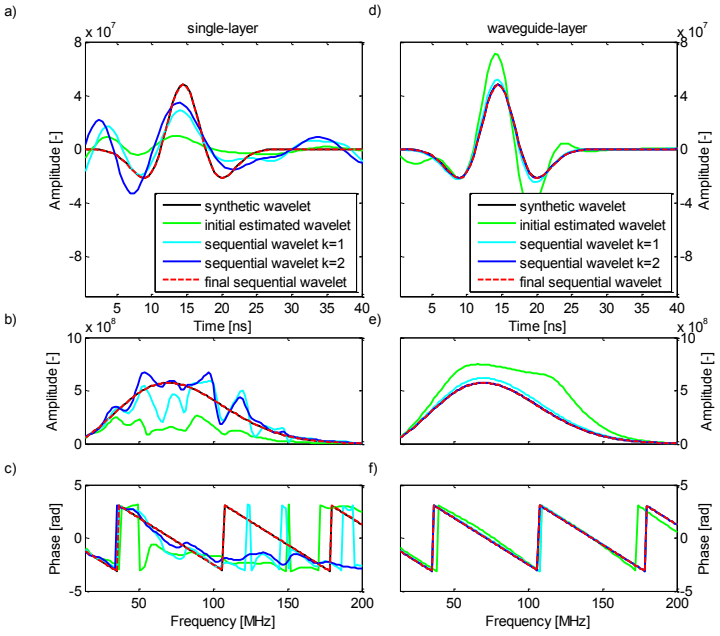

Figure 3.4 The evolution of the effective wavelet during the simultaneous optimization procedure for the (a-c) single-layered and (d-f) waveguide data in time- and frequency domain, respectively. The initial estimated wavelet obtained in step 2 (see Figure 3.1) is plotted in green. The wavelets obtained in step 5 at iterations k = 1, 2 and at the final iterations k = 6, 10 are plotted in light blue, blue and dashed red. Subsequently, the wavelets at iteration k = 6, 10 are used for the simultaneous model optimization.

waveguide. Instead of the geometrical spreading of $1/x^2$ for the ground wave an approximate 2D geometrical spreading of $1/\sqrt{x}$ can be assumed for the waveguide data. The estimation of the conductivity using the 2D geometrical spreading approximation returns σ_1 = 13.14 mS/m for the picked amplitudes between 0.9 - 15.3 m (Figure 3.3b and d), which contains an error of 10 % compared to the true value of σ_1 = 12.00 mS/m (see Table 3.1).

In the following, we will demonstrate the benefit of the full-waveform inversion by discussing the results of the straightforward simultaneous parameter optimization (*Approach 1*), the combined sequential and simultaneous model optimization (*Approach 2*), and the combined sequential and simultaneous model and wavelet optimization (*Approach 3*), respectively.

For each dataset shown in Figure 3.3 we defined, as a worst case scenario, a starting model far away from the true model parameters (Table 3.2 and Table 3.3). The inversions are carried out using 40 frequencies within the frequency range 14 - 200 MHz and 15 offset in

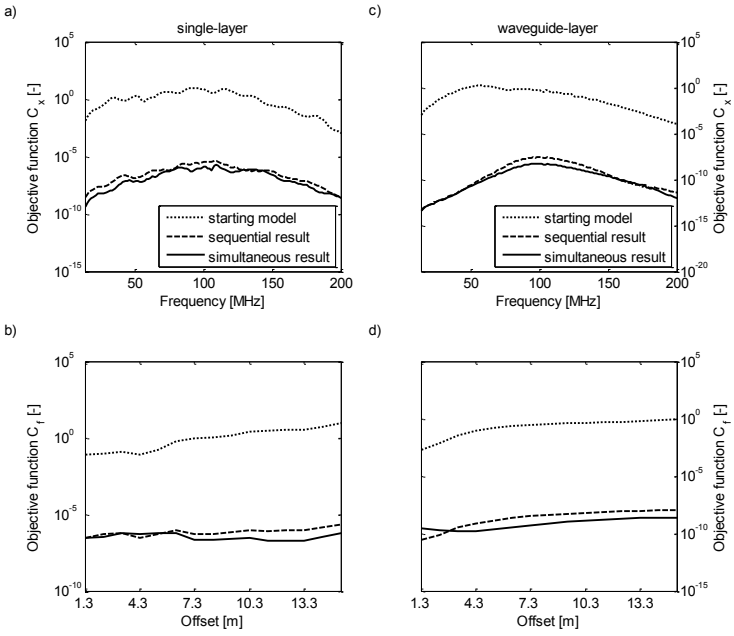

Figure 3.5 Offset and frequency averaged objective function for the (a, b) single- and (c, d) waveguide-layer data, respectively (see equations 3.9 and 3.10) for the starting model (dotted), sequential (dashed) and simultaneous inversion result (solid).

the offset range 1.3 - 15.3 m. For the global search of *Approach 2* and *Approach 3* we defined a percentage deviation to the initial starting model of α_0 = 25% and divided the parameter domain in an equidistant grid with four grid points.

The results of the different inversion approaches are shown in Table 3.2 and Table 3.3. In case of the waveguide data, *Approach 2* and *Approach 3* show comparable results. Both approaches are able to reliably reconstruct the true model parameters. In contrast, the simultaneous parameter optimization while keeping the wavelet fix (*Approach 1)* returns erroneous inversion results. In case of the single-layered data, only *Approach 3* is able to reconstruct the true model parameter. Due to the explicit source wavelet optimization that is carried out simultaneously with the optimization of the medium properties, this approach results in better convergence and is not trapped in a local minimum. In the following we will only use this approach.

The results of the sequential wavelet and model optimization of *Approach 3* for the single-layer and waveguide data are shown in Figure 3.4. Due to the erroneous starting

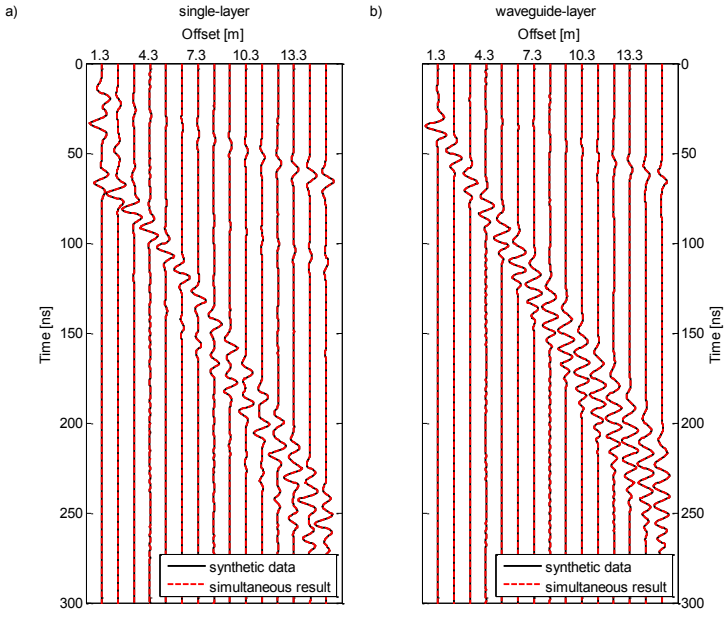

Figure 3.6 Time-domain traces of the synthetic data (black) and the simultaneous optimization result (dashed red) for the single-layer (a) and waveguide data (b). For each trace the amplitudes are normalized to the maximum of the model trace.

model properties, the initial estimated wavelet (green) differs significantly from the true wavelet in the time- and frequency-domain (black). The combined sequential optimization of the wavelet and model parameter followed by a simultaneous optimization of all medium properties while keeping the wavelet fixed leads to a subsequent decrease of the objective function. Especially during the first iterations (k = 1, 2), the wavelets amplitude and phase change considerably (see Figure 3.4). The final sequential optimized wavelet (dashed red) and the true wavelet (black) in Figure 3.4 are in excellent agreement. The medium properties are close to the model properties (Table 3.2 and Table 3.3) and the objective functions C_{fx} are reduced significantly. This is also evident in Figure 3.5, showing the objective functions C_f (b, d) and C_x (a, c) using equations (3.9) and (3.10) for the starting model, the sequential optimization result and the simultaneous optimization result for the single-layer and waveguide data.

To compare the inversion results of both datasets in time domain, we calculated in addition to the frequencies used for the inversion 122 frequencies within the frequency range

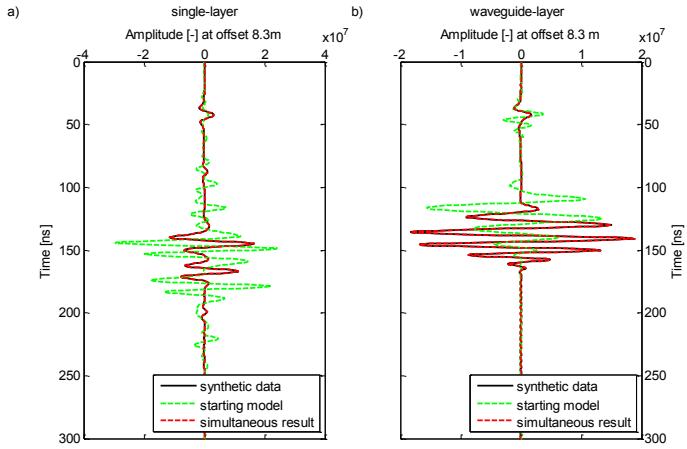

Figure 3.7 Time-domain trace for offset 8.3 m for the single-layer (a) and waveguide data (b) indicating the improvement of the data fit between the synthetic (black), the starting model (dashed green) and the simultaneous result (dashed red).

14 - 200 MHz and carried out an inverse Fourier transformation. Figure 3.6 shows the corresponding trace-normalized time-domain wiggle traces for the synthetic data and simultaneous optimization result whereas Figure 3.7 shows the time-domain plot at offset 8.3 m for synthetic data, the initial starting model and the simultaneous result. The ground wave and reflected waves in the single-layer data as well as the dispersive ground wave in the waveguide data agree very well with modeled data.

3.3 Application to measured data

We use a dispersive waveguide dataset (Figure 3.8) acquired across a terrace of braided river sediments in New Zealand (Yetton, 2002). Due to a thin layer with thickness h of high permittivity material ε_1 (sandy silt) overlying low-permittivity material ε_2 (gravel), waveguide dispersion occurs.

Figure 3.9a shows the corresponding spectral amplitudes as function of the frequency and offset. For larger offsets the signal to noise ratio (SNR) is low which can result in convergence towards a local minimum and return an erroneous result. In order to reduce the influence of noise, we introduce an offset-dependent SNR threshold. All amplitudes below this threshold are excluded from the inversion. For each offset the threshold was calculated

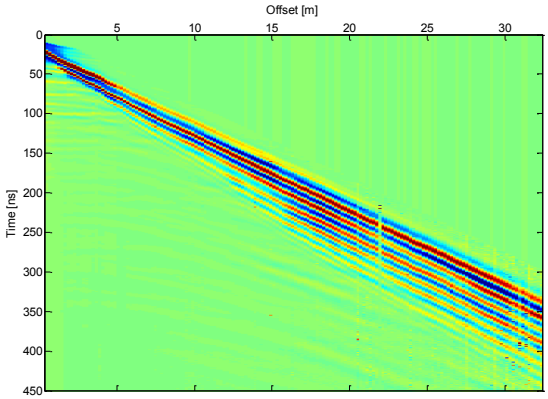

Figure 3.8 Measured dispersive data where the airwave is filtered out and red and blue colors indicate high and low amplitudes which are trace-normalized, respectively.

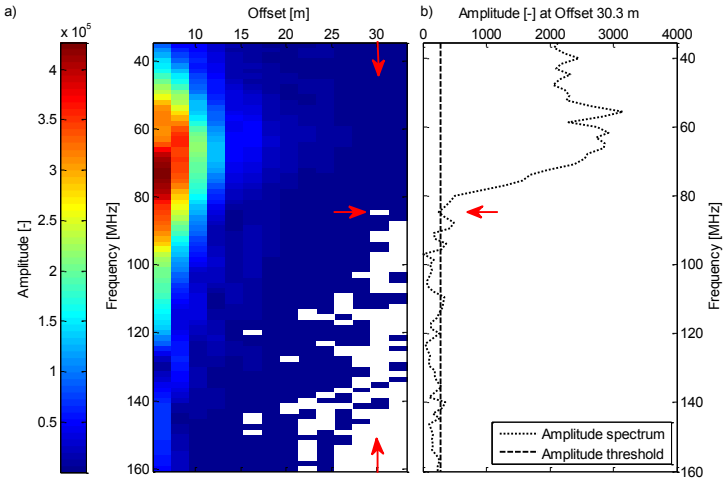

Figure 3.9 (a) the offset and frequency-dependent SNR threshold calculated for all frequencies and offsets within f_N and x_M and (b) the characteristic frequency domain amplitude spectrum (dotted) for the offset 30.3 m and the amplitude threshold (dashed) determined from the SNR average amplitude. Colored cells indicate amplitudes and therefore frequencies above the calculated SNR threshold whereas the red arrows indicate the effect of this threshold. Amplitudes below the SNR threshold (white) are not taken into account during the inversion process.

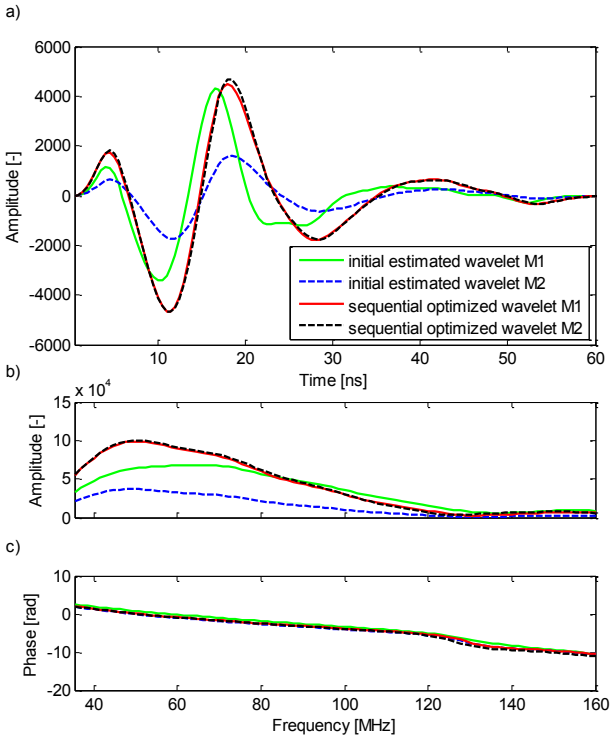

Figure 3.10 Evolution of the effective wavelet showing the time- and frequency-domain spectra of the initial estimated wavelet (blue, dashed green) and the optimized wavelet (red, dashed black) for M1 and M2, respectively. The optimized wavelets are nearly identical.

Table 3.4 Medium properties and objective function C_{fx} for the inversion of measured waveguide data.

	ε_1 [-]	ε_2 [-]	σ_1 [mS/m]	σ_2 [mS/m]	h [m]	C_{fx} [-]
starting model (M1)	20.60	7.50	10.00	0.10	0.18	5.63e-1
sequential inversion result	22.75	7.62	8.65	1.68	0.16	1.60e-1
simultaneous inversion result	23.46	7.62	9.35	1.74	0.15	1.52e-1
starting model (M2)	23.38	7.55	5.50	0.10	0.15	1.21
sequential inversion result	21.16	7.58	7.62	1.78	0.17	1.61e-1
simultaneous inversion result	22.51	7.61	8.92	1.75	0.16	1.53e-1

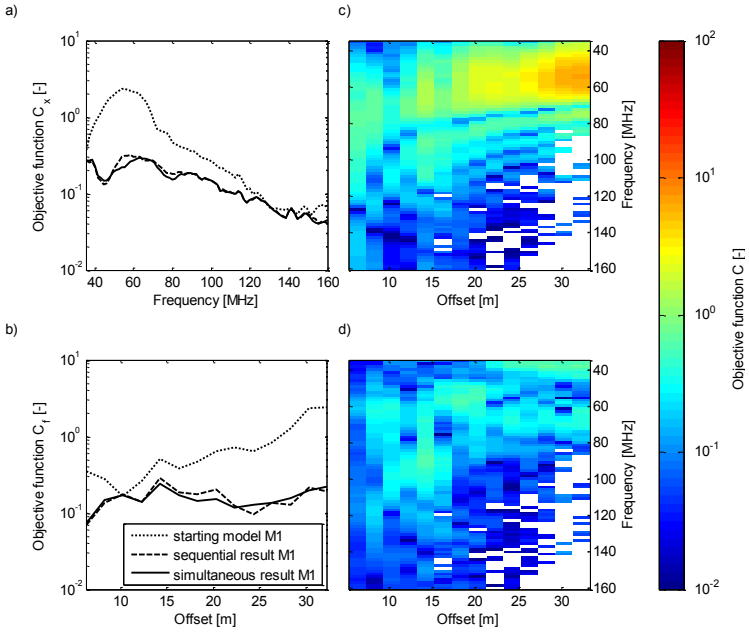

Figure 3.11 Objective function of the measured data and the first model (dotted), the optimized model (dashed) and the final model (solid) of M1 calculated as the sum over (a) the offsets and (b) the frequencies. Figures c) and d) show the evolution of the objective function from the first starting model to the final results calculated for each frequency and offset within f_N an x_M.

by estimating the mean spectral amplitude for frequencies larger than 210 MHz (~ three times the center frequency). Figure 3.9b shows the spectral amplitudes for an offset of 30.3 m and the corresponding threshold. All spectral components below this threshold and therefore frequencies higher than 85 MHz are muted for the corresponding offset in Figure 3.9a.

To test the full-waveform inversion for measured data, we chose two different starting models M1 and M2. Starting model M1 was determined from conventional dispersion inversion (van der Kruk et al. 2006) and returned $\varepsilon_1 = 20.60$, $\varepsilon_2 = 7.50$, $h = 0.18$ m. Since only phase information is used, the dispersion inversion does not return quantitative values for conductivities. Therefore, the electric conductivity for the sandy silt is assumed as $\sigma_1 = 10.00$ mS/m (Davis and Annan, 1989) whereas the conductivity for the gravel is assumed as $\sigma_2 = 0.10$ mS/m. To investigate the robustness of the approach the permittivity and the thickness values for starting model M2 were changed to $\varepsilon_1 = 23.38$, $\varepsilon_2 = 7.55$ and

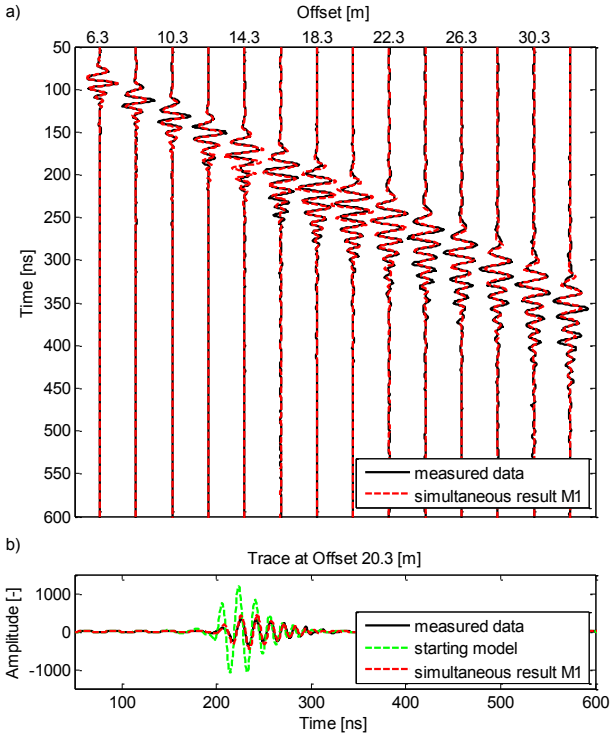

Figure 3.12 Time-domain traces (a) of the measured data (black) and the simultaneous model for M1 (dashed red). In (b), we display the time-domain traces for Offset 8.3 m for the measured data (black), the starting model (dashed green) and the simultaneous inversion result (dashed red). For each trace of (a), the amplitudes are normalized to the maximum amplitude of the measured trace.

h = 0.14 m. The conductivity σ_1 = 5.50 mS/m is estimated using far-field ground wave analysis. The sequential and simultaneous optimization (*Approach 3*) is carried out using 82 frequencies within the frequency range 35 - 160 MHz and 14 offsets within the offset range 6.3 - 32.3 m. For the global search we defined a percentage deviation of α_0 = 25% and subdivided the parameter domain in four equidistant grid points. Figure 3.10 shows the initial estimated and the final sequential optimized wavelet for M1 and M2, respectively. Large misfits in the amplitude of the initial estimated and optimized wavelets indicate wrong conductivity values for the starting model of M1 and M2 whereas small variations in the phase of the initial estimated and optimized wavelets indicate a good starting model for ε_1, ε_2 and h. Table 3.4 shows the obtained model parameters of the entire optimization

process. As already seen for the synthetic single-layer and waveguide data, the sequential optimization of the effective source wavelet and the model parameters followed by the subsequent optimization of ε_1, ε_2, σ_1, σ_2 and h results in a steady decrease of the objective function and a improved fit of the modeled data to the measured data. Figure 3.11a and b show the objective functions C_x and C_f for the starting model and the sequential and simultaneous inversion results, respectively. Figure 3.11c and d show spectral amplitudes for each offset and frequency of the objective function C (3.6) for the starting model and simultaneous optimization result. The white entries correspond to those spectral components having amplitudes less than the SNR threshold. Due to erroneous starting conductivity values, Figure 3.11b and c clearly indicate an increasing objective function for the starting model for increasing offsets. After the combined sequential and simultaneous optimization, the objective function amplitudes are significantly reduced and show a more uniform distribution.

Although the starting models of M1 and M2 differ strongly, the optimization provides comparable values for the material properties which indicate the reliability of the final model obtained by the full-waveform inversion. Figure 3.12a compares the obtained trace-normalized time-domain traces with the measured data and shows that the quantitative medium properties well describe the measured data. As indicated in Figure 3.12b, which shows the time-domain plot at offset 20.3 m for the measured data, the initial starting model and the simultaneous result, the fit to the measured data is significantly improved. It is expected that also the inversion uncertainty is less compared with conventional phase picking and velocity analysis (Jacob and Hermance, 2004).

3.4 Conclusions

A novel frequency-domain full-waveform inversion for surface GPR is presented and applied to synthetic and measured CMP data. A crucial step in the full-waveform inversion is the explicit optimization of the effective source wavelet since it is inherently coupled with the conductivity values of the medium. Therefore, we introduced a sequential phase and amplitude optimization (*Approach 3*) by updating the model parameters and the source wavelet followed by a simultaneous optimization by updating the medium properties while keeping the wavelet fixed. Applying this approach to two single-layered synthetic models clearly show the benefits compared to a more straightforward simultaneous parameter optimization (*Approach 1*) and a combined sequential and simultaneous model optimization (*Approach 2*). In case of the waveguide data *Approach 1* returns an erroneous inversion result, which indicates the need for more sophisticated approach. *Approach 2* and *Approach 3* return comparable results and the model parameter and the source wavelet are well reconstructed (Table 3.2 and Table 3.3). In contrast to the waveguide data, the single-layered dataset is more challenging due to the numerous distinguishable events (ground wave, reflections and multiples), which probably increase the number of local

minima. Applying *Approach 1* and *Approach 2* to the data, neither the model properties nor the source wavelet could be reconstructed. Only the combined sequential and simultaneous wavelet and model optimization in *Approach 3* is able to return reliable inversion results, which indicates that this approach seems to be less sensitive to be trapped in a local minima. The most important reason for this superior behavior is the simultaneous waveform and medium parameter optimization, whereas in *Approach 2* the optimization of the medium properties is driving the wavelet updating. As indicated with *Approach 1* the waveform optimization is also possible while inverting for all subsurface parameters simultaneously, but from our experience this inversion approach is highly sensitive to local minima. Splitting the medium properties in two different parameter groups, as done in *Approach 2* and *3*, serves to significantly reduce the computational effort, since grid searches for three or four parameters require order-of-magnitude fewer forward computations than searches for all subsurface and wavelet parameters. In addition, the simplex search shows a much better convergence behavior for fewer parameters.

In the presence of noise in the data, a SNR threshold is introduced that ensures the robustness of the inversion. Throughout the inversion process of a complex experimental data set containing interfering multiples due to the presence of a low-velocity waveguide, *Approach 3* reduced the misfit of the initial starting model, which was derived from conventional dispersion inversion, significantly. Investigating the robustness of the approach by using different starting models, the presented full-waveform inversion is able to return comparable quantitative values for permittivity and conductivity.

Chapter 4

Improved characterization of fine texture soils using surface GPR full-waveform inversion*

Traditionally, time domain reflectometry (TDR) is the most accurate method to estimate the permittivity and conductivity for the same sensing volume (Topp et al., 1980) at the point scale. A relatively new method to estimate the apparent permittivity of the soil is the Theta probe method operating with a fixed frequency impedance sensor (Gaskin and Miller, 1996). However, compared with TDR results, Theta probe measurements overestimate the water content of the soil by ~1.5 (Robinson et al., 1999) and the performance depends on the texture and compaction of the soil (Sarani and Afrasjab, 2012).
At the field scale, estimates of the apparent electrical conductivity of the soil can be carried out using electromagnetic resistivity tomography (ERT) and electromagnetic induction (EMI) measurements. Many studies have used ERT and EMI measurements to estimate soil properties such as water content and solute concentrations (Ramirez et al., 1993; Zhou et at., 2001) and to obtain electrical conductivity profiles in different sensing depth (Borchers et al., 1997; Hendrickx et al., 2002; Saey et al., 2009).
However, although the traditionally used methods analyzing TDR/Theta probe, ERT and EMI data return estimates of the soil permittivity or conductivity, except the surface GPR FWI none of the currently available methods is able to return two independent medium property estimates for the same sensing volume.
In the previous Chapter we introduced the FWI methodology and applied and verified the inversion for reflected waves present in synthetic single-layer and waveguide data as well as in measured GPR data reflecting a single-layer low-velocity waveguide, where a thin layer of high permittivity sandy silt was overlying low permittivity gravel, respectively.

In this Chapter, we (i) extend the surface GPR full-waveform inversion for the analysis of the direct ground wave, (ii) include an automated time-domain filter to filter out interferences with the direct air wave and reflections, (iii) apply the FWI for fine texture soils with a high variability in the soil water content, (iv) compare the obtained results with Theta probe, ERT and EMI measurements, and (v) correlate the obtained medium permittivities and conductivities with the soil texture (clay, silt, and skeleton) and the wavelet center frequency and amplitude by formulating a linear relationship.

*Adapted from Busch, S., J. van der Kruk, and H. Vereecken, 2012, Improved characterization of fine texture soils using on-ground GPR full-waveform inversion, IEEE Transactions on Geoscience and Remote Sensing, accepted, doi: 10.1109/TGRS.2013.2278297.

4.1 Combined analysis of the soil properties

4.1.1 Selhausen test site

To explore the potential of the full-waveform inversion for a fine textured soil, combined Theta probe, ERT, EMI and GPR measurements were carried out on a silty loam at our test site in Selhausen.

The Selhausen test site of the Forschungszentrum Jülich GmbH is located in the southern part of the Lower Rhine Embayment in Germany. Here, Eolian sediments with a thickness up to 1 m from the Pleistocene and Holocene cover Quaternary sediments, which are mostly fluvial deposits from the Rhine/Meuse river and the Rur river system (Weihermüller et al., 2007). According to the U.S. Department of Agriculture textural classification (USDA) the major soil type is silt loam (Weihermüller et al., 2007). Since the test site is weakly inclined (< 4°), colluvial sediments eroded from the upper part of the test site can be found in the lower part of the test site. The ground water depth shows seasonal fluctuations between 3 m and 5 m below the surface.

A distinct gradient in soil texture is present with a considerably higher stone content at the upper part of the field (Vanderborght et al., 2010). In the upper part of the test site the surface soil contains up to 60 % stones and 10 % at the lower part. Soil samples show that the top soil (0 – 30 cm) contains 54 % skeleton, 14 % sand, 25 % silt and 7 % clay in the upper part of the field compared to 9 % skeleton, 14 % sand, 63 % silt and 14 % clay in the lower part of the field (Figure 4.5).

Due to the geomorphology and soil texture variation, a high variability in the surface soil water content is detectable. Previous studies by Weihermüller et al (2007) and Jadoon et al. (2012) using GPR, TDR and volumetric soil samples showed that a gradient in soil water content and therefore in the permittivity from the upper to the lower part of the field which is partly related to changes in texture.

4.1.2 Measurement setup

Along a profile with a length of 120 m, we combined electrical resistivity tomography (ERT) using the SYSCAL PRO system (IRIS Instruments, Orleans, France) with 120 electrodes and an electrode spacing of 0.25 m in dipole-dipole configuration, electromagnetic induction (EMI) measurements every 1 m in the HCP and VCP orientations with EM38 (Geonics, Mississauga, Ontario, Canada) and GSSI Profiler (Geophysical Survey Systems, Inc., Salem, New Hampshire, United States) in vertical (VCP) and horizontal (HCP) orientation and GPR WARR measurements with unshielded 200 MHz antennas (Sensors & Software Inc., Mississauga, Ontario, Canada) every 10 m. Measurements of the effective permittivity in the top soil were carried out using Theta

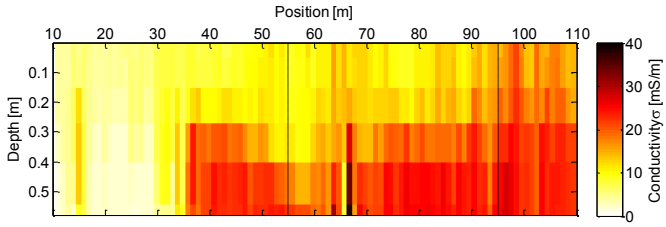

Figure 4.1 Inversion results of the electrical resistivity tomography (ERT) showing lateral and vertical conductivity variations at Selhausen test site. Bright colors indicate low conductivities, dark colors high conductivities.

Probe ML2 sensors (Macaulay Land Use Research Institute, Aberdeen and Delta-T Devices, Cambridge, United Kingdom) every 1 m.

4.2 Results and discussion

4.2.1 ERT and EMI inversion

The ERT data were inverted with the RES2DINV software (Geotomo Software, Penang, Malaysia) and returns a 2-D model consisting of rectangular blocks with a certain resistivity. Optimizing the resistivity (inverse of conductivity) by minimizing the misfit between the calculated and measured ERT data, returns a resistivity pseudo section of the subsurface (Geotomo Software). The inversion result shown in Figure 4.1 clearly indicates the heterogeneity of the Selhausen test site. In the upper part of the test site (10 - 30 m horizontally), the ERT inversion results indicate relative low conductivities of 5 - 10 mS/m and apparently no layering, whereas in the lower part of the test site a high conductive layer (5 - 20 mS/m) with a thickness of 0.4 m is overlying an even more conductive layer (> 20 mS/m).

In contrast to ERT measurements, current EMI systems only return qualitative values for the subsurface conductivity because of instrument calibration difficulties (Triantafilis et al., 2000; Sudduth et al., 2001; Abdu et al., 2007; Gebbers et al., 2009). To overcome these limitations, Lavoué et al. (2010) proposed a method to calibrate EMI measurements with the electrical conductivity values obtained from ERT inversion. Therefore, the conductivity distribution obtained from RES2DINV inversion was used as input in an electromagnetic forward model for synthetic EMI data with the same EMI configurations as used for the experimental measurements. The obtained synthetic EMI data were then used to calibrate the measured data following the procedure described by Lavoué et al. (2010) and inverted

for a two-layer subsurface by minimizing the misfit between the measured and modeled magnetic field following the procedure described by Mester et al. (2011). Note that due to metal objects at the surface the area between 55 and 85 m is excluded from the calibration of the EMI data. The ERT and the EMI inversion results for the upper 30 cm are shown in Figure 4.5c.

4.2.2 GPR full-waveform inversion

The relatively high conductivities at Selhausen test site cause significant attenuation of the electromagnetic waves in the subsurface and therefore a decreasing penetration depth of the GPR with increasing conductivities. Since reflected waves could not be clearly identified in the measured WARR profiles, the data are well suited to verify the extended FWI for the analysis of the DGW. We estimated the initial permittivity and conductivity values for each WARR measurement using a ray-based direct ground expression (van der Kruk and Slob, 2002; Busch et al., 2012; see Chapter 3, equation 3.1).

In contrast to the FWI for a layered subsurface (Chapter 3), for the analysis of the DGW the subsurface is approximated by homogeneous halfspace with only one permittivity and conductivity value.

Here, a crucial step for the inversion process is the effect of the direct air wave (DAW) propagating between the transmitting and receiving antenna. In case of near offsets in the CMP/WARR profiles, the DAW might interfere with the DGW and the analysis of the DGW will become a challenging task since the direct air and ground wave cannot be clearly distinguished. Moreover, in the case of larger offsets the DAW may mask weaker subsurface signals and make them difficult or impossible to see or interpret. Therefore, to minimize the effect of the direct air wave on the DGW full-waveform inversion result, we introduce a time-domain filter which acts on each trace of the data independently. The filter facilitates to define muting areas above and below the direct ground wave and sets all data points within these areas to zero.

The full waveform inversion is performed for each WARR measurement along the 120 m long profile. Table 4.1 gives an overview of the inversion results and indicates the offset range x^{FWI} and the number of traces n_x^{FWI} within x^{FWI} used for the inversion, the initial model for the subsurface permittivity ε^{RB} and conductivity σ^{RB} obtained from ray-based methods, the inverted permittivity ε^{FWI} and conductivity σ^{FWI} as well as the corresponding objective functions C^{RB} and C^{FWI}, respectively.

The WARR profiles after applying a gain function at the receiver position 40 m and 90 m, representing GPR measurements on relative low and higher conductive media, are shown in Figure 4.2a and c, respectively. In both datasets a dominant air-wave is presented which interferes with the ground wave. However, due to these interferences, clipping of the amplitudes for small offsets, the increasing attenuation of the DGW as well as an increasing

Table 4.1 Starting model and simultaneous inversion results obtained from the FWI of the WARR measurements at the receiver positions 10 m, 30 – 50 m, and 80 - 110 m at Selhausen test site. In most cases the same offset range x^{FWI} was used to determine the ray-based (*RB*) and full-waveform (*FWI*) results.

WARR at [m]	ε^{RB} [-]	σ^{RB} [mS/m]	x^{FWI} [m]	n_x^{FWI} [-]	C^{RB} [-]
10	10.56	5.90	1.1-1.5	5	2.09e-1
30	10.70	5.53	1.0-1.6	7	3.33e-1
40	13.35	7.96	0.9-1.6	8	1.72e-1
50	14.91	6.20	0.9-2.3	15	1.72e-1
80	16.42	23.94	0.9-1.6	6	2.38e-1
90	17.36	25.94	0.9-1.6	8	2.12e-1
100	14.22	28.17	0.9-1.8	8	3.76e-1
110	16.93	25.36	0.9-1.7	7	2.54e-1
	ε^{FWI} [-]	σ^{FWI} [mS/m]	x^{FWI} [m]	n_x^{FWI} [-]	C^{RB} [-]
10	12.20	2.39	1.1-1.5	5	1.64e-1
30	8.11	6.08	1.0-1.6	7	2.55e-1
40	14.35	6.26	0.9-1.6	8	1.59e-1
50	14.93	9.82	0.9-2.3	15	1.71e-1
80	18.02	17.68	0.9-1.6	6	1.86e-1
90	17.63	22.93	0.9-1.6	8	1.89e-1
100	17.29	28.45	0.9-1.8	8	2.27e-1
110	18.51	27.72	0.9-1.7	7	2.27e-1

signal-to-noise ratio (SNR) for increasing offsets limits the number of offsets which can be used for the full-waveform inversion (see also Table 4.1).

Figure 4.2b and d show the picked maximum amplitudes of the DGW (black), the fitted far-field decay function (dashed red; see Chapter 3, equation 3.1) and the applied gain function (blue). Note that the inversion of the data is carried out using true amplitudes and no gain function was applied. The initial and inverted model of the subsurface properties as well as the initial (green) and inverted effective wavelets (dashed red) are shown in Table 4.1 and Figure 4.3. Small variations in the phase of the wavelet (c, f) indicate a good permittivity ε starting model obtained from conventional velocity analysis for the WARR measurements at the receiver positions 40 and 90 m. Comparing the initial and inverted wavelet amplitudes (a-b, d-e), especially the wavelet for the WARR at 90 m differs significantly indicating an erroneous initial conductivity σ model.

The time-domain traces of the measured data and the initial and inverted model for the WARR's at 40 m and 90 m are presented in Figure 4.4. Note that the data are trace-normalized to the measured data and therefore show true amplitudes. In contrast to the initial model (dashed green), the measured data (black) and the inverted model (dashed red) are overlying. The significant improvement of the subsurface model is also indicated

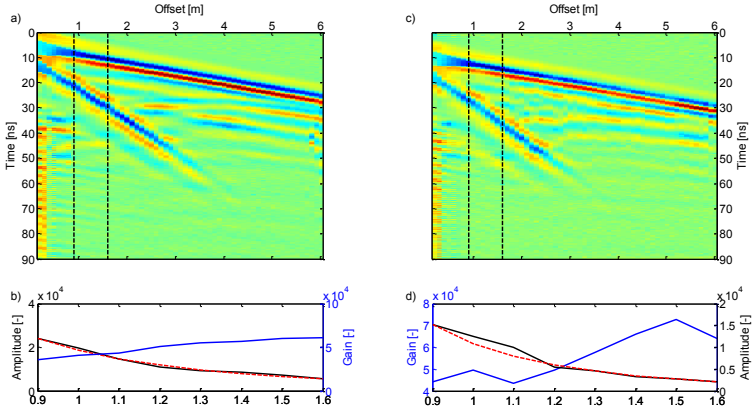

Figure 4.2 Measured WARR after applying a gain function at the receiver positions 40 m (a) and 90 m (b). Red and blue colors indicate trace-normalized positive and negative, respectively. For the inversion, the air wave present in the data is muted out. Dashed black lines indicate the selected offset range x^{FWI} for the full-waveform inversion; c) and d) show the picked maximum amplitudes (black) of the DGW, the fitted ray-based decay function (dashed red) and the applied gain function (blue). Note that for the inversion of the GPR data the true amplitudes without applying a gain function are used.

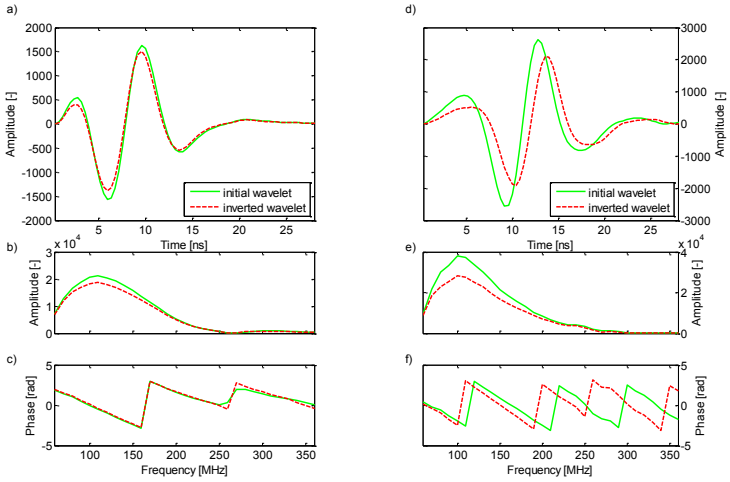

Figure 4.3 Time-domain and frequency-domain amplitude and phase spectra of the initial and inverted effective wavelet for the WARR measurements at the receiver positions 40 m (a-c) and 90 m (d-f).

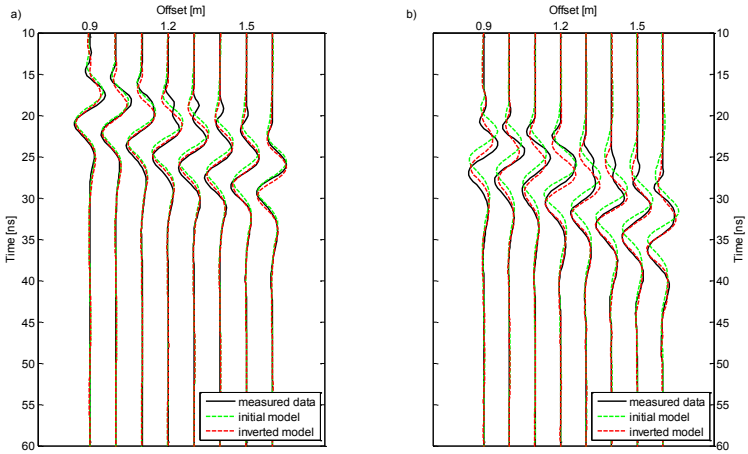

Figure 4.4 Time-domain traces of the measured data and the initial and inverted model for the WARR's at 40 m (a) and 90 m (b). The amplitudes are trace-normalized to the measured data and show true amplitudes.

by the decrease in the objective functions C^{RB}, obtained from ray-based methods, and C^{FWI}, obtained from the full-waveform inversion (see Table 4.1). For the WARR measurement at the receiver position at 40 m the objective functions C^{RB} of the ray-based model in Table 4.1 decreases by 8 %, whereas the objective function C^{RB} for the WARR at 90 m decreases by 11 %.

Figure 4.5, Table 4.2 and Table 4.3 show the grain size distribution at Selhausen test site and the results of the combined Theta probe, ERT, EMI and GPR measurements. For the depth of 0 – 30 cm, Figure 4.5a clearly indicate an increasing clay (green, 7 – 14 %) and silt (red, 25 – 63 %) content, a constant sand content (blue, 13 – 14 %) and a decreasing skeleton content (dashed black, 54 – 9 %) for increasing position. The permittivity values obtained from Theta probe (blue, 11.36 – 17.41) measurements, the GPR^{RB} ray-based technique (dashed black, 10.56 – 16.93) and the GPR^{FWI} full-waveform inversion (black, 8.11 – 18.01) are shown in Figure 4.5b. The increasing permittivities observed with increasing WARR positions are consistent with increasing clay and silt content and a decreasing skeleton content. The conductivity values obtained from ERT (green, 4.26 – 19.10 mS/m) and EMI (red, 5.24 – 19.34 mS/m) inversions as well as the values obtained from GPR^{RB} (dashed black, 2.39 – 28.45 mS/m) and GPR^{FWI} (black, 5.53 – 28.17 mS/m) are shown in Figure 4.5c. Since only the ground wave is used for the full-waveform inversion of the GPR data, which is travelling through the upper ~30 cm of

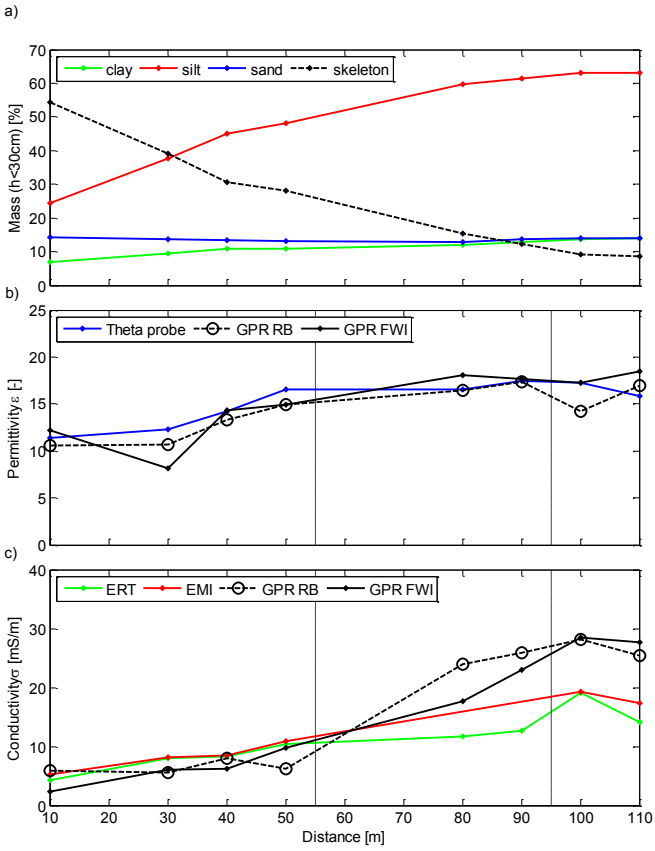

Figure 4.5 Results of the measurements. a) The grain size distribution at the Selhausen test site for 0 – 30 cm depth shows increasing clay and silt content, a rather constant sand content and a decreasing skeleton content for increasing position. The permittivity ε values (b) obtained from Theta probe (blue) measurements, GPR^{RB} ray-based techniques (dashed black) and GPR^{FWI} full-waveform inversion (black) as well as the conductivities σ values (c) obtained from ERT, EMI, GPR^{RB} and GPR^{FWI} increase for increasing positions. Between 55 and 95 m metal objects and cables at and in the subsurface influence the geophysical measurements.

the subsurface (Galagedara et al., 2005a; 2005b), the GPR conductivities in Figure 4.5c are compared with the mean ERT and EMI conductivities for the depth 0 – 30 cm. Here, especially at the WARR positions at 50, 80 and 90 m where the fine texture soil content

Table 4.2 Soil texture content at the WARR measurements at the receiver positions 10 m, 30 – 50 m, and 80 - 110 m at Selhausen test site.

WARR at [m]	Clay [%]	Silt [%]	Sand [%]	Skeleton [%]
10	7	25	14	54
30	9	38	14	39
40	11	45	13	31
50	11	48	13	28
80	12	60	13	15
90	13	61	14	12
100	14	63	14	9
110	14	63	14	9

Table 4.3 Permittivities and conductivities obtained from the combined Theta probe, ERT, EMI and GPR measurements at Selhausen test site.

WARR at [m]	ε^{TP} [-]	ε^{GPR} [-]	σ^{ERT} [mS/m]	σ^{EMI} [mS/m]	σ^{GPR} [mS/m]
10	11.36	12.20	4.26	5.24	2.39
30	12.29	8.11	7.95	8.16	6.08
40	14.24	14.35	8.38	8.47	6.26
50	16.60	14.93	10.33	10.87	9.82
80	16.54	18.02	11.76	-	17.68
90	17.41	17.63	12.62	-	22.93
100	17.26	17.29	19.10	19.34	28.45
110	15.82	18.51	14.14	17.31	27.72

increases, conventional used ground-wave picking GPR^{RB} returns either lower or higher conductivity values than the ERT, EMI and GPR^{FWI} techniques. Although each method has different sensing depth and frequency range, and the results are therefore not directly comparable, these methods indicate a similar trend in the electric properties of the soil. Between 55 and 95 m metal objects at the surface and cables in the subsurface (60 – 70 m) influence the geophysical measurements. Therefore, ERT and EMI measurements within this offset range are not used for the calibration of the EMI data.

Figure 4.6 shows the correlations between the subsurface conductivity (measured with GPR, ERT and EMI), the permittivity (measured with GPR and Theta probes) and the soil texture at Selhausen test site. As already seen in Figure 4.5c and d, the GPR^{FWI} conductivities and permittivities increase with increasing clay and silt content, i.e. with increasing content of fine texture soil (Figure 4.6 a-b, e-f), whereas the conductivities and permittivities decrease with increasing skeleton content, i.e. with increasing coarse texture

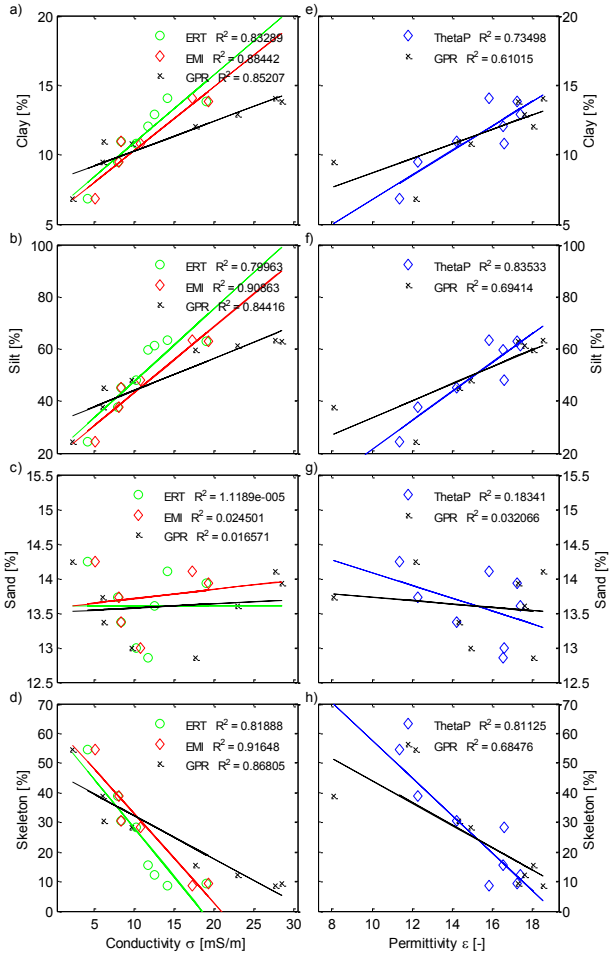

Figure 4.6 Correlations between the subsurface conductivities obtained from measured with ERT, EMI and GPR inversion, the permittivities obtained from Theta probe measurements and GPR inversion, and the soil texture at Selhausen test site, respectively. The conductivity and permittivity increases with increasing clay and silt content (a-b, e-f), whereas the σ and ε decrease with increasing skeleton content (d, h). Due to a constant sand constant there is no correlation with increasing σ and ε from the upper to the lower part of the test site (c, g).

soil (Figure 4.6, d-h). The corresponding correlation coefficients R^2 between 0.80 and 0.98 indicate a strong linear relationship between conductivity, permittivity and soil texture (clay, silt, skeleton). Due to a relatively constant sand content there is no correlation with the increasing conductivity and permittivity (Figure 4.6, c-g) for increasing position. These results are in good agreement with the results of Theta probe, ERT and EMI measurements which indicates the reliability of the surface GPR full-waveform inversion.

Figure 4.7 shows the three-dimensional correlation between the permittivity and conductivity values obtained from the GPR full-waveform inversion and the clay (a) silt (b) and skeleton (c) content. Calculating the correlation coefficients returns R^2_{clay} = 0.55, R^2_{silt} = 0.81 and $R^2_{skeleton}$ = 0.44 and clearly indicates a linear relation between the clay, silt and skeleton content and the subsurface permittivity and conductivity. This relationship can be parameterized by an orthogonal distance regression

$$\begin{pmatrix} x \\ y \\ z \end{pmatrix} = \begin{pmatrix} x_0 \\ y_0 \\ z_0 \end{pmatrix} + \begin{pmatrix} v_x \\ v_y \\ v_z \end{pmatrix} \cdot d, \tag{4.1}$$

where (x, y, z) is a data point, (x_0, y_0, z_0) is the point on the regression line L, (v_x, v_y, v_z) is the vector defining the direction of L and d is the distance whose value is varied to define the point (x_0, y_0, z_0) on L. Minimizing the sum of square distances from (x_0, y_0, z_0) to L returns the best fitting line with the direction (v_x, v_y, v_z). The orthogonal distance regression for the soil texture and the permittivity ε and conductivity σ values obtained from the full-waveform inversion is parameterized by

$$\begin{pmatrix} \varepsilon \\ \sigma \\ M_{clay} \end{pmatrix} = \begin{pmatrix} 15.13 \\ 15.17 \\ 11.36 \end{pmatrix} - \begin{pmatrix} 0.27 \\ 0.94 \\ 0.20 \end{pmatrix} \cdot d, \tag{4.2}$$

$$\begin{pmatrix} \varepsilon \\ \sigma \\ M_{silt} \end{pmatrix} = \begin{pmatrix} 15.13 \\ 15.17 \\ 50.32 \end{pmatrix} - \begin{pmatrix} 0.17 \\ 0.57 \\ 0.80 \end{pmatrix} \cdot d, \tag{4.3}$$

$$\begin{pmatrix} \varepsilon \\ \sigma \\ M_{skeleton} \end{pmatrix} = \begin{pmatrix} 15.13 \\ 15.17 \\ 24.73 \end{pmatrix} - \begin{pmatrix} 0.16 \\ 0.52 \\ -0.84 \end{pmatrix} \cdot d, \tag{4.4}$$

where M_{clay}, M_{silt} and $M_{skeleton}$ are the clay, silt and skeleton content, respectively.

Figure 4.8 shows the inverted data-driven effective wavelets for the WARR's at the receiver positions 10 m, 30 – 50 m, and 80 - 110 m in time-domain (Figure 4.8a) and the corresponding amplitude spectra in frequency-domain (Figure 4.8b). Here, the zero crossings are aligned to enable a comparison of the wavelet shape and amplitude. Although the amplitude of the effective wavelets differs at each midpoint position, the shape of the wavelets is similar. Figure 4.9a shows the normalized wavelets (black) from Figure 4.8a as well as the calculated mean wavelet (red). With increasing permittivity ε and conductivity

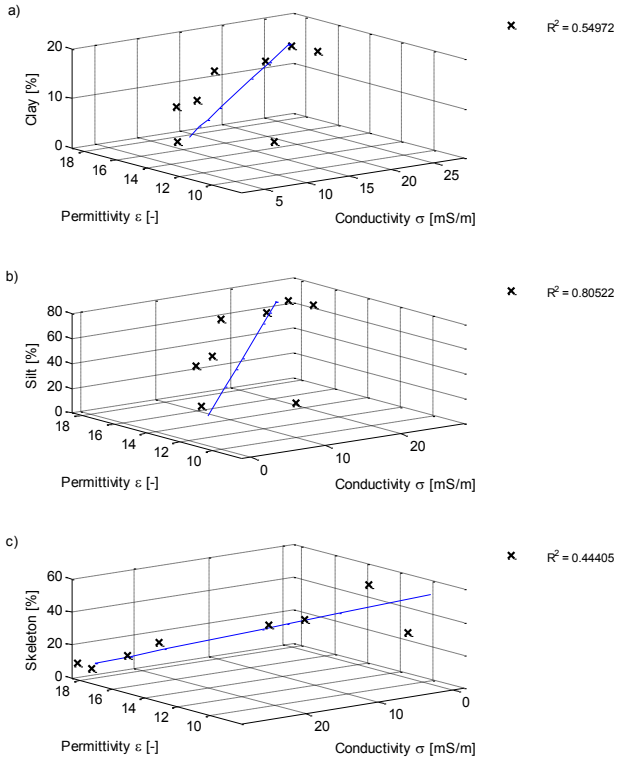

Figure 4.7 Correlation between permittivity, conductivity and texture of the soil indicate a linear relationship for fine texture (clay and silt, a-b) and coarse texture soil (skeleton, c).

σ values for increasing position the wavelet center frequency f_c shifts to lower frequencies (Figure 4.9c), whereas the wavelet amplitude $\hat{W}_A(f_c)$ increases (Figure 4.9b). This is also obvious in Figure 4.10, where f_c and $\hat{W}_A(f_c)$ show a strong correlation with σ and ε. The correlation coefficients R^2 in the range of 0.44 - 0.94 clearly indicate that the effective wavelet is affected by the subsurface properties.

For a half wavelength dipole antenna in a homogeneous space, the resonance frequency depends on the relative permittivity of material surrounding the antenna, which in turn depends on the permittivity of the material supporting the metal antenna, the air, the ground

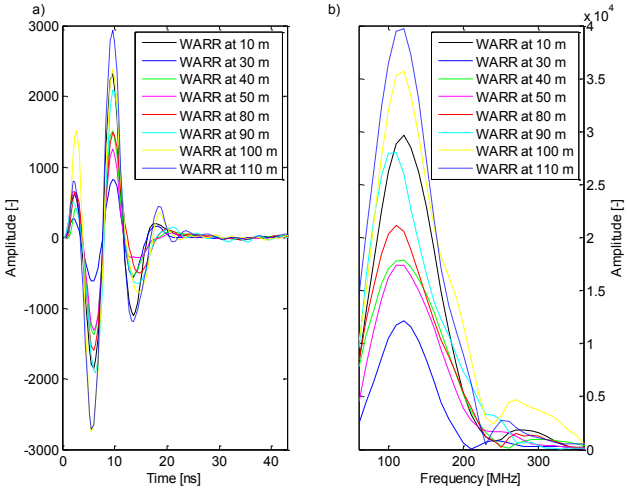

Figure 4.8 Data-driven time-domain (a) and frequency-domain amplitude (b) and phase spectra (c) of the optimized wavelets the WARR's at 10 m, 30 – 50 m, and 80 - 110 m. Note that the wavelets are normalized to the wavelet with the maximum Amplitude (WARR at receiver position 110 m) and thus shifted in time.

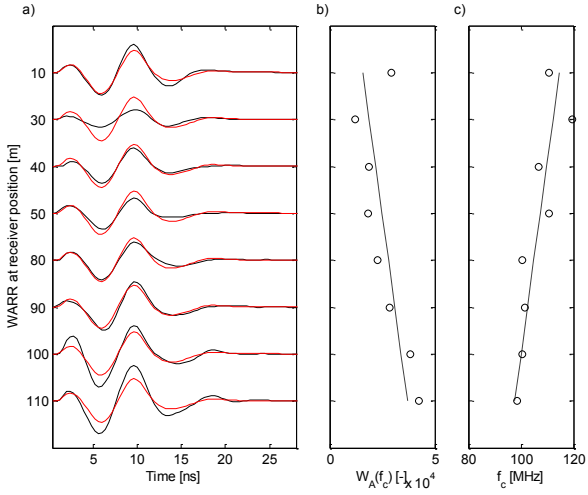

Figure 4.9 Normalized time-domain source wavelet (a) for the WARRs at 10 m, 30 – 50 m, and 80 - 110 m (black) and the calculated mean wavelet (red); (b) and (c) indicate the corresponding maximum wavelet amplitude and center frequency.

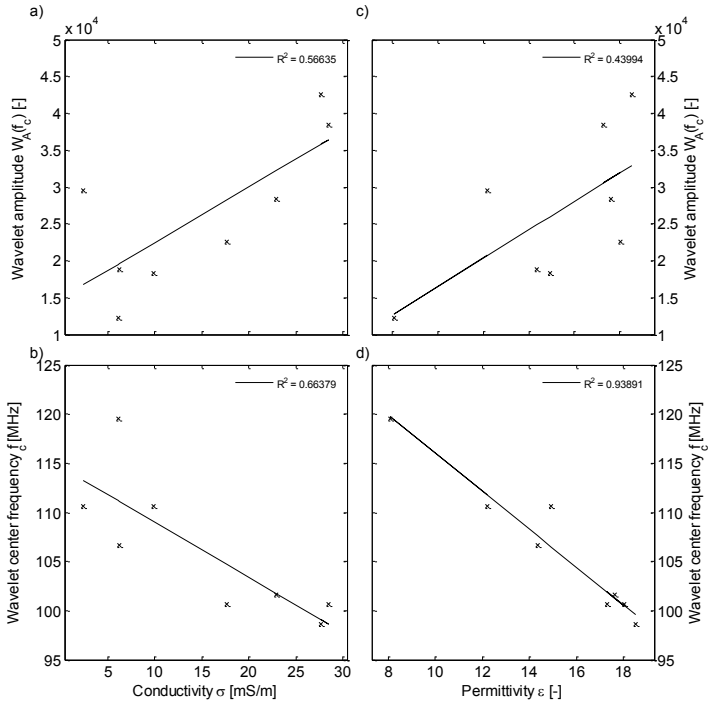

Figure 4.10 Correlations between the wavelet center frequency and amplitude and the subsurface permittivity and conductivity, respectively. The correlations indicate an increasing wavelet amplitude W_A with increasing conductivities σ and ε (a, b) and a decreasing wavelet center frequency f_c with increasing σ and ε (c, d).

material- and roughness and the antenna height (Loeffler and Bano, 2004). For an increasing permittivity ε, the antenna appears to be electrically longer resulting in a decrease of the antenna center frequency f_c. In addition, due to a decrease in f_c, the antenna system emits more low-frequency energy which in turn results in an increasing wavelet amplitude $\hat{W}_A(f_c)$. All inverted wavelet characteristics are consistent with the changing electrical length of the antenna and the radiation characteristics for ground coupled antennas. Note that using full-waveform inversion also quantitative values for the wavelet center frequency and amplitude are obtained that might also be used for an improved characterization of the subsurface. In addition, radiation patterns of horizontal electric dipoles show that the wave energy emitted in the subsurface, characterized by $\hat{W}_A(f_c)$, is increasing with increasing permittivity (Engheta et al., 1982; Sensors and Software Inc.,)

and conductivity (Slob and Fokkema, 2002), which seem to dominate the decreasing radiated power due to a possible deterioration of the impedance matching condition.

4.3 Conclusions

A recently developed full-waveform inversion approach for surface GPR was extended and verified for the inversion of the direct ground wave to characterize the shallow part of the subsurface. In the case of surface GPR CMP/WARR data the proposed method indicates the high information content present in GPR data. The permittivity and conductivity values obtained from the inversion of WARR data measured on a silty loam are in very good agreement with the results obtained from conventional used Theta probe (effective dielectric permittivity), ERT and EMI measurements (electric conductivity), respectively. Here, in contrast to conventional used GPR ray-based techniques, the FWI returns reliable conductivity values especially for conductive fine texture soils.

Since the novel inversion approach enables to obtain permittivity and conductivity values for the same sensing volume, this technique also allows to formulate an orthogonal distance regression parameterization between the soil electrical properties and texture (clay, silt, skeleton). Moreover, strong correlations between the subsurface permittivity and conductivity and the wavelet amplitude and center frequency clearly show the benefits of the surface GPR FWI for the improved characterization of the subsurface and indicate the need for an accurate estimated source wavelet for ground coupled GPR antennas.

Chapter 5

Coupled hydrogeophysical inversion of time-lapse surface GPR data to estimate hydraulic properties of a layered subsurface*

In Chapter 3 and 4 we introduced the quantitative permittivity and conductivity estimation for coarse and fine texture soils using the full-waveform inversion. Since reliable estimates of the soil water content can be obtained using the subsurface permittivity and conductivity in combination with petrophysical relationships such as the Complex Refractive Index Model (CRIM) or empirical relationships such as Topp's equation and Archie's law, the FWI improves the characterization of the subsurface. However, a major challenge in vadose zone hydrology is to obtain accurate information on the temporal changes of the vertical soil water distribution and its feedback with the atmosphere and groundwater. A variety of non-invasive geophysical techniques are routinely used to monitor shallow soil conditions and may provide valuable estimates of soil hydraulic parameters needed for hydrological model parameterization.

Within the last decade, the estimation of water content profiles (WCP) along the TDR probe based on modeling of TDR wave propagation has become possible (e.g., Heimovaara et al., 2004; Leidenberger et al., 2006; Greco, 2006; Greco and Guida, 2008). Such estimation of water content variations along the length of the probe also provides the necessary information to estimate soil hydraulic properties using inverse modeling.

Promising techniques to characterize dynamic processes in the subsurface are time-lapse geophysical surveys in combination with coupled inversion schemes where a hydrological model of the subsurface is combined with a geophysical forward model. (Ferré et al., 2009). Recently, Hinnell et al. (2010) described the advantages and assumptions of the coupled inversion approach in detail. Compared to conventionally used sequential inversion approaches, where the measured geophysical data and the hydrological model are inverted independently, the error propagation from the data inversion to the hydrological model inversion is minimized (e.g. Hinnell et al. 2010; Mboh et al., 2011).

Time-domain reflectometry (TDR) has been commonly used to estimate soil water content and to gain knowledge about soil hydraulic properties (Robinson et al., 2003). Amongst others, Wollschläger et al. (2009) and Bauer et al. (2012) used this type of TDR information to estimate the hydraulic properties of a layered soil profile using inverse modeling.

*Adapted from Busch, S., L. Weihermüller, J. A. Huisman, C. M. Steelman, A. L. Endres, H. Vereecken, and J. van der Kruk, 2013, Coupled hydrogeophysical inversion of time-lapse surface GPR data to estimate hydraulic properties of a layered subsurface, Water Resources Research, accepted.

Ground penetrating radar (GPR) techniques provide a good alternative for characterizing soil moisture dynamics (Huisman et al., 2003). Similar to TDR, GPR techniques are based on electromagnetic (EM) wave propagation. Given the non-invasive nature and potential depth of investigation, surface GPR methods such as reflection profiling and common midpoint (CMP) sounding are promising hydrogeophysical methods for obtaining hydrological information. However, there have been no previous studies focusing on coupled inversion of surface GPR field data for hydrological parameter estimation. Recently, Steelman et al. (2012) conducted an extensive 26 month field study covering two contrasting annual cycles of soil conditions typical of mid-latitude climates. In that study, GPR reflection profiling and CMP soundings were carried out in a daily to weekly interval to characterize vertical soil water dynamics within the vadose zone. This unique data set revealed the highly variable nature of soil water content in the upper 3 meters over both seasonal and shorter time scales. To examine the potential information content of their GPR-derived soil water profiles for estimating hydraulic parameters, Steelman et al. (2012) compared their GPR observations with soil water flow simulations using a one-dimensional hydrological model (HYDRUS-1D) parameterized with laboratory-derived Brooks-Corey (BC) soil hydraulic properties (Brooks and Corey, 1966) obtained from repacked soil samples. Here, the simulated and measured results of Steelman et al. (2012) matched fairly well and the authors hypothesized that the good fit between their uncalibrated modeling results and GPR-derived soil moisture estimates provided strong evidence that surface GPR data can be used for soil hydraulic parameter estimation.

In this Chapter we extend the analysis of Steelman et al. (2012) and assess the feasibility of estimating soil hydraulic properties of a layered subsurface using a coupled hydrogeophysical inversion scheme applied to surface GPR data, where measured interval velocities and travel times were combined with a hydrological model of the subsurface. First, a synthetic surface GPR data set was used to determine whether these data sets contain sufficient information for the estimation of soil hydraulic properties of a multi-layered medium. Afterwards, our coupled inversion approach was applied to the data set of Steelman et al. (2012) to examine its performance when applied to real field data.

5.1 Methodology

Time-lapse GPR reflection profiling and common-midpoint (CMP) measurements were used to characterize soil moisture dynamics in the subsurface. Although water content can be directly calculated from GPR velocity analysis using petrophysical and empirical relationships, such as the Complex Refractive Index Model (CRIM; Wharton et al., 1980) and Topp's equation (Topp et al., 1980), the estimation of soil hydraulic properties is not feasible if the movement of water over time and depth is unknown. Here, we used time-lapse GPR data measured on an agricultural test site to obtain in situ travel times and

interval velocities that reflect water content changes in the upper few meters of the vadose zone, enabling the estimation of unsaturated soil hydraulic properties over discrete depth intervals. A hydrological model with input from a nearby weather station was used to generate water content distribution dynamics that are converted to GPR travel times and interval velocities using the CRIM model at those dates when the GPR data were measured. The misfit between the simulated and observed GPR travel times and interval velocities was minimized by updating the parameters of the hydrological model using the shuffled complex evolution approach (SCE-UA) as described by Duan et al. (1992).
The GPR data used in this study were initially analyzed by Steelman et al. (2012) and they described the field methodology and interpretation of the results needed for the current analysis in detail. A brief summary of that information is provided below.

5.1.1 Test site

The monitoring transect of the time-lapse GPR and soil water content measurements was positioned on top of a local sandy hill characterized by interbedded fine to coarse sand. GPR common-offset profiling and CMP soundings were carried out in a daily to weekly interval (Steelman et al., 2012). Based on nearby water bodies and geophysical measurements, the local water table is expected at a depth of 15 – 20 m below the ground surface. During the study period, no agricultural management operations such as plowing and tillage were performed.
Detailed soil physical properties of the study site were obtained from soil samples down to a depth of 1.6 m, which were extracted at the end of the experiment on a fresh trench wall. The exposed vertical section of the soil was characterized by a 0.25 m dark colored plough horizon composed of coarse sand containing approximately 1.5% (wt/wt) organic material and 3% (wt/wt) silt fraction overlying clean, well-sorted sequences of fine to coarse grained sand layers with a thickness ranging from centimeters to decimeters.

5.1.2 Interval velocity and depth model estimation from GPR data

For the interval velocity and depth model obtained from the GPR survey (see Figure 5.1 and Figure 5.2), a layered subsurface was used in which suitable reflections in common-offset profiles and CMP data (i) are laterally continuous with consistent vertical separation across the monitoring profile, (ii) correspond to major stratigraphic boundaries, and (iii) are clearly identifiable in both the reflection and CMP data. Figure 5.1a shows a characteristic GPR CMP data set that clearly shows four reflections coming from major stratigraphic boundaries present at the test site and Figure 5.1b indicates the associated ray paths. Conventional normal moveout (NMO) velocity and travel time analysis of the reflected waves were carried out by Steelman et al. (2012). For each CMP data set, the semblance

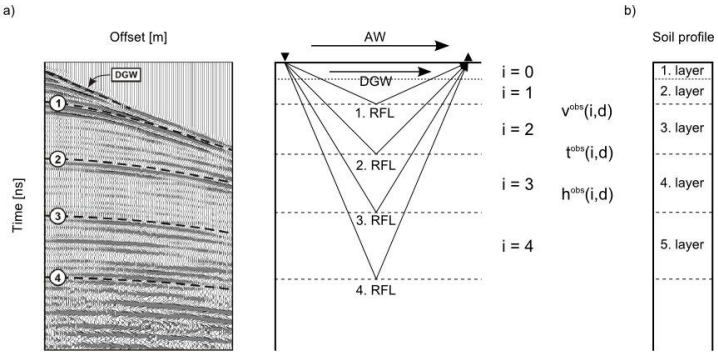

Figure 5.1 Measured CMP data (a) and model of a layered soil profile obtained from the measured CMP data (a) used for the coupled hydrogeophysical and the corresponding ray-paths of the air-wave (AW), the direct ground-wave (DGW), and the reflections (RFL) in the interval $i = 0, \ldots, I$; b) corresponding soil profile validated by pitting and coring directly below the survey line after the study period.

velocity spectrum was calculated and the "first break" of the GPR wavelet was picked to extract the velocity information (Steelman et al., 2012). Successive pairs of NMO velocity and travel time were then used to calculate an interval velocity and depth model of the layered subsurface (Figure 5.1b).

Since the intervals are defined by stratigraphic boundaries, the layer depth and therefore the interval thickness is assumed to be constant during the entire inversion process. The calculated interval velocity $\mathbf{v}^{obs}(i,d)$, travel time $\mathbf{t}^{obs}(i,d)$, and the thickness of the interval $\mathbf{h}^{obs}(i,d)$ (Figure 5.2, left column) corresponds to the number of the observed reflections $i = 1, \ldots, I$ and the observation days $d = 1, \ldots, D$. The available data consists of 75 GPR observation days that reflect the water content changes for each layer.

To further characterize the plough horizon in the uppermost 0.25 m we introduce the top soil layer by the interval $i = 0$. The wave velocity $\mathbf{v}^{obs}(i=0,d)$ associated with this layer was taken from the direct ground wave (DGW) travelling through the shallow subsurface (Galagedara et al., 2005a; 2005b). Since $i = 1$ also includes the DGW interval, this will result in an irregular weighting during the inversion process. Therefore, the interval velocity $\mathbf{v}^{obs}(i=1,d)$, travel time $\mathbf{t}^{obs}(i=1,d)$, and the layer thickness $\mathbf{h}^{obs}(i=1,d)$ of the interval $i = 1$ were recalculated by

$$\mathbf{t}^{obs}\left(i=1,d\right)=\frac{\mathbf{h}^{obs}\left(i=1,d\right)}{\mathbf{v}^{obs}\left(i=1,d\right)}-\frac{\mathbf{h}^{obs}\left(i=0,d\right)}{\mathbf{v}^{obs}\left(i=0,d\right)}, \tag{5.1}$$

$$\mathbf{v}^{obs}\left(i=1,d\right)=\frac{\mathbf{h}^{obs}\left(i=1,d\right)-\mathbf{h}^{obs}\left(i=0,d\right)}{\mathbf{t}^{obs}\left(i=1,d\right)}. \tag{5.2}$$

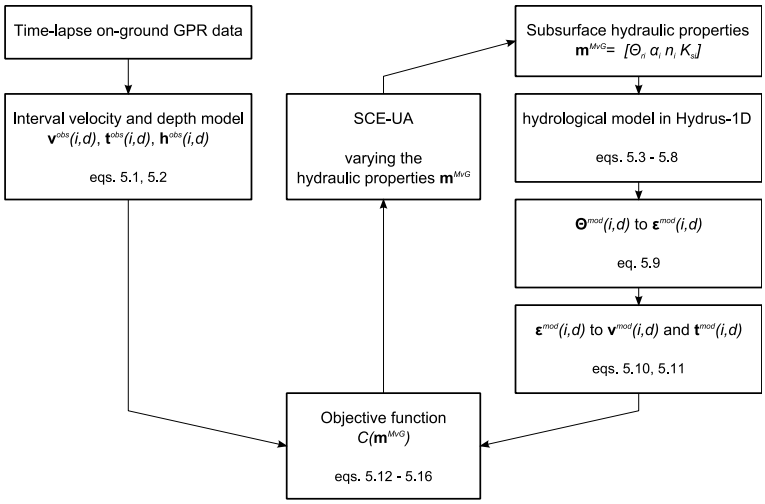

Figure 5.2 Overview of the coupled hydrogeophysical of time-lapse surface GPR data to estimate the hydraulic properties of a layered subsurface, where θri is the residual water content [cm^3/cm^3], α_i [1/cm] and n_i [-] are empirical parameters and K_{si} [cm/d] is the saturated hydraulic conductivity in the interval $i = 0, \ldots, I$.

Note that although the calculated interval velocity information is complementary to the travel time for a fixed interval thickness $\mathbf{h}^{obs}(i,d)$, they still contain partly independent information especially for the intervals $i = 0, 1$.

5.1.3 Hydrological model with film flow

The water flow simulations (Figure 5.2, right column) were performed using the HYDRUS-1D model (Šimůnek et al., 2008), which solves the one-dimensional Richards equation for variably saturated water flow with

$$\frac{\partial \theta(h)}{\partial t} = \frac{\partial}{\partial z}\left[K(h)\left(\frac{\partial h}{\partial z}+1\right)\right] - S, \tag{5.3}$$

where $\theta(h)$ is the water content as a function of the pressure head, θ is the volumetric water content [cm^3/cm^3], h is the pressure head [cm], t is the time [d], z is the positive upward spatial component [cm], and $K(h)$ is the hydraulic conductivity [cm/d] as a function of h. The sink term S describes the volume of water removed from a unit volume of soil due to plant water uptake and is defined by the relation of Feddes et al. (1978) as

$$S(h) = \alpha(h) S_P, \tag{5.4}$$

where $\alpha(h)$ is root water uptake function and S_P is the potential water uptake rate (Šimůnek et al., 2008). Climatic data obtained from the University of Waterloo weather station located approximately 7 km east of the test site. Because the plot was covered by short grass, root water uptake was parameterized with the pressure head values h_0 = -10 cm, h_{opt} = -25 cm, h_{2H} = -200 cm and h_{2l} = -800 cm. The maximum potential transpiration rates r_{2H} and r_{2L} were set to 0.5 and 0.1 cm/d, respectively, and the pressure head h_3 to -8000 cm. Rooting depth was assigned to reach -15 cm depth, which corresponds to the rooting depth observed at the field plot. The lower boundary was set to free drainage and the overall domain size of 1000 cm was discretized with 1001 equidistant nodes.

The soil water retention function, $\theta(h)$, is described by the Mualem-van Genuchten model (Mualem, 1976; van Genuchten, 1980):

$$\theta(h) = \theta_r + \frac{\theta_s - \theta_r}{\left(1 + |\alpha h|^n\right)^m}, \tag{5.5}$$

where θ_r is the residual water content [cm^3/cm^3], α [1/cm] and n [-] are empirical parameters related to the air entry pressure value and the width of the pore size distribution, respectively, and m is restricted by the Mualem condition to $m = 1 - 1/n$ with $n > 1$. Compared to the Brooks-Corey relationship used by Steelman et al. (2012), the Mualem-van Genuchten parameterization offers more degrees of freedom in inverse modeling and less prone to numerical issues when solving equation (5.3). The relative unsaturated hydraulic conductivity $K_r^{cap}(h)$ [cm/d] due to capillarity can be calculated as a function of pressure head as follows:

$$K_r^{cap}(h) = \frac{\left[\left(1 - |\alpha h|^{mn}\right)\left(1 + |\alpha h|^n\right)^{-m}\right]^2}{\left(1 + |\alpha h|^n\right)^{m\lambda}}, \tag{5.6}$$

where λ [-] is a factor that accounts for pore tortuosity and is set to 0.5. This set of equations is often used to describe capillary fluid flow in a porous media, and allows an appropriate description of the water flow under relatively wet conditions (van Genuchten, 1980).

In relatively dry conditions where capillary flow becomes negligible in comparison to film flow, this modeling approach (equation 5.6) sometimes fails (Lenormand, 1990; Toledo et al., 1990; Goss and Madliger, 2007). To overcome this limitation, we extend equation (5.6) with a simple empirical approach to describe water flow in films as a function of pressure head with an additional free fitting parameter τ [-] following Peters and Durner (2008):

$$K_r^{film}(h) = \left[\left(1 + |\alpha h|^n\right)^{-m}\right]^\tau. \tag{5.7}$$

The relative hydraulic conductivity $K_r(h)$ as a function of pressure head can then be described by adding the contributions of capillary $K_r^{cap}(h)$ and film flow $K_r^{film}(h)$ according to:

$$K_r(h) = (1-\omega)K_r^{cap}(h) + \omega K_r^{film}(h), \tag{5.8}$$

where ω [-] is the relative contribution of the film flow with $0 < \omega < 1$ (Peters and Durner, 2008). For HYDRUS-1D (Figure 5.2, right column) simulations, a layered subsurface is defined in which the Mualem-van Genuchten parameters $\mathbf{m}^{MvG} = [\theta_{ri}, \alpha_i, n_i, K_{si}]$ are prescribed for each interval i. Additionally, the saturated water contents θ_{si} (total porosity) were fixed along the entire profile based on laboratory measurements.

5.1.4 Conversion of soil water content into interval velocities and travel times

Combining numerical simulations of hydrological processes with interval velocity and travel time analysis of GPR data allows a coupled inversion for the hydraulic parameters of a layered soil (Figure 5.2, right column). In order to achieve this, a discrete set of observation nodes P was selected from the hydrological model output to obtain the water content distribution with depth for predefined observation days d. Subsequently, these water content profiles [cm^3/cm^3] were converted into dielectric permittivities [-] using the CRIM model (Figure 5.2, right column):

$$\sqrt{\boldsymbol{\varepsilon}^{\mathrm{mod}}(i,d)} = \boldsymbol{\theta}^{\mathrm{mod}}(i,d)\sqrt{\varepsilon_w} + (1-\phi)\sqrt{\varepsilon_s} + \left(\phi - \boldsymbol{\theta}^{\mathrm{mod}}(i,d)\right)\sqrt{\varepsilon_a} \tag{5.9}$$

with a porosity of $\phi = 0.39$ and the permittivities [-] of air $\varepsilon_a = 1$, the solid mineral $\varepsilon_s = 5$, and the water $\varepsilon_w = 84.9$, which corresponds to a temperature of 8°C representing the average annual temperature at the test site. The electromagnetic interval velocities $\mathbf{v}^{mod}(i,d,\mathbf{m}^{MvG})$ and travel time $\mathbf{t}^{mod}(i,d,\mathbf{m}^{MvG})$ are then calculated by:

$$\mathbf{v}^{\mathrm{mod}}\left(i,d,\mathbf{m}^{MvG}\right) = \frac{1}{P_i}\sum_{p_i=1}^{P_i}\frac{v_0}{\sqrt{\boldsymbol{\varepsilon}_{p_i}^{\mathrm{mod}}\left(i,d,\mathbf{m}^{MvG}\right)}}, \tag{5.10}$$

$$\mathbf{t}^{\mathrm{mod}}\left(i,d,\mathbf{m}^{MvG}\right) = \mathbf{h}^{obs}(i,d)\mathbf{v}^{\mathrm{mod}}\left(i,d,\mathbf{m}^{MvG}\right), \tag{5.11}$$

where $v_0 = 0.2998$ m/ns is the electromagnetic wave velocity in air, $\mathbf{h}^{obs}(i,d)$ is the fixed observed layer thickness, $\boldsymbol{\varepsilon}_{pi}^{mod}(i,d,\mathbf{m}^{MvG})$ is the permittivity at node $p_i = 1, ..., P_i$ and P_i is the total number of observation points (Figure 5.2, right column).

5.1.5 Coupled inversion for hydraulic properties

Using the parameters $\mathbf{m}^{MvG}$, we are now able to calculate GPR interval velocities and travel times (Figure 5.2, right column). To evaluate the model fit, we introduced the misfit between the measured and modeled interval velocities and travel times using the objective function (Figure 5.2, middle column):

$$C\left(\mathbf{m}^{MvG}\right) = C_v\left(\mathbf{m}^{MvG}\right) + C_t\left(\mathbf{m}^{MvG}\right), \tag{5.12}$$

$$C_v\left(\mathbf{m}^{MvG}\right)=\frac{1}{D}\sum_{d=1}^{D}\left(\frac{\left|\mathbf{v}^{obs}\left(i,d\right)-\mathbf{v}^{\mathrm{mod}}\left(i,d,\mathbf{m}^{MvG}\right)\right|}{\boldsymbol{\sigma}_v\left(i\right)}\right), \tag{5.13}$$

$$C_t\left(\mathbf{m}^{MvG}\right)=\frac{1}{D}\sum_{d=1}^{D}\left(\frac{\left|\mathbf{t}^{\mathrm{mod}}\left(i,d\right)-\mathbf{t}^{\mathrm{mod}}\left(i,d,\mathbf{m}^{MvG}\right)\right|}{\boldsymbol{\sigma}_t\left(i\right)}\right). \tag{5.14}$$

Here, the misfit in the interval velocities and travel times was normalized with their average deviation from the mean interval velocity $\sigma_v(i)$ and travel times $\sigma_t(i)$ by:

$$\boldsymbol{\sigma}_v\left(i\right)=\frac{1}{D}\sum_{d=1}^{D}\left|\mathbf{v}^{obs}\left(i,d\right)-\frac{1}{D}\sum_{d=1}^{D}\mathbf{v}^{obs}\left(i,d\right)\right|, \tag{5.15}$$

$$\boldsymbol{\sigma}_t\left(i\right)=\frac{1}{D}\sum_{d=1}^{D}\left|t^{obs}\left(i,d\right)-\frac{1}{D}\sum_{d=1}^{D}t^{obs}\left(i,d\right)\right|. \tag{5.16}$$

To find the model parameters $\mathbf{m}^{MvG}$ that provide the best fit in the multi-dimensional solution space, an efficient minimization algorithm must be used (Figure 5.2, middle column). Here, we used the shuffled complex evolution (SCE-UA) method described by Duan et al. (1992), which is a global optimization routine that combines deterministic and probabilistic approaches to evolve a population of parameter combinations towards the global minimum of the objective function. The coupled inversion was stopped when 10 successive evolution loops did not improve the objective function by more than 0.01% (Figure 5.2, middle and right column). The corresponding confidence intervals of the inverted model parameters were determined by a first-order approximation as suggested by Kool and Parker (1988).

Note that the coupled hydrogeophysical inversion used interval velocities and travel times for the data fitting and the uncertainty in their calculation was not explicitly taken into account during the inversion process. Moreover, each soil layer has four unknown parameters, and this increases to six parameters when film flow is considered. Obviously, the computational costs of the inversion process increase significantly when the number of soil layers is increased. In addition, a larger number of soil layers poses larger demands on the information content of the observed data to reliably estimate soil hydraulic parameters. Therefore, we restrict the coupled inversion to two- and three-layered soils in the following application to synthetic and measured data.

5.2 Application to synthetic data

To investigate the feasibility of hydraulic parameter estimation by the coupled inversion approach, synthetic time-lapse surface GPR data were modeled for a layered soil. Assuming that the effects of vertical stratigraphic variations in the soil water content and hydraulic parameters for the intervals i = 1 - 4 are negligible, the soil can be described by a two-layered subsurface where a top soil (i = 0, Figure 5.1) is overlying a homogeneous

Table 5.1 Hydraulic parameter and objective functions *C* for the two-layer inversion of modeled time-lapse surface GPR data without (*CAP*) and with film flow (*FILM_CAP*), respectively. The values indicated by ± show the 95% confidence interval based on the first order approximation.

	MvG parameter	$\mathbf{m}^{MvG}$ model	lower boundary	upper boundary	$\mathbf{m}^{MvG}$ *CAP*	$\mathbf{m}^{MvG}$ *FILM_CAP*
Top soil (i = 0)	θ_r [cm^3/cm^3]	0.07	0.04	0.11	0.06	0.07
					± 0.001	± 0.0001
	α [1/cm]	0.04	0.02	0.06	0.03	0.04
					± 0.001	± 0.0003
	n [-]	2	1.1	3	2	2
					± 0.03	± 0.004
	K_s [cm/d]	1140	570	1710	1708	1209
					± 66	± 42
	ω [-]	0.06	0	0.1	-	0.06
						± 0.002
	τ [-]	1	0	5	-	1.6
						± 0.009
Underlying soil (i = 1 - 4)	θ_r [cm^3/cm^3]	0.06	0.03	0.87	0.06	0.06
					± 0.002	± 0.0003
	α [1/cm]	0.04	0.02	0.06	0.03	0.04
					± 0.001	±0.0003
	n [-]	2	1.1	3	2	2
					± 0.03	± 0.006
	K_s [cm/d]	2600	1300	3900	1730	2626
					± 57	± 34
Objective function *C* (Eq. 5.12):					0.13	0.002

subsoil (i = 1 - 4). For each interval, four hydraulic parameters $\mathbf{m}^{MvG} = [\theta_{ri}, \alpha_i, n_i, K_{si}]$ were defined to simulate water movement through the subsoil (see Table 5.1).

In addition, by introducing a film flow in the uppermost interval i = 0 with ω = 0.06 and τ = 1.0 in equations (5.7) and (5.8), we explicitly accounted for the contributions of capillary and film flow to the water movement in coarse soils during dry conditions. Here, the part of the hydraulic conductivity that is primarily affected by film flow lies in the pressure head range between about $-10^{2.5}$ and -10^4 cm (Peters and Durner, 2010).

To test the inversion algorithm and to show how parameter estimation is affected by capillary and film flow, we used two different models where we neglect (*CAP*) and account for film flow (*FILM_CAP*). The parameter range used in the global optimization is given in Table 5.1, whereas the saturated water content θ_{si} and the tortuosity factor λ_i were fixed to measured and literature values, respectively. Since more information is contained in the data for the subsoil layer due to reflections from four interfaces as compared to the top soil layer where only the ground wave is used, we reduced the weighting for the lower four reflections by a factor of four such that the information contained in the uppermost layer

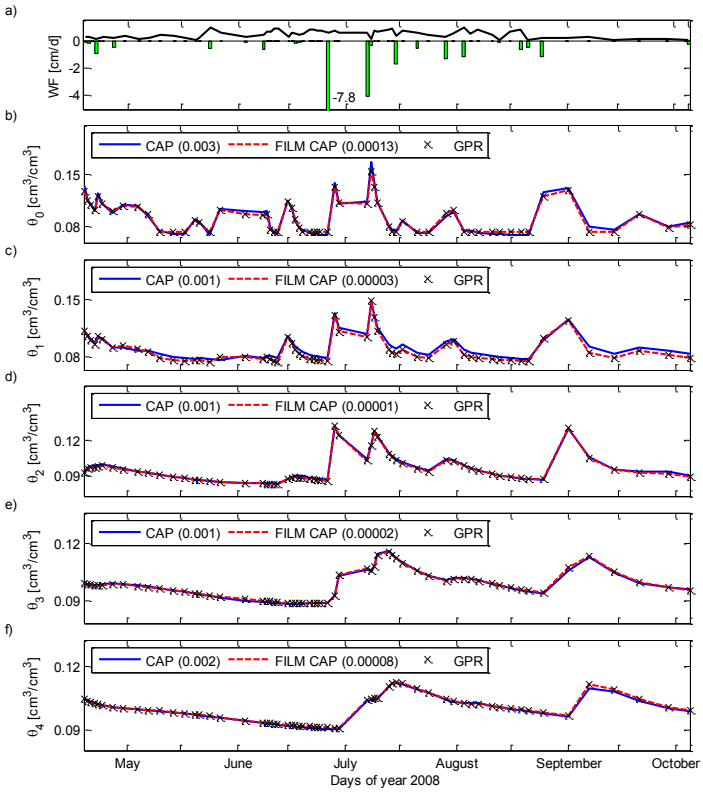

Figure 5.3 a) Input evapotranspiration (black) and precipitation (green); b-f) Average water content profiles and RMSE (brackets) obtained from the modeled time-lapse GPR data with simulated capillary and film flow (black). Blue lines show the results of two-layer inversion *CAP*, red lines indicate the results of *FILM_CAP*. In contrast to *CAP*, in each interval the water content profiles obtained from *FILM_CAP* are overlying with the modeled data. Note that different scales for the axis of the ordinate are used.

(i = 0) and the remaining layers (i = 1 - 4) are equally weighted when determining the hydraulic parameters of the upper layer and the lower halfspace.

Table 5.1 shows the inversion results for *CAP* and *FILM_CAP* and the corresponding objective function values C. Figure 5.3 shows the evapotranspiration (black, a) and precipitation (green, a) obtained from the weather data, as well as the simulated average

Table 5.2 RMSE of the average water content θ_i, the pressure-saturation functions $\theta(h)_i$ and hydraulic conductivity functions $K(h)_i$ for *CAP* and *FILM_CAP*, respectively.

		CAP			*FILM_CAP*		
Interval i	Depth [m]	$\theta_{i,RMSE}$ [cm^3 /cm^3]	$\theta(h)_{i,RMSE}$ [cm^3/cm^3]	$K(h)_{i,RMSE}$ [cm/d]	$\theta_{i,RMSE}$ [cm^3/cm^3]	$\theta(h)_{i,RMSE}$ [cm^3/cm^3]	$K(h)_{i,RMSE}$ [cm/d]
0	0.25	0.003	0.0032	411	0.00013	0.00015	44
1	0.50	0.001			0.00003		
2	1.32	0.001	0.0042	552	0.00001	0.0004	17
3	2.11	0.001			0.00002		
4	2.93	0.002			0.00008		

water content profiles (b-f) and the RMSE (in brackets) for the modeled time-lapse GPR data (black) and the inversion results for *CAP* (blue) and *FILM_CAP* (red). Note that the calculated interval velocities (equation 5.10) are converted into average water content θ_i along the profile using CRIM's relationship (equation 5.9). Although *CAP* returns an reasonable fit to the modeled GPR data, the inversion seems to compensate for the missing film flow parameters ω and τ by overestimating the wetter and underestimating the dryer events especially within the top layer. As a consequence, the inversion using the *CAP* approach leads to inaccurate hydraulic properties $\mathbf{m}^{MvG}$ (Table 5.1). In contrast, the predicted water content obtained with the *FILM_CAP* scenario perfectly matched the synthetic data as indicated by the low RMSE and the inverted hydraulic properties were close to the prescribed hydraulic properties (Table 5.2).

Figure 5.4 compares the prescribed and inverted pressure-saturation $\theta(h)$ and relative hydraulic conductivity function $K_r(h)$ for the top soil layer and the subsoil. The linear addition of the capillary $K_r^{cap}(h)$ and film flow $K_r^{film}(h)$ for the modeled data (black) and the inversion results *CAP* (blue) and *FILM_CAP* (red) are also illustrated. In the case of $\theta(h)$, *CAP* returns a different pressure-saturation function for the top layer and the underlying subsoil due to inaccurate values for θ_{ri}, α_i and n_i, whereas there is a perfect match between the prescribed and inverted pressure-saturation function for *FILM_CAP*. Comparing the inverted hydraulic conductivity function $K_r(h)$ of *CAP* (blue) with the prescribed $K_r^{cap}(h)$ of the modeled data (dashed-dotted black), it is clear that higher values for the hydraulic conductivities were obtained for *CAP* for both soil layers. The hydraulic conductivity function $K_r^{cap}(h)$ for the top layer obtained from *FILM_CAP* (dashed red) as well as $K_r(h)$ for the subsoil (d, dashed red) matched perfectly with the prescribed hydraulic conductivity (dashed-dotted black and solid black). Moreover, the inversion results of *FILM_CAP* for $K_r^{film}(h)$ and $K_r(h)$ (dotted and solid red) are in relatively good agreement with the prescribed function (dashed and solid black) but clearly show the effect of small inaccuracies in the inverted parameters in $i = 0$. Since film flow primarily affects the hydraulic conductivity for small pressure heads (Tuller and Or, 2005; Vanderborght et al.,

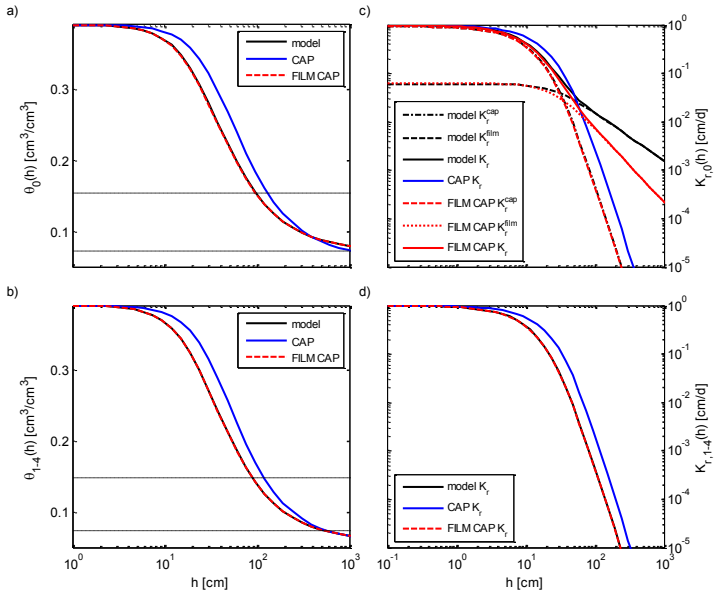

Figure 5.4 Pressure-saturation $\theta(h)$ (a, b) and relative hydraulic conductivity $K_r(h)$ functions (c, d) based on Mualem-van Genuchten parameterization for the modeled data (black) and, *CAP* (blue) and *FILM_CAP* (red), for the ground wave layer (a, c) and the underlying halfspace (b, d), respectively; (a, c) dashed black lines indicate the range in the water content of the corresponding intervals; (c, d) dashed and dotted lines indicate the relative unsaturated hydraulic conductivity due to capillary $K_r^{cap}(h)$ and film flow $K_r^{film}(h)$, whereas solid lines indicate the relative hydraulic conductivity $K_r(h)$ described as the linear superposition of the contributions of capillary and film flow. Note that, except $K_r(h)$ in (c), the calculated retention curves for the modeled data and the inversion results *FILM_CAP* are overlying.

2010), the reason for the inaccuracies in the inversions results might be related to the simulated range of pressure heads that does not reach the low values required for an appropriate parameterization of ω, τ, and K_s.

5.3 Application to field data

To examine the potential of the coupled inversion approach to a field data set, we used the data from Steelman et al. (2012) and focused on the period of unfrozen soil between 1st of April and 1st of November 2008. The overall simulation period in HYDRUS-1D was 214 days where the first 30 days were used as a spin-up to equilibrate the simulated soil water content profile with the atmospheric forcing.

Table 5.3 Uncalibrated Mualem-van Genuchten model calculated from Brooks-Corey laboratory data (Steelman et al., 2012).

Interval	Depth	θ_r	θ_s	α	n	K_s	λ
i	[m]	[cm^3/cm^3]	[cm^3/cm^3]	[1/cm]	[-]	[cm/d]	[-]
0	0.25	0.07	0.39	0.04	2	1140	0.5
1	0.50	0.06	0.39	0.04	2	2600	0.5
2	1.32	0.06	0.39	0.04	2	2600	0.5
3	2.11	0.06	0.39	0.04	2	2600	0.5
4	2.93	0.06	0.39	0.04	2	2600	0.5

Seasonally persistent reflection events allowed to calculate the interval velocities and travel times of four well-defined stratigraphic interfaces located in the upper 3 m of the vadose zone (Steelman et al., 2012), which correspond to the measured GPR intervals i = 1 – 4 (Figure 5.1 and Table 5.3). The inversion of the measured GPR data was carried out for a two-layered subsurface without (*CAP_L2*) and with film flow (*FILM_CAP_L2*), where interval i = 0 represents the direct ground wave. We also considered a three-layered subsurface (*FILM_CAP_L3*), where the interval i = 1 represents a transition soil layer between the top soil and subsoil.

An uncalibrated model of the MvG parameters was estimated from the Brooks-Corey relationships given by Steelman et al. (2012) to characterize their laboratory data. The MvG parameters, which were not adjusted (i.e., calibrated, in the hydrological modeling sense) to improve model fit to the GPR results, were used to define the parameter range for the global optimization as listed in Table 5.3.

For this case, the uncalibrated model described a two-layered subsurface with an organic-rich plough zone with a thickness of 0.25 m containing the soil roots on top of homogeneous sand extending to a depth of 10 m. A single porosity value of 0.39 was used for the saturated water content θ_{si} along the entire vertical profile, whereas the parameter ranges for θ_{ri}, α_i, n_i and K_{si} have been selected widely to avoid excluding plausible parameter values. To obtain an equal weighting of the data in the objective function during the inversion process, we reduced the weighting for the lower four reflections of the two-layer inversions by a factor of four and for the lower three reflections of the three-layer inversions by a factor of three, respectively.

Table 5.4 shows the optimized hydraulic parameters and the minimum objective function C for all considered scenarios. Here, *CAP_L2* and *FILM_CAP_L2* only indicate small differences in the hydraulic properties and the objective function. With the exception of saturated hydraulic conductivity K_s, which exhibited a larger uncertainty based on the Kool and Parker (1988) approximation, these inversions return comparable hydraulic properties for the subsurface. In the case of *FILM_CAP_L3*, the inverted hydraulic parameters θ_r and K_s differ strongly from *CAP_L2* and *FILM_CAP_L2* due to the additional transition zone

Table 5.4 Hydraulic parameter and objective function *C* for the two-layer inversion without film-flow (*CAP_L2*) and the two- (*FILM_CAP_L2*) and three-layer inversion (*FILM_CAP_L3*) with film flow, respectively. The values indicated by ± show the 95% confidence interval based on the first order approximation.

	MvG parameter	$\mathbf{m}^{MvG}$ uncalibrated	lower boundary	upper boundary	$\mathbf{m}^{MvG}$ *CAP_L2*	$\mathbf{m}^{MvG}$ *FILM_CAP_L2*	$\mathbf{m}^{MvG}$ *FILM_CAP_L3*
Top soil (i = 0)	θ_r	0.07	0.010	0.14	0.040	0.049	0.012
	[cm^3/cm^3]				± 0.012	± 0.010	± 0.003
	α [1/cm]	0.04	0.006	0.08	0.059	0.068	0.071
					± 0.019	± 0.031	± 0.014
	n [-]	2	1.1	3	1.5	1.5	1.3
					± 0.1	± 0.1	± 0.02
	K_s [cm/d]	1140	171	11404	2548	2685	6090
					± 1591	± 443	± 1099
	ω [-]	0.06	0	0.1	-	0.07	0.07
						± 0.02	± 0.01
	τ [-]	1	0	5	-	1.5	2.1
						± 0.5	± 0.6
Transition zone (i = 1)	θ_r	0.06	0.009	0.12	-	-	0.079
	[cm^3cm^3]						± 0.005
	α [1/cm]	0.04	0.006	0.08	-	-	0.011
							± 0.003
	n [-]	2	1.1	3	-	-	2.7
							± 0.4
	K_s [cm/d]	2600	390	26006	-	-	6280
							± 1964
Underlying soil (i = 2 -4)	θ_r	0.06	0.009	0.12	0.054	0.056	0.039
	[cm^3/cm^3]				± 0.005$^+$	± 0.003$^+$	± 0.009
	α [1/cm]	0.04	0.006	0.08	0.021	0.014	0.011
					± 0.005$^+$	± 0.003$^+$	± 0.003
	n [-]	2	1.1	3	2.6	2.8	2.1
					± 0.4$^+$	± 0.3$^+$	± 0.2
	K_s [cm/d]	2600	390	26006	7979	6446	8975
					± 3868$^+$	± 2284$^+$	± 1748
Objective function *C* (Eq. 5.12):					0.79	0.81	0.73

$^+$for the two-layer inversion the transition zone and the underlying soil are combined to a halfspace

i = 1, which also leads to a further decrease in the overall misfit to the measured data (Table 5.4).

Figure 5.5 shows the average water content profiles obtained from the time-lapse GPR data (black crosses), the uncalibrated model (black) and *CAP_L2* (blue), *FILM_CAP_L2* (red) and *FILM_CAP_L3* (green). Figure 5.6 shows the calculated interval velocities and travel times and the corresponding RMSE for each interval is presented in Table 5.5. Note that the

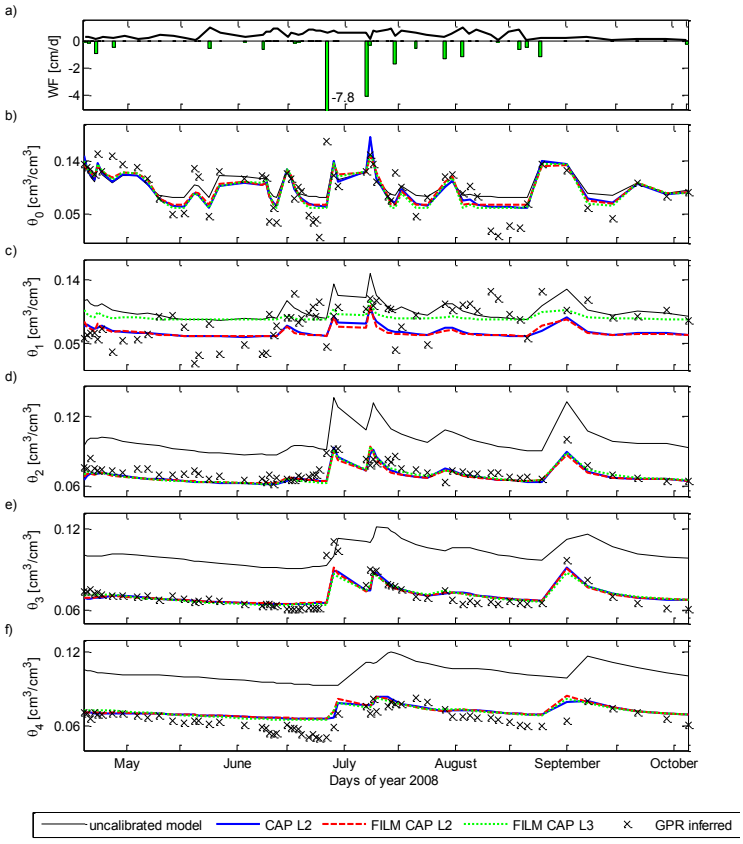

Figure 5.5 Measured evapotranspiration (black) and precipitation (green); b-f) Water content profiles obtained from the time-lapse GPR data (black crosses), the uncalibrated model (black) and the inversion results for *CAP_L2* (blue), *FILM_CAP_L2* (red) and *FILM_CAP_L3* (green), respectively. Except interval i = 1, the results of *CAP_L2*, *FILM_CAP_L2* and *FILM_CAP_L3* are overlying and in good agreement with the water content obtained from the GPR measurements. Especially for the intervals $i = 2 - 4$ the inversion result show a significant improved data fit. Note that different scales for the axis of the ordinate are used.

interval velocities and travel times in Figure 5.6 are calculated based on the average water content; hence they show the same characteristic in the data fitting and the RMSE.

Since the measurement period was characterized by numerous large precipitation events, greater water content variability near the surface with numerous drainage pulses propagating through the soil profile (Steelman et al., 2012). While wetter periods in the

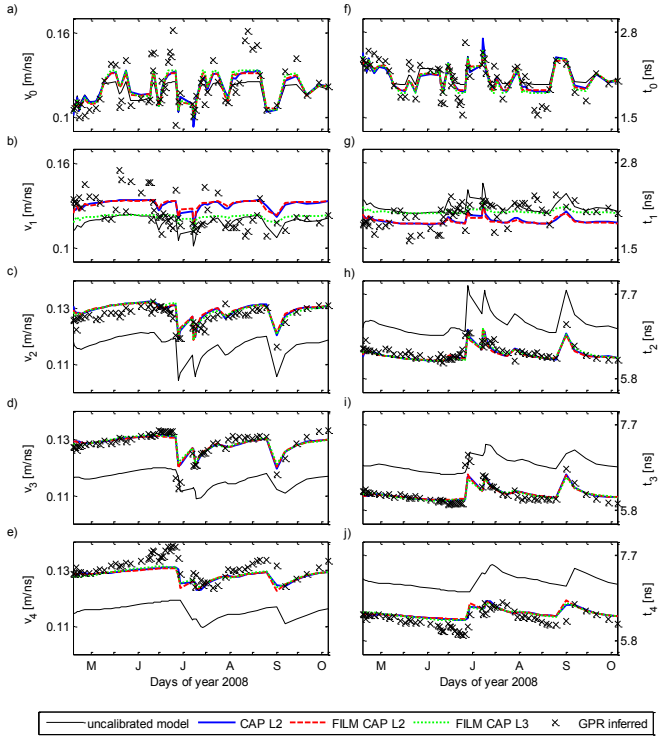

Figure 5.6 Observed GPR interval velocities (black crosses, a-e) and travel times (g-j) and calculated interval velocities and travel times for the uncalibrated model (solid black line), *CAP_L2* (blue), *FILM_CAP_L2* (red) and *FILM_CAP_L3* (green), respectively. Note that different scales for the axis of the ordinate are used.

uppermost subsurface were well-described by the inversion results, measurements from dryer periods were not described as well. Here, *FILM_CAP_L2* and *FILM_CAP_L3* show a slightly better fit in the intervals $i = 0 – 1$ (Figure 5.5) and the film flow parameter ω and τ obtained from *FILM_CAP_L2* and *FILM_CAP_L3* are in very good agreement.

Although the dynamic water content changes obtained from the inversion results are in good agreement, particularly for the intervals $i = 2 – 4$, the differences between the two- and three-layer inversion with film flow are negligible. The additional film flow parameter in *FILM_CAP_L2* did not improve the inversion results and the three-layered model in

Table 5.5 RMSE of the calculated water content θ_i, the interval velocity v_i and travel time t_i based on *CAP_L2*, *FILM_CAP_L2* and *FILM_CAP_L3*, respectively.

Interval i	$\theta_{i,RMSE}$ [cm^3/cm^3]	$v_{i,RMSE}$ [m/ns]	$t_{i,RMSE}$ [ns]
uncalibrated model			
0	0.032	0.013	0.19
1	0.031	0.013	0.20
2	0.029	0.011	0.65
3	0.029	0.013	0.67
4	0.033	0.016	0.83
CAP_L2			
0	0.011	0.011	0.17
1	0.007	0.011	0.19
2	0.009	0.003	0.13
3	0.006	0.003	0.15
4	0.011	0.004	0.16
FILM_CAP_L2			
0	0.011	0.011	0.17
1	0.006	0.012	0.19
2	0.008	0.003	0.14
3	0.003	0.003	0.14
4	0.014	0.004	0.17
FILM_CAP_L3			
0	0.018	0.011	0.17
1	0.013	0.012	0.17
2	0.013	0.003	0.14
3	0.011	0.003	0.15
4	0.019	0.004	0.16

FILM_CAP_L3 only slightly improved the inversion result (see objective function in Table 5.4). This behavior is also indicated in Figure 5.7, which shows a weak positive correlation between the water content calculated from the measured GPR data using the CRIM model (dashed black) and the predicted water content from the hydraulic parameters determined from the uncalibrated model (black), *CAP_L2* (blue), *FILM_CAP_L2* (red) and *FILM_CAP_L3* (green) for the intervals $i = 0$ and $i = 2 - 4$, respectively. Within the top soil layer (a) and the subsoil (b), *CAP_L2*, *FILM_CAP_L2* and *FILM_CAP_L3* return reliable values for θ_0 and $\theta_{2\text{-}4}$ whereas the uncalibrated model (solid black) clearly overestimate the water content inferred from the measured GPR data (dashed black).

Figure 5.8 shows the effective saturations $S_e(h)$ (a-c) as a function of the pressure head (Peters and Durner, 2008):

$$S_e(h) = \left(1 + |\alpha h|^n\right)^{\frac{1}{n}-1}, \tag{5.17}$$

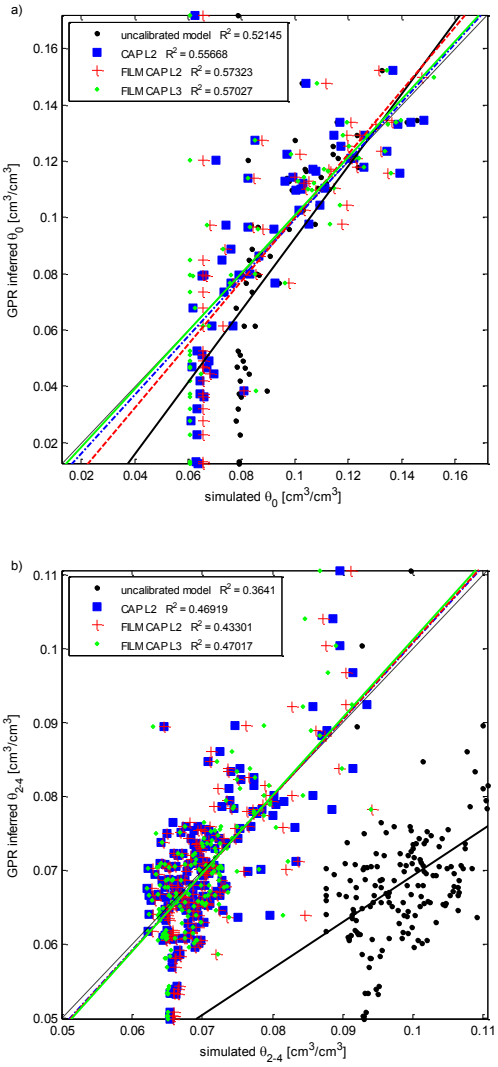

Figure 5.7 Correlation between the water content inferred from GPR measurements (dashed black) and the water content obtained from the uncalibrated model (black), and from *CAP_L2* (blue), *FILM_CAP_L2* (red) and *FILM_CAP_L3* (green), for the intervals $i = 0$ (a) and $i = 2 - 4$ (b), respectively.

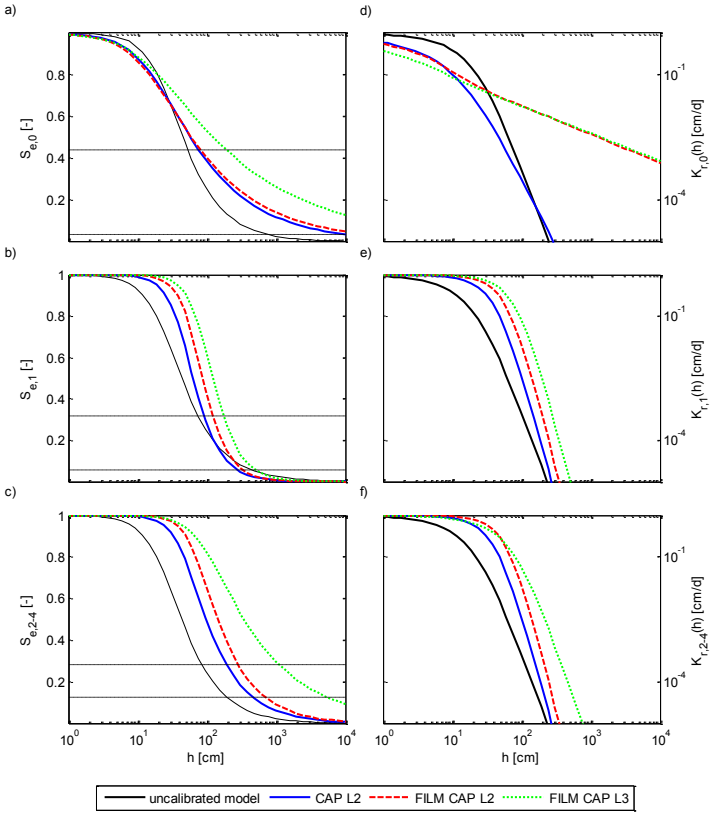

Figure 5.8 Effective saturation $S_e(h)$ (a-c) and relative hydraulic conductivity $K_r(h)$ (d-e) functions based on Mualem-van Genuchten parameterization for the uncalibrated model (black) and the inversion results for *CAP_L2* (blue), *FILM_CAP_L2* (red) and *FILM_CAP_L3* (green), respectively. (a, d) show the retention curves of the top soil (i = 0), (b, e) of the transitions zone (i = 1) and (c, f) of the underlying soil (i = 2 - 4). Dashed horizontal black lines (a-c) indicate the range in the effective saturation of the corresponding intervals.

as well as the relative hydraulic conductivity $K_r(h)$ functions (d-e) for the uncalibrated model (black) and the inversion results for *CAP_L2* (blue), *FILM_CAP_L2* (red) and *FILM_CAP_L3* (green), respectively. Compared to the predictions based on hydraulic parameters derived from the uncalibrated model, the inversion results return higher values for the air entry pressure α and lower values for the pore size distribution n. This results in

flatter curves for $S_e(h)$ and $K_r(h)$ for the top soil layer. In contrast, the inversion results for *CAP_L2*, *FILM_CAP_L2* and *FILM_CAP_L3* return lower values for α and higher values for n for the intervals $i = 1 - 4$, which results in steeper retention curves for the effective saturation and hydraulic conductivity functions.

5.4 Conclusions

A novel coupled inversion scheme that combines conventional ray-based analysis of time-lapse surface GPR data with a hydrological forward model is presented and applied to synthetic and measured GPR data over a horizontally layered subsurface. To allow an appropriate description of the water flow under wet and dry conditions, we explicitly account for capillary and film flow in the uppermost subsurface layer.

In case of synthetic data with film flow, the coupled inversion approach that did not include film flow was able to reproduce modeled data despite a wrong model formulation and returned different hydraulic parameters that partly compensated the error introduced by neglecting film flow. The modeled data were correctly inverted using the coupled inversion approach that included the film flow. Here, the inversion results clearly show the importance of an appropriate model conceptualization when using coupled inversion.

In the case of measured time-lapse GPR data, we used a two- and three-layered subsurface. The inversion was able to reduce the RMSE between measured and predicted soil water content as compared to an uncalibrated model relying on laboratory derived hydraulic parameters. Here, especially the RMSE of the subsoil could be improved and the dynamic water content changes could be fitted very well. At this point the novel coupled inversion clearly showed the potential to estimate the hydraulic properties of the subsurface.

However, neither the consideration of film flow nor the consideration of a transition zone between the topsoil and subsoil improved the inversion results as compared to a two-layer subsurface.

To assure reliable parameter estimates from model inversion, the hydrological model should describe the dominating processes present in the measured data in detail. In the case of an inaccurate hydrological model, the coupled inversion will optimize the model parameters to achieve the best possible data fit. As a consequence, the inversion may return inaccurate hydraulic properties, as was observed in the synthetic case study. Moreover, the inversion results are also sensitive to the incorrect specification of the atmospheric forcing, since daily precipitation measurements and daily estimates of the potential evapotranspiration serve as input data for hydrological modeling. Here, meteorological data were obtained from a weather station with a distance of 7 km to the test site and the use of measurements directly at the test site will probably improve the description of evapotranspiration. In addition, simplified ground cover conditions such as a constant and densely distributed plant canopy during the simulation period as well as an over-simplified parameterization of the root water uptake model might be a reason for the misfit in the top

soil layer. Moreover, as already described by Steelman et al. (2012), HYDRUS-1D does not consider all processes that affect soil water content in the dry range. Here, Steelman et al. (2012) suggested the implementation of a capillary and film flow model to better describe the field data, since the liquid water begins to move upwards from the deeper layers by capillary and film flow when the soil becomes very dry in the upper few centimeters due to soil heating. When the water reaches the drying front, it is converted to water vapor and evaporates to the atmosphere. However, we were not able to significantly improve the coupled inversion results for the top soil layer with a simple method to account for capillary and film flow following Peters and Durner (2008). Therefore, it may be necessary to use numerical representations of coupled heat and vapor transport to accurately represent water content in the dry range (Saito et al., 2006; Steenpass et al., 2010). Unfortunately, the numerical effort associated with such models is large, and therefore its use in coupled inversion of long time series is problematic.

Chapter 6

Conclusions and Outlook

The objectives of this PhD work were to investigate the feasibility of surface GPR for a the quantitative estimation of the subsurface permittivity and conductivity as well as the hydraulic property estimation at the field scale. Therefore, two independent inversion approaches, the surface GPR full-waveform inversion (Chapters 3 and 4) and the coupled hydrogeophysical inversion of surface GPR data (Chapter 5), were developed which improve the characterization and the understanding of the highly dynamic process in the shallow subsurface.

6.1 Surface GPR full-waveform inversion

The proposed full-waveform inversion (FWI) scheme for surface GPR is based on a combined global and local search algorithm and uses a 3D forward model for a horizontally layered model that returns the exact electromagnetic field of the subsurface including far-, intermediate- and near-field contributions. The inversion returns the subsurface medium parameters (permittivity and conductivity), which mainly influence the velocity and amplitudes, respectively. Conventional ray-based techniques usually return good starting values for the relative permittivity. However, estimates of the conductivity values contain relatively large errors for surface GPR.

Since the wavelet amplitudes and medium properties are coupled, an important aspect for a successful inversion is the estimation of the unknown source wavelet, which is addressed by an iterative sequential phase and amplitude optimization by updating the model parameters and the source wavelet. To further address the coupling between the permittivity and conductivity, which is not explicitly taken into account during the sequential optimization process, the optimized parameters serve as input for a simultaneous parameter optimization while keeping the wavelet fixed.

Focusing on the analysis of reflected wave and applying this approach to two single-layered synthetic models clearly shows the benefits compared to a more straightforward simultaneous parameter optimization with a fixed wavelet and a combined sequential and simultaneous model optimization without directly inverting the wavelet parameters. Simulating a worst case scenario for the starting model in which the initial model parameters are far away from the true model parameters, only the combined sequential and simultaneous model and wavelet optimization is able to reconstruct the true model parameters. Due to the explicit source wavelet optimization, this approach has a better

convergence and is not trapped in a local minimum. Throughout the inversion process, the effective source wavelet and the starting model of the subsurface properties were significantly improved resulting in a reliable inversion result. Here, the proposed optimization works well even when the starting model and therefore the effective wavelet differ strongly from the true parameters. Moreover, complex wave phenomena such as offset dependent amplitudes and dispersion due to a low velocity waveguide could be well reconstructed.
Our inversion was applied to experimental data measured over a single-layer low-velocity waveguide, consisting of a thin high-permittivity sandy silt layer overlying a low permittivity gravel, that contained complicated interfering multiples. Here, the full-waveform inversion reduced the misfit of the initial start model derived from conventional dispersion inversion significantly and obtained quantitative values for permittivity and conductivity. To limit the influence of noise on the inversion and prevent that the inversion gets stuck in a local minimum, we introduced an offset-dependent signal-to-noise (SNR) threshold, calculated from the mean spectral noise amplitudes at high frequencies. Amplitudes below this threshold were excluded from the inversion, which resulted in a robust and reliable inversion.

In the case of lossy soils, where sometimes only the direct ground wave can be measured, especially the subsurface conductivity contains important information that cannot be reliably obtained by using conventional ray-based methods. Therefore, we extended the inversion approach to analyze the direct ground wave and verified the surface GPR FWI for fine texture soils.
Measurements were performed over a silty loam at the Selhausen test site in North Rhine-Westphalia, Germany, with significant variability in the soil texture. Since the test site is weakly inclined (< 4°), colluvial sediments that eroded from the upper part of the test site now can be found in the lower part of the test site. The ground water depth shows seasonal fluctuations between 3 m and 5 m below the surface. A distinct gradient in soil texture is present with a considerably higher stone content of up to 60% at the upper and 10 % at the lower part of the field. Moreover, soil samples of the top 30 cm showed that the silt (25 - 63%) and clay (7 - 14%) content of the top soil increases from the upper to the lower part of the test site whereas the skeleton content decreases (54 - 9%) and the sand content remains constant (14%).
The ground wave present in the surface GPR wide-angle reflection-refraction (WARR) data was inverted using the full-waveform inversion and the obtained permittivities and conductivities were compared with the results of Theta probe (effective permittivity), ERT and EMI (conductivity) measurements, respectively. The permittivity values obtained from Theta probe (11.36 – 17.41) measurements and the GPR FWI (8.11 – 18.01) as well as the conductivity values obtained from ERT (4.26 – 19.10 mS/m), EMI (5.24 – 19.34 mS/m) inversion and GPR FWI (5.53 – 28.17 mS/m) are consistent with increasing clay and silt content and a decreasing skeleton content.

Although each method has a different sensing depth and frequency range, these methods returned a similar trend in the electric soil properties and therefore indicate the reliability of the surface GPR full-waveform inversion.
The correlations of the obtained conductivities and permittivities with the soil texture indicate a strong linear relationship with correlation coefficients R^2 in the range of 0.80 - 0.98. Here, since the surface GPR FWI returns two independent parameters for the same sensing volume, the full-waveform inversion enabled the parameterization of an orthogonal distance regression for the soil texture and the permittivity and conductivity and therefore enabled an improved characterization of the Selhausen test site.
Moreover, a the three-dimensional correlation between the subsurface permittivities and conductivities and the amplitude and center frequency of the effective source wavelet was observed during the inversion of the WARR data. The correlation coefficients R^2 in the range of 0.44 - 0.94 clearly indicate that the effective wavelet is affected by the subsurface properties. This is consistent with the changing radiation patterns and the electrical antenna length and enables to further investigate the influence of the various subsurface properties on the wavelet characteristics.

6.2 Coupled inversion of time-lapse surface GPR data

Although soil moisture content can be well determined with GPR measurements in sandy soils, it is not straightforward to obtain hydraulic properties from the GPR data where time-lapse measurements are needed. Here, we propose a coupled hydrogeophysical inversion of time-lapse GPR data where measured GPR interval velocities and travel times are combined with a hydrological model of the subsurface. Using the shuffled complex evolution approach (SCE-UA) algorithm, the differences between the measured and modeled GPR velocities and travel times are minimized by varying the hydraulic properties of the hydrological model and converting the obtained simulated water content values to synthetic interval velocities and travel times using a petrophysical relationship. The soil hydraulic properties obtained for the best fitting model are assumed to be representative parameters that describe the measurements best.
Our coupled inversion approach was applied to the data set of Steelman et al. (2012) to examine its performance when applied to real field data. In their study, the authors conducted an extensive 26 month field study covering two contrasting annual cycles of soil conditions typical of mid-latitude climates. Therefore, GPR reflection profiling and CMP soundings were carried out in a daily to weekly interval to characterize vertical soil water dynamics within the vadose zone. Reflection profiles provided high resolution travel time data between four stratigraphic reflection layers while the analysis of the CMP returned precise depth estimates for the reflecting interfaces. The unique data set revealed the highly variable nature of the soil water content in the uppermost 20 - 25 cm on both seasonal and shorter time scales and resolved the downward propagation of major infiltration episodes

associated with seasonal (i.e. spring recharge) and transient (i.e. major rainfalls and intra-winter thaws) events. In addition, the GPR data indicated variability in the nature of these seasonal trends and infiltration events between contrasting annual cycles, such as a dry versus a wet summer.

Due to the presence of dry soil states in the measured data obtained over a sandy soil, we explicitly account for capillary and film flow in the uppermost subsurface layer to allow an appropriate description of the water flow under wet and dry conditions.

In case of synthetic data with film flow, the introduced coupled inversion approach that did not include film flow partly compensated the error introduced by neglecting film flow. Although the approach returns an reasonable fit to the modeled GPR data, the inversion seems to compensate for the missing film flow parameters by overestimating the wetter and underestimating the dryer events especially within the top layer which in turn results in inaccurate hydraulic parameters. In contrast, by accounting for capillary and film flow the modeled data were correctly inverted which clearly shows the importance of an appropriate model conceptualization when using a coupled inversion.

The inversion was able to reduce the RMSE by factor of 2.1 - 3.7 between measured and predicted soil water content as compared to an uncalibrated model relying on laboratory derived hydraulic parameters. Here, especially the RMSE of the underlying halfspace could be improved and the dynamic water content changes could be fitted very well. For the top soil neither accounting for film flow nor the consideration of a transition zone between the topsoil and subsoil returns a significant improvement in the data fit. Here, probably an hydrological model that includes heat and vapor transport will improve the data fit of the soil water content under dry conditions. Nevertheless, the application to synthetic and measured data clearly verifies the capacity of surface GPR to provide reliable information about soil moisture dynamics, and also demonstrates its suitability for the field-scale soil hydraulic parameter estimation.

6.3 Outlook

The novel full-waveform inversion of surface GPR CMP data is a promising tool to obtain quantitative permittivity and conductivity values in complicated media configurations, such as the dispersion of the electromagnetic waves due to the presence of a waveguide layer. Here, the application of conventional used ray-based techniques is limited and may provide inaccurate estimates of the medium properties.

Due to the additional electrical conductivity information, especially for the characterization of fine texture soils the full-waveform inversion can probably reduce the non-uniqueness of increasing permittivity caused by increasing clay or soil water content. Here, probably because of the lack of quantitative conductivity data, the information present within the conductivity at GPR frequencies has not been explored until now.

Moreover, a combination of soil moisture content estimation by converting permittivities and conductivities using Topp's equation and Archie's law might enable an explicit contribution of fine texture soil content that manifests itself by an increased conductivity due to the presence of surface conduction (Annan, 2005).
Since the FWI also provides quantitative values for the center frequency and amplitude for the characterization of the effective source wavelet, further research will show if the wavelet characteristics might also be used for an improved soil characterization. The proposed full-waveform inversion approach can easily be extended for a multi-layer model and the obtained results can be used as a starting model for a 2.5D or 3D surface GPR full-waveform inversion. Furthermore, acquiring and inverting quantitative medium properties on large scales offers a great potential for a wide range of applications.

The hydrogeophysical inversion of synthetic and measured time-lapse surface GPR data clearly shows the potential of the coupled inversion approach to estimate the hydraulic properties of a layered subsurface.
Currently, the proposed coupled hydrogeophysical inversion uses conventional standard ray-based techniques to obtain velocities and travel times from time-lapse surface GPR data containing ground and reflected waves. In this way, only part of the measured data is used to obtain wave propagation information. An extension of the approach using the full-waveform forward modeling as described in Chapters 2 and 3 will result in a more accurate forward modeling of the electromagnetic wave propagation and enables the inversion of the full measured waveforms to obtain reliable quantitative estimates of the permittivity and conductivity where common ray-based techniques are not appropriate such as in the case of waveguide dispersion. Note that the full-waveform inversion does not need a specific adaption for the ground, reflected or waveguide dispersive waves since the forward model includes all waves that can propagate through the subsurface.

Appendix A

Chlorides and moisture assessment in concrete by off-ground GPR full-waveform inversion*

The full-waveform (FWI) methodology is applicable for a wide range of applications. In the case of civil engineering, the assessment of existing concrete structures is a major challenge. Here, especially the reinforcement corrosion is an important issue since structures such as bridges are exposed to corrosion because of salt spread in winter for road de-icing. Ground Penetrating Radar (GPR) presents several abilities for their assessments: GPR (i) is non destructive, (ii) can locate changes of medium conditions (iii) allows keeping the structure open for traffic during its inspection. Therefore, GPR is a suitable non-destructive tool to investigate reinforced concrete bride decks (Sbartai et al., 2006; Hugenschmidt and Mastrangelo, 2006; Klysz and Balayssac, 2007; Derobert et al., 2008).
A previous experimental assessment carried out with GPR measurements over nine concrete specimens with controlled chloride and moisture content (Hugenschmidt and Loser, 2007) demonstrated that amplitudes of reflections are influenced by both the chloride and moisture content. However, it was not possible to discriminate between moisture and chloride effects. Recently, several full-waveform inversions have been developed that enable medium properties quantitative estimation by fitting the entire measured waveform with an accurate forward model (Crocco and Soldovieri, 2003; Lambot et al., 2004c; Ernst et al., 2007b; Meles et al., 2010, Klotzsche et al., 2010).
In this Chapter we describe the processing of the experimental off-ground GPR data and investigate the influence of chlorides and moisture on estimations of the electric conductivity and the relative dielectric permittivity obtained from a full-waveform inversion and discuss the stability of these results.

A.1 Basics of steel corrosion due to the presence of chlorides

During winter salt is used for road de-icing, the chlorides dissolved in the melt water are scattered around the reinforced concrete structure mainly due to vehicle circulation (splash, mist and stagnation). Once the impermeability of the sealing is compromised, the water containing chlorides penetrates into the underlying concrete during wet seasons. During dry seasons water evaporates without mobilizing chlorides that remain in the concrete. This way the alternation of weathering cycles causes the chlorides to gradually migrate through the pores of the concrete by capillarity and diffusion (Conciatori, 2005). Thus one can expect to encounter chloride and water concentration gradients within a concrete structure.

*Adapted from Kalogeropoulos, A., J. van der Kruk, J. Hugenschmidt, S. Busch, and K. Merz, 2011, Chlorides and moisture assessment in concrete by GPR full waveform inversion: Near Surface Geophysics, 9, 277–285.

Reinforced concrete structures and specifically bridge decks contain several layers of steel reinforcing bars (rebars) for bearing resistance. Once chlorides reach the first rebar layer (generally located at 2 to 4 cm depth) the chlorides ions remove the protecting passivation layer on the steel rebar surface and localized corrosion (pitting) is initiated. Pitting corrosion induces localized areas to become anodic while the rest of the bar becomes cathodic, this creates an electric potential that increases the corrosion process. Different studies have shown that the probability of the initiation increases steadily with increasing chloride level. This probability is considered as high when exceeding 0.5 % chloride content (Böhni, 2005). Once initiated, the corrosion process does not stop, and the rebars lose progressively their mechanical resistance until possible structural failure.

A.2 Experimental setup

In order to evaluate the effect of chlorides and moisture on ground penetrating radar signals, experiments were carried out by measuring traces with fixed-height horn antennas over concrete slabs having controlled moisture and chloride content.

A.2.1 Concrete specimens

Nine concrete slabs were produced (Hugenschmidt and Loser, 2007), each with dimensions of 0.90 m, 0.75 m, 0.08 m. Three concrete mixtures with constant volume of paste but different chloride contents were used (Table A.1).

Table A.1 Specimen numeration.

	Moisture		
Chloride	35 %	70%	90%
1.0%	7	8	9
0.4%	4	5	6
0.0%	1	2	3

Chlorides were added to the mixtures by dissolving *NaCl* in the mixing water. All mixtures had comparable fresh concrete properties. The concrete was cast in three moulds per mixture and the bases of the moulds were covered with aluminium sheets. After compaction, the specimens were stored at 20°C and 90% relative humidity for 2 days. Afterwards, one specimen of each mixture was moved to climates of 35%, 70% and 90% relative humidity for 99 days before the radar measurements were carried out. One would expect to obtain higher increasing relative dielectric permittivity ε_r for increasing water content and higher increasing conductivity σ for increasing chloride content.

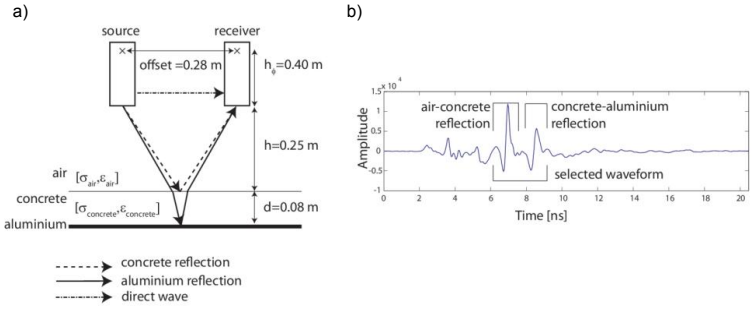

Figure A.1 (a) Measurement setup of off-ground Horn antennas with an offset between source and receiver antenna of 0.28 m. Ray-paths indicate the simplified travel paths of the direct wave, the air-concrete and concrete-aluminum reflection; (b) Trace recorded on concrete specimen showing the direct wave between 2 and 6 ns and two reflections coming from the air-concrete and concrete-aluminium interfaces. Corresponding simplified travel paths are shown in (a).

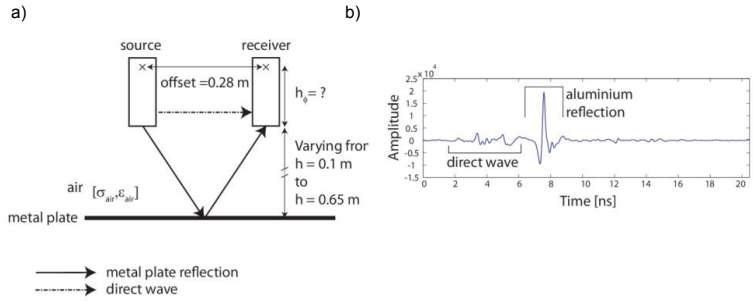

Figure A.2 (a) Antenna calibration setup over an aluminium plate; (b) Calibration trace recorded for time zero positioning and effective wavelet estimation. The direct wave is visible and the high-amplitude reflection from the air-aluminium interface is clearly visible.

A.2.2 GPR measurements

The measurements were performed using two off-ground 1.2 GHz horn antennas with an offset of 0.28 m and positioned at a fixed height (h = 0.25 m) above the concrete specimens (Figure A.1a). A representative trace is shown in Figure A.1b. For calibration purposes, also measurements were performed over a metal plate for different heights (see Figure A.2).

A.3 Forward model

To perform a full-waveform inversion of GPR data, an accurate forward model is necessary that describes the medium properties and the electromagnetic wave propagation from source to concrete specimen and back to the receiver.

A.3.1 Medium properties

The analysis of the normalized frequency spectrum of the concrete-aluminum interface reflection of the recorded data revealed that for increasing chloride contents, the high frequencies had lower amplitudes (Figure A.3). These relatively lower amplitudes for higher frequencies indicate a frequency dependent conductivity assessed by several authors (Robert, 1998; Soutsos et al., 2001; Lambot et al., 2005). To include the frequency-dependent conductivity in the model the following equation was used

$$\sigma\left(f,\sigma_{fc},\Delta\sigma\right)=\sigma_{fc}+\frac{\left(f-f_c\right)}{f_c}\Delta\sigma, \tag{A.1}$$

where f_c is the center frequency of the GPR system (1.2 GHz), σ_{fc} is the reference electric conductivity at the center frequency and $\Delta\sigma$is the frequency dependent part of $\sigma(f,\sigma_{fc},\Delta\sigma)$. The frequency dependence of the relative permittivity was assumed to be negligible (Lambot et al., 2005).

A.3.2 Greens function

The antennas were modeled as point sources that emit an effective wavelet $\hat{W}(f)$ for the medium properties $\mathbf{m} = [\varepsilon_r, \sigma]$. Since the wavelet is unknown we need the calibration setup shown in Figure A.2 and introduce the following Greens function

$$\hat{G}\left(f,\mathbf{m}\right)=\hat{G}^{aa}\left(f,\mathbf{m}\right), \tag{A.2}$$

where $\hat{G}^{aa}$ describes the total reflection of a wave propagating from the source to a metal plate and its back-propagation to the receiver (Figure A.2a). For the concrete measurements, two reflections are measured (see Figure A.1b), and the corresponding Greens function includes the source-reflector and reflector-receiver propagation plus both reflections coming from the concrete specimen interfaces which can be written as

$$\hat{G}\left(f,\mathbf{m}\right)=\hat{G}^{ac}\left(f,\mathbf{m}\right)+\hat{G}^{ca}\left(f,\mathbf{m}\right), \tag{A.3}$$

where $\hat{G}^{ac}$ and $\hat{G}^{ca}$ stand for the propagation of the first reflection on the air-concrete interface and the second reflection of the concrete-aluminum interface, respectively.

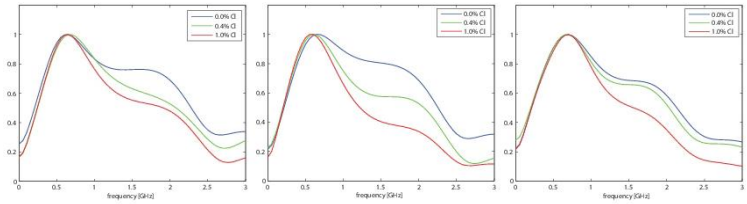

(a) 35% Relative Humidity (b) 70% Relative Humidity (c) 90% Relative Humidity

Figure A.3 Normalized frequency spectrum of measured traces for (a) 35%, (b) 70% and (c) 90% relative humidity and 0% (blue), 0.4% (green) and 1% (red) chloride content. For increasing conductivity, the high frequency amplitudes are reduced more than the low frequencies and clearly show a frequency dependent conductivity for all three relative humidities.

A.4 GPR system characterization

A critical step for full-waveform inversion is a proper characterization of our GPR system (Klotzsche et al., 2010). Our forward model describes the measurements assuming a point source and receiver. In reality, these antennas are horn antennas, where the waves are guided within the antenna and spread spherically while outside them. The calibration procedure described by Lambot et al. (2004c, 2006c) where a monostatic off-ground antenna system was used in combination with a Vector Network Analyzer is not possible since our measurements were carried out using a commercial GPR system. Here, we describe our GPR system by estimating a phase center and an effective wavelet when the system is measuring reflections coming from a metal plate. In this way, we will be able to match the measured waveforms, including any small nuances which may be present.

A.4.1 Phase center estimation

The phase center is the virtual point from which the electromagnetic waves seem to be emitted or received assuming point source and receiver antennas (see also Figure A.1a). To estimate the phase center, a calibration was performed by measuring the reflections coming from a metal plate for heights varying between $0.1 < h < 0.65$ m (Figure A.2a). A time domain filter was used to select the air-aluminum reflection (see Figure A.2). Additionally, we used the Fresnel zone to ascertain that only the reflections from the specimen will be inverted and no side reflections influence the results. The Fresnel zone (Figure A.4) is the diameter of a circle from which the reflections constructively interfere (i.e. the travel path

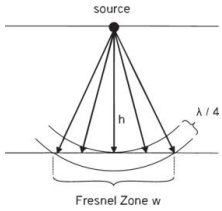

Figure A.4 Fresnel zone calculations are used to consider only the reflected energy coming from the metal plate during phase center estimation.

between vertical incident ray and the ray from the boundary of the Fresnel zone boundary have half-wavelength difference in travel path) and is given by

$$\text{Fresnel zone} = \sqrt{\frac{0.6h}{f\,[\text{GHz}]}}\,, \tag{A.4}$$

where h the height in [m] and f is frequency given in [GHz]. The Fresnel zone can be used to estimate the lowest frequency from which all reflections come still from the surface of the metal plate and not from its sides. Taking the smallest horizontal dimension of the concrete specimen, 0.75 m and a maximum height of h = 0.65 m to calculate the lowest frequency from which the side effects have no influence on the measurements, we get 700 MHz as a lower limit. Note that the phase center is not included in the Fresnel zone calculation since the waves are guided within the antenna.

The amplitudes from the surface reflection of the metal plate decrease with *1/(travel distance)* or *1/(2*height)* due to the geometrical spreading when measured in the far-field. By plotting the inverse values of representative amplitudes within the wavelet as function of the travel distance (or height), we can extrapolate towards zero amplitude using a linear regression approach which indicates the position of the phase center (Lambot et al. 2004c, 2005, 2006c). Here, we used the maximum, minimum-maximum, and energy values of the reflected waveforms which returned a similar value of the phase center, h_ϕ = 0.40 m (Figure A.5).

A.4.2 Effective wavelet estimation

The effective wavelet is determined to describe the effective wavelet that is emitted and received by the antennas. It is extracted for each specimen by spectral division of a calibration measurement and a Greens function (Streich and van der Kruk, 2007b; Ernst et al., 2007a; Klotzsche et al., 2010) by

$$\hat{W}(f) = \frac{\hat{E}_{data}(f,\mathbf{m})\hat{G}^{aa*}(f,\mathbf{m})}{\hat{G}^{aa}(f,\mathbf{m})\hat{G}^{aa*}(f,\mathbf{m}) + 10^{-10}}\,, \tag{A.5}$$

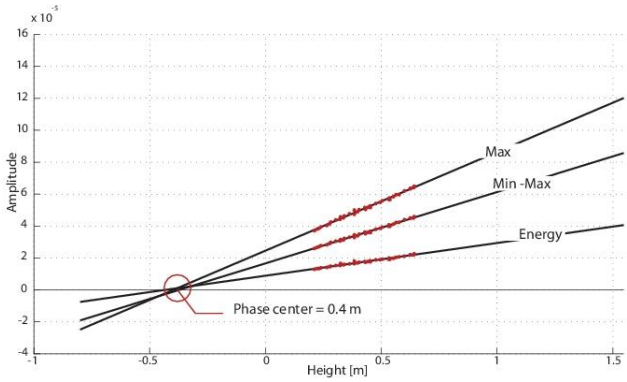

Figure A.5 Linear regression using the inverse values of reflected calibration waveforms values (maximum, minimum-maximum and energy) to estimate the phase center.

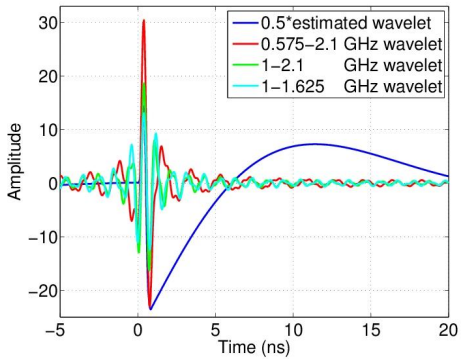

Figure A.6 Estimated wavelet (halved in amplitude) and three frequency-filtered wavelets used in the inversion.

where $\hat{E}_{data}(f,\mathbf{m})$ is the calibration trace with the corresponding height ($h + h_\phi$ = 0.65 m) used for the inversion measurements (see also Figure A.2), and is the calculated Greens function (A.2) describing a total reflection of the incident wave on the metal plate surface assuming a reflection coefficient of -1. The value 10^{-10} is used to avoid division by zero. Figure A.6 shows the estimated wavelet and three frequency-filtered wavelets that are used in the inversion. Both the phase center and the effective wavelet now fully describe the GPR system and do not change when the antennas are placed in front of another specimen.

A.5 Full-waveform inversion methodology

The dataset, measured with a 1.2 GHz antenna center frequency, contains frequencies between 500 MHz and 2.1 GHz (see also Figure A.3) and the data were inverted using three different frequency ranges: 0.575 - 2.1 GHz, 1 - 2.1 GHz, and 1 - 1.625 GHz using the corresponding wavelet shown in Figure A.6. After estimating the phase center and the effective wavelet, synthetic GPR data with configuration parameters according to the measurements are modeled using equations (A.1) and (A.3). In the following, the model parameters **m** describe the wave propagation within the concrete slab are optimized for n frequencies by minimizing the misfit between the measurement and the synthetic data by

$$C(\mathbf{m}) = \sum_{i=1}^{n} \frac{\hat{E}_{data}(f_i, \mathbf{m}) - \hat{G}(f_i, \mathbf{m})\hat{W}(f_i)}{n}. \tag{A.6}$$

For full-waveform inversion the starting model is important. Using a starting model that is far away from the actual global minimum can result a wrong result due to the presence of a local minimum. Especially when the starting model returns traces with a time-shift larger than half the period of the dominant frequency of the signal this can cause failure due to the occurrence of cycle skipping. Having a time shift of less than half the dominant period of FBID is a necessary but not sufficient condition to guarantee success.

To improve the robustness of our inversion strategy against local minima and to assure the convergence towards the global minimum returning the true values of the electric features of the concrete slabs, we use the picked time zero and the maximum and minimum of both air-concrete and concrete-aluminium reflections as starting values in the inversion algorithm. Moreover, we use several starting models in the three consecutive steps of the inversion algorithm to investigate the convergence. For each starting model a local optimization algorithm based on the simplex search algorithm (Lagarias et al., 1998) is initiated and a local minimum is found. The local minimum with the smallest cost function is assumed to be the global minimum.

The first step optimizes the time-zero and the concrete permittivity ($\mathbf{m}_1 = [t_0, \varepsilon_r]$) by minimizing the misfit between the measured air-concrete reflection and $G^{ac}W$. A correction for the time-zero is needed since a metal plate is put on the specimen for the calibration measurements which slightly change the vertical location of the reflection. Here, we do not optimize the frequency-dependent conductivity since the air-concrete reflection mainly depends on the concrete permittivity. Two starting values for the time zero are obtained by taking the picked time zero plus and minus one sample. Two starting values for the permittivity are derived by picking the maximum and minimum of both air-concrete and concrete-aluminium reflections and using the thickness of the concrete slab resulting in four starting models. For all starting models the inversion results are equal clearly indicating that the global minimum is found. The obtained time zero is fixed in the following steps.

The second step optimizes the concrete permittivity and frequency-dependent conductivity $\mathbf{m}_2 = [\varepsilon_r, \sigma_{fc}, \Delta\sigma]$ by minimizing the misfit between the concrete-aluminium reflection and

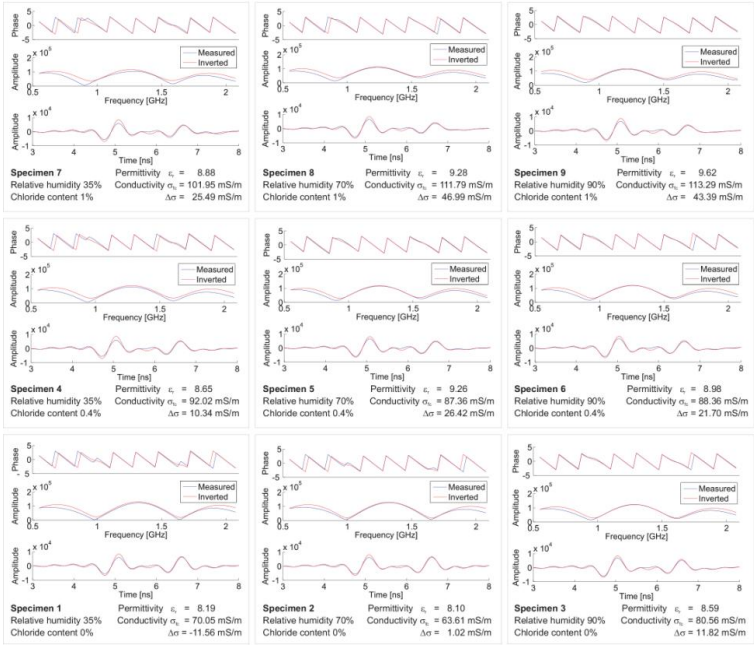

Figure A.7 Overview of all the inversion results using the frequencies between 575 MHz and 2.1 GHz. For each specimen the figure shows the phase (top), and amplitude spectrum (middle) in frequency domain and the signals in time domain (bottom) for the measured (blue) and inverted (red) traces with corresponding inversion results.

$G^{ca}W$. As starting values for the concrete permittivity the average of the starting values and the result of the first step are used. Starting values for σ_{fc} were 50 and 100 mS/m and starting values for $\Delta\sigma$ were 5 and 10 mS/m. The inversion results for these eight starting models return equal or very similar (less than 1% deviation) medium properties of the concrete slab which indicates that the global minimum is found.

The third step optimizes the concrete permittivity and frequency-dependent conductivity $\mathbf{m}_3 = [\varepsilon_r, \sigma_{fc}, \Delta\sigma]$ by minimizing the misfit between the air-concrete and concrete-aluminium reflections and $(G^{ca} + G^{ca})W$. As starting values for the concrete permittivity 0.9, 1.0 and 1.1 times the obtained permittivity of step 2 were used. As starting values for σ_{fc} and $\Delta\sigma$, 0.5, 1.0 and 1.5 times the obtained σ_{fc} and $\Delta\sigma$ values of step 2 were used. The inversion results for all these 27 starting models again return equal or very similar medium properties of the concrete slab, which are very similar to the inversion results obtained in the second step. This indicates that the global minimum is found. Figure A.7 shows for all

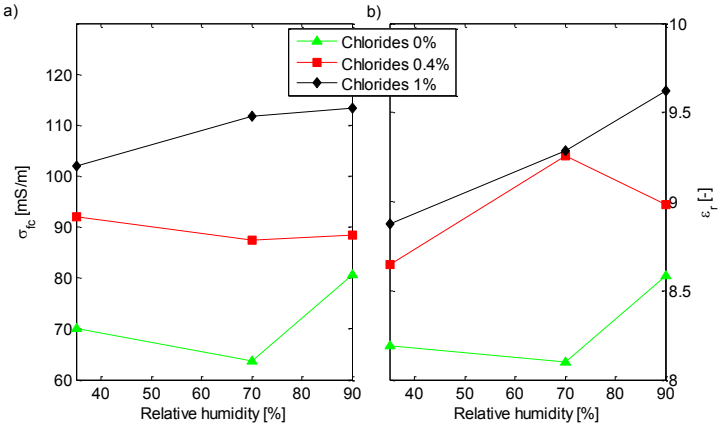

Figure A.8 (a) Inverted conductivity σ_{fc} and (b) permittivity ε_r values as function of the relative humidity for different chloride contents.

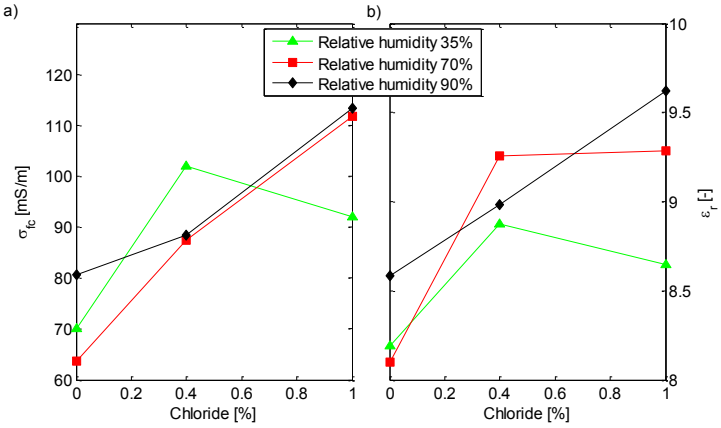

Figure A.9 (a) Inverted conductivity σ_{fc} and (b) permittivity ε_r values as function of the chloride content for different relative humidities.

specimens the measured data in blue and the inverted data in red. The phase and amplitude spectrum in frequency domain are very similar and the fit is optimal around the center frequency f_c = 1.2 GHz. The time domain results clearly show the air-concrete reflection

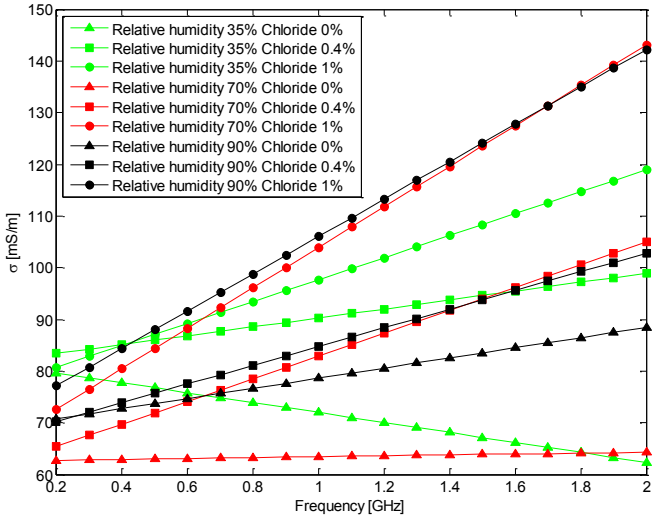

Figure A.10 Inversion results of frequency dependent conductivities of the specimens (see Table 1).

and the concrete-aluminium reflection, which are very similar, although the concrete-aluminium reflection inversion gives a better fit in amplitude and shape than the air-concrete reflection. The clear similarity between the measurements and the inverted data clearly indicate that our inversion results describe the measurements well.

A.6 Full-waveform inversion results

The following discussion will focus on the results of the inversion of both reflections using the 0.575 - 2.1 GHz frequency range since the inversion step of only the concrete-aluminium reflection returned similar results. We will present inversion results by plotting the medium properties as function of the relative humidity and chloride content to investigate their dependency in more detail. Figure A.8a shows that for increasing chloride content larger conductivities are obtained, whereas the relative humidity has little influence on the conductivity values. Figure A.8b shows the obtained relative permittivity as a function of the relative humidity for the different chloride contents. The identical chloride content series show moderately increasing relative permittivity values for increasing relative humidity. Note the slight increase in relative permittivity for increasing humidity compared to the significant increase in conductivity for increasing chloride content.

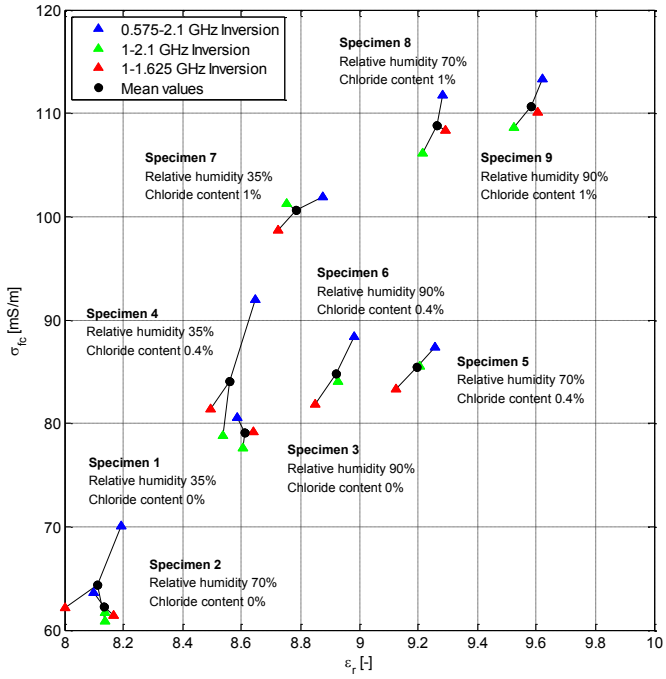

Figure A.11 Inverted relative permittivity and conductivity values of all specimens.

Figure A.9a shows that conductivity is strongly increasing for increasing chloride content and that the slopes are similar for the three different relative humidities. Figure A.9b shows in general an increase of the inverted relative permittivity for increasing chloride content for the different relative humidities. Two outliers could be identified which did not follow the trend; specimen 2 (70% relative humidity and 0% chlorides) and specimen 5 (70% relative humidity and 0.4% chloride). Figure A.10 shows the linear frequency dependent conductivities (A.1) for all inverted specimens (Table A.1). It is observed that the 1% chloride results (circles) have the steepest slopes and the highest conductivity values. Squares (0.4% chlorides) have intermediates slopes and medium σ values. Finally, triangles (0% chlorides) show the lowest slopes with low σ values.

Figure A.11 shows an overview of all the inverted conductivities and relative permittivities for all specimens. The use of three different frequency ranges, indicated by the red, green and blue, provided similar results which show the stability of the full-waveform inversion.

Again, for increasing chloride and humidity an increasing conductivity and permittivity can be observed, respectively. In this way, both relative humidity and chloride content effects can be observed. This figure shows that the chloride content has a more accentuated effect on conductivity values than relative humidity has on relative permittivity. Moreover, increasing chloride content has similar influence as relative humidity on relative dielectric permittivity values. This indicates that chloride content is a more discriminating parameter than relative humidity on electromagnetic wave propagation in concrete.

A.7 Conclusions

A novel full-waveform inversion algorithm is developed for off-ground bistatic GPR horn antennas using all information present in the GPR traces. Using the full-waveform in the inversion enables the estimation of quantitative electromagnetic properties. The horn antenna GPR system is characterized by estimating the phase center and the effective wavelet using measurements over a metal plate. GPR data measured over nine concrete specimens having different moisture and chloride contents are inverted and return a relative dielectric permittivity and a conductivity which include a frequency-dependent component. The full-waveform inversion consists of three consecutive steps. The first inversion step calibrates the time zero using the air-concrete reflection. The second step inverts the permittivity and the frequency-dependent conductivity of the concrete using the concrete-aluminium reflection. The third step inverts the permittivity and the frequency-dependent conductivity of the concrete using the air-concrete and concrete-aluminium reflection and returned similar results as in the second step. In all steps several starting models are used and return equal or very similar results which indicate that the inversion is well constrained. In general, the inversion results show for increasing chloride and humidity content specimen, increasing conductivity and permittivity values, respectively, with the exception of two outliers (specimen 2 and 5). Chloride content has a more accentuated effect on wave propagation than relative humidity and for increasing chloride content increasing frequency-dependent conductivity values are obtained. It was shown that it is possible to discriminate the separate effects of chloride content and relative humidity on both conductivity and relative dielectric permittivity. Future work will focus on concrete specimens containing different chloride gradients and on the electromagnetic wave propagation model implementation for numerous layers to estimate these gradients.

Appendix B

A.8 List of Figures

A.9 List of Tables

Appendix C

A.10 List of Publications

Busch, S., L. Weihermüller, J. A. Huisman, C. M. Steelman, A. L. Endres, H. Vereecken, and J. van der Kruk, 2013, Coupled hydrogeophysical inversion of time-lapse surface GPR data to estimate hydraulic properties of a layered subsurface, Water Resources Research, accepted.

Busch, S., J. van der Kruk, and H. Vereecken, 2012, Improved characterization of fine texture soils using on-ground GPR full-waveform inversion, IEEE Transactions on Geoscience and Remote Sensing, accepted, doi: 10.1109/TGRS.2013.2278297.

Busch, S., J. van der Kruk, J. Bikowski, and H. Vereecken, 2012, Quantitative conductivity and permittivity estimation using full-waveform inversion of on-ground GPR data, Geophysics, 77, H79–H91, doi: 10.1190/GEO2012-0045.1.

Van der Kruk, J., A. Klotzsche, S. Busch, and H. Vereecken, 2012, Neueste Ergebnisse der Dispersionsinversion und Vollen-Wellenfeldinversion von Georadar Daten, DGG Mitteilungen Sonderband I/2012, 77–82, ISSN-Nr. 0947-1944 (2012).

Kalogeropoulos, A., J. van der Kruk, J. Hugenschmidt, S. Busch, and K. Merz, 2011, Chlorides and moisture assessment in concrete by GPR full waveform inversion: Near Surface Geophysics, 9, 277–285.

Conference Proceedings

Van der Kruk, J., A. Klotzsche, A. Mester, S. Busch, G. Meles, J. Bikowski, X. Yang, and H. Vereecken, 2012, Recent developments in quantitative electromagnetic induction and ground penetrating radar inversion, Proceedings of the 5th International Conference on Environmental and Engineering Geophysics, 318–322, ISBN: 978-1-933100-42-5.

Busch, S., J. van der Kruk, J. Bikowski, and H. Vereecken, 2011, Combined effective wavelet estimation and full-waveform inversion of GPR data, 6th International Workshop on Advanced Ground Penetrating Radar (IWAGPR), 5.

Busch, S., J. van der Kruk, J. Bikowski, and H. Vereecken, 2010, Full-waveform inversion of multi-offset surface GPR data, Proceedings of the 13th International Conference on Ground Penetrating Radar (ICGPR), 1–4, doi: 10.1109/ICGPR.2010.5550242.

A.11 International Conferences and Workshops

Contributions as first author

Busch, S., L. Weihermüller, J. A. Huisman, C. M. Steelman, A. L. Endres, H. Vereecken, and J. van der Kruk*, Joint inversion of time-lapse on-ground GPR data to estimate the hydraulic properties of a layered subsurface, Deutsche Geophysikalische Gesellschaft (DGG), Leibzig, , Germany, 04. – 07. March 2013 (Oral).

Busch*, S., J. van der Kruk, J. Bikowski, and H. Vereecken, Characterization of conductive soils using on-ground GPR full-waveform inversion, EGU General Assembly 2012, Vienna, Austria, 22. – 27. April 2012 (Oral).

Busch*, S., J. van der Kruk, J. Bikowski, and H. Vereecken, Improved characterization of silty soils using on-ground GPR full-waveform inversion, 72th Annual Meeting of the Deutsche Geophysikalische Gesellschaft (DGG), Hamburg, Germany, 05. – 08. March 2012 (Oral).

Busch*, S., J. van der Kruk, J. Bikowski, and H. Vereecken, Quantitative permittivity and conductivity estimation using full-waveform inversion of on-ground GPR data, American Geophysical Union (AGU) Fall Meeting 2011, San Francisco, California, USA, 05. – 09. December 2011 (Oral).

Busch*, S., J. van der Kruk, J. Bikowski, and H. Vereecken, Combined effective wavelet estimation and full-waveform inversion of GPR data, 6th International Workshop on Advanced Ground Penetrating Radar (IWAGPR), Aachen, Germany, 22. – 24. June 2011 (Oral).

Busch*, S., J. van der Kruk, J. Bikowski, and H. Vereecken, Combined full-waveform inversion and effective wavelet estimation of on-ground GPR data, 71th Annual Meeting of the Deutsche Geophysikalische Gesellschaft (DGG), Cologne, Germany, 21. – 24. February 2011 (Oral).

Busch, S., J. van der Kruk*, J. Bikowski, and H. Vereecken, Full-waveform inversion of multi-offset surface GPR data, International 13th International Conference on Ground Penetrating Radar (ICGPR), Lecce, Italy, 21. – 25. June 2010 (Oral).

Contributions as co-author

Van der Kruk*, L., A. Klotzsche, S. Busch, X. Yang, J. Bikowski and H. Vereecken, Recent Developments in Full-waveform of GPR Data, SEG-AGU Hydrogeophysics Workshop, Boise, Idaho, USA, 08. – 11. July 2012 (Poster).

Van der Kruk*, J., A. Klotzsche, A. Mester, S. Busch, G. Meles, J. Bikowski, X. Yang, and H. Vereecken, Recent developments in quantitative electromagnetic induction and ground penetrating radar inversion, 5th International Conference on Environmental and Engineering Geophysics (ICEEG), Changsha, China, 16. – 18. June 2012 (Oral).

Van der Kruk*, J., A. Klotzsche, A. Mester, S. Busch, G. Meles, and H. Vereecken, High resolution electromagnetic hydrogeophysical imaging, Sixteenth International Water Technology Conference (IWTC), Istanbul, Turkey, 07. – 15. May 2012 (Oral).

Endres*, A. L., C. Steelman, L. Jones, S. Busch, and J. van der Kruk, Evaluating soil moisture dynamics using high frequency Ground-Penetrating Radar, American Geophysical Union (AGU) Fall Meeting 2011, San Francisco, California, USA, 05. – 09. December 2011 (Oral).

Van der Kruk*, J., A. Kalogeropoulos, J. Hugenschmidt, S. Busch, and K. Merz, Full-waveform inversion of ground penetrating radar data to assess chloride and moisture content in concrete, EGU General Assembly 2011, Vienna, Austria, 03. – 08. April 2011 (Oral).

Klotzsche*, A., S. Busch*, X. Yang*, and J. van der Kruk, Full-waveform inversion for hydrogeophysical applications: state of the science, Advancing Hydrogeophysics, Hornberg, Germany, 25. – 27. February 2011 (Oral).

A.12 About the Author

Sebastian Busch was born in Mülheim an der Ruhr, Germany on 22. January 1982. In 2009 he received the Master of Science degree in Geosciences with focus on Geophysics from the Ruhr-Universität Bochum, Germany. He realized his master thesis in relation to the application of near-surface refraction and reflection seismics and ground-penetrating radar on different test sites, supervised by Professor Wolfgang Friederich. In 2009 he started his PhD in hydrogeophysics at the Forschungszentrum Jülich, "Institute of Bio- and Geosciences", Agrosphere (IBG-3), Jülich, Germany, in collaboration with the "Fakultät für Georessourcen und Materialtechnik" of the Rheinisch-Westfälische Technische Hochschule (RWTH) Aachen, Germany, under the supervision of Professor Jan van der Kruk. He obtained three years PhD research grant funded by Forschungszentrum Jülich where he was a team member of the "Hydrogeophysical Imaging and Characterization" group. His research activity concerns the quantitative GPR imaging using surface GPR full-waveform inversion. In 2011 he followed two month training at the Department of "Earth and Environmental Sciences" at the University of Waterloo, Ontario, Canada. Supervised by Professor Anthony L. Endres, this project aimed the application of a novel coupled hydrogeophysical inversion of time-lapse surface GPR data to estimate the hydraulic properties of a layered subsurface.

Bibliography

Abdu, H., D. A. Robinson, and S. B. Jones, 2007, Comparing bulk soil electrical conductivity determination using the DUALEM-1S and EM38-DD electromagnetic induction instruments, Soil Science Society of America Journal, 71, 189–196.

Annan A. P., 2005, Ground Penetrating Radar, in Near-Surface Geophysics, edited by D. K. Butler, Chapter 11, 357-438, Society of Exploration Geophysicists, Tulsa, Okla.

Annan, A. P., 1973, Radio interferometry depth sounding. 1. Theoretical discussion, Geophysics, 38, 3, 557–580.

Annan, A. P., W. M. Waller, D. W. Strangway, J. R. Rossiter, J. D. Redman, and R. D. Watts, 1975, The electromagnetic response of a low-loss, 2-layer, dielectric earth for horizontal electric dipole excitation, Geophysics, 40, 285–298.

Bano, M., 2004, Modelling of GPR waves for lossy media obeying a complex power law of frequency for dielectric permittivity, Geophysical Prospecting, 37, 11–26.

Bauer, J., L. Weihermüller, J. A. Huisman, M. Herbst, A. Graf, J. M. Sequaris, and H. Vereecken, 2012, Inverse determination of heterotrophic soil respiration response to temperature and water content under field conditions, Biogeochemistry, 108, 119–13.

Behaegel, M., P. Sailhac, and G. Marquis, 2007, On the use of surface and ground temperature data to recover soil water content information, Journal of Applied Geophysics, 62, 234–243.

Ben-Hadj-Ali, H., S. Operto, and J. Virieux, 2011, An efficient frequency-domain full waveform inversion method using simultaneous encoded sources, Geophysics, 76, 4, R109–R124.

Binley, A., P. Winship, and R. Middleton, 2001, High-resolution characterization of vadose zone dynamics using cross-borehole radar, Water Resources Research, 37, 11, 2639–2652.

Bohidar, R. N., and J. F. Hermance, 2002, The GPR refraction method, Geophysics, 67, no. 5, 1474–1485.

Böhni, H., 2005, Corrosion in reinforced concrete structures. CRC Press, Woodhead publishing ltd.

Borchers, B., T. Uram, and J. M. H. Hendrickx, 1997, Tikhonov regularization of electrical conductivity depth profiles in field soils, Soil Science Society of America Journal, 61, 1004–1009.

Bradford, J. H., 2008, Measuring water content heterogeneity using multifold GPR with reflection tomography, Vadose Zone Journal, 7, 184–193.

Brooks, R. H., and A. T. Corey, 1966, Properties of porous media affecting fluid flow, Journal of the Irrigation and Drainage Division, ASCE Proc. 72(IR2), 61–88.

Brossier, R., S. Operto, and J. Virieux, 2009, Seismic imaging of complex onshore structures by 2D elastic frequency-domain full-waveform inversion, Geophysics, 74, 6, WCC105–WCC118.

Buchner, J., U. Wollschläger, and K. Roth, 2012, Inverting surface GPR data using FDTD simulation and automatic detection of reflections to estimate subsurface water content and geometry, Geophysics, 77, H45–H55.

Busch, S., J. van der Kruk, J. Bikowski, and H. Vereecken, 2012, Quantitative conductivity and permittivity estimation using full-waveform inversion of on-ground GPR data, Geophysics, 77, H79–H91, doi: 10.1190/GEO2012-0045.1.

Conciatori, D., 2005, Effet du microclimat sur l'initiation de la corrosion des aciers d'armature dans les ouvrages en béton armé. Thèse N° 3408, Ecole Polytechnique Fédérale de Lausanne.

Crase, E., A. Pica, M. Noble, J. McDonald, and A. Tarantola, 1990, Robust elastic nonlinear wave-form inversion - Application to Real Data, Geophysics, 55, 5, 527–538.

Crocco, L., and F. Soldovieri, 2003, GPR prospecting in a layered medium via microwave tomography, Annals of Geophysics, 46, 559–572.

Davis, J. L., and A. P. Annan, 1989, Ground-penetrating radar for high-resolution mapping of soil and rock stratigraphy, Geophysical Prospecting, 37, 531–551.

de Hoop, A. T., Handbook of radiation and scattering of waves, Academic Press, Amsterdam, 1995.

Derobert, X., J. Iaquinta, G. Klysz, and J.-P. Balayssac, 2008, Use of capacitive and GPR techniques for the non-destructive evaluation of cover concrete, NDT & E International, 41, 44–52.

Duan, Q. Y., S. Sorooshian, and V. Gupta, 1992, Effective and efficient global optimization for conceptual rainfall-runoff models, Water Resources Research, 28, 1015–1031.

Endres, A. L., W. P. Clement, and D. L. Rudolph, 2000, Ground penetrating radar imaging of an aquifer during a pumping test , Ground Water, 38, 566–576.

Engheta, N., C. H. Papas, and C. Elachi, 1982, Radiation patterns of interfacial dipole antennas, Radio Science, 17, 1557–1566.

Ernst, J. R., A. G. Green, H. Maurer, and K. Holliger, 2007a, Application of a new 2D time-domain full-waveform inversion scheme to crosshole radar data, Geophysics, 72, J53–J64.

Ernst, J. R., A. G. Green, H. Maurer, and K. Holliger, 2007b. Full-waveform inversion of cross-hole radar data based on 2-D finite difference time domain solutions of Maxwell's equations, IEEE Transactions on Geoscience and Remote Sensing, 45, 2807–2828.

Ersahin, S., and A. R. Brohi, 2006, Spatial variation of soil water content in topsoil and subsoil of a Typic Ustifluvent, Agricultural Water Management, 83, 79–86.

Feddes, R. A., E. Bresler, and S. P. Neuman, 1974, Field test of a modified numerical model for water uptake by root systems, Water Resources Research, 10, 1199–1206.

Ferré, T., Bentley, L., Binley, A., Linde, N., Kemna, A., Singha, K., Holliger, K., Huisman, J. A., and V. Minsley, 2009, Critical steps for the continuing advancement of hydrogeophysics, Eos, 90, 23.

Galagedara, L. W., G. W. Parkin, and J. D. Redman, 2003, An analysis of the ground-penetrating radar direct ground wave method for soil water content measurement, Hydrological Processes, 17, 3615–3628.

Galagedara, L. W., G. W. Parkin, J. D. Redman, P. von Bertoldi, and A. L. Endres, 2005a, Field studies of the GPR ground wave method for estimating soil water content during irrigation and drainage, Journal of hydrology, 301, 182–197.

Galagedara, L. W., J. D. Redman, G. W. Parkin, A. P. Annan, and A. L. Endres, 2005b, Numerical modeling of GPR to determine the direct ground wave sampling depth, Vadose Zone Journal, 4, 1096–1106.

Garambois, S., P. Senechal, and H. Perroud, 2002, On the use of combined geophysical methods to assess water content and water conductivity of near-surface formations, Journal of Hydrology, 259, 32–48.

Gaskin, G. J., and J. D. Miller, 1996, Measurement of soil water content using a simplified impedance measuring technique, J. agric. Engng Res., 63, 153–160.

Gauthier, O., J. Virieux, and A. Tarantola, 1986, Two-dimensional nonlinear inversion of seismic wave-forms - Numerical Results, Geophysics, 51, 7, 1387–1403.

Gebbers, R., E. Lücke, M. Dabas, and H. Domsch, 2009, Comparison of instruments for geoelectrical soil mapping at the field scale, Near Surface Geophysics, 7, 179–190.

Geotomo Software, Manual RES2DINV, http://www.geotomosoft.com.

Gerhards, H., U. Wollschläger, Q. Yu, P. Schiwek, X. Pan, and K. Roth, 2008, Continuous and simultaneous measurement of reflector depth and average soil-water content with multichannel ground-penetrating radar, Geophysics, 4, J15–J23.

Goss, K.-U., and M. Madliger, 2007, Estimation of water transport based on in situ measurements of relative humidity and temperature in a dry Tanzanian soil, Water Resources Research, 43, W05433.

Greaves, R. J., D. P. Lesmes, J. M. Lee, and M. N. Toksoz, 1996, Velocity variations and water content estimated from multi-offset, ground-penetrating radar, Geophysics, 61, no. 3, 683–695.

Greco, R., 2006, Soil water content inverse profiling from single TDR waveform, Journal of Hydrology, 317, pp. 325–339.

Greco, R., and A. Guida, 2008, Field measurements of topsoil moisture profiles by vertical TDR probes, Journal of Hydrology, 348, pp. 442–451.

Heimovaara, T. J., J. A. Huisman, J. A. Vrugt, and W. Bouten, 2004, Obtaining the spatial distribution of water content along a TDR probe using the SCEMUA bayesian inverse modeling scheme, Vadose Zone Journal, 3, pp. 1128–1145.

Hendrickx, J. M. H., B. Bochers, D. L. Corwin, S. M. Lesch, A. C. Hilgendorf, and J. Schlue, 2002, Inversion of soil conductivity profiles from electromagnetic induction measurements, Theory and experimental verification, Soil Science Society of America Journal, 66, 673–685.

Hinnell, A. C., T. P. A. Ferré, J. A. Vrugt, J. A. Huisman, S. Moysey, J. Rings, and M. B. Kowalsky, 2010, Improved extraction of hydrologic information from geophysical data through coupled hydrogeophysical inversion, Water Resources Research, 46, WW00D40.

Hu, W., A. Abubakar, and T. M. Habashy, 2009, Simultaneous multifrequency inversion of full-waveform seismic data, Geophysics, 74, 2, R1–R14.

Hugenschmidt, J., 2002, Concrete bridge inspection with a mobile GPR system, Construction and Building Materials, 16, 147–154.

Hugenschmidt, J., and R. Loser, 2007, Detection of chlorides and moisture in concrete structures with ground penetrating radar, Materials and Structures, 41, 785–792.

Hugenschmidt, J., and R. Mastrangelo, 2006, GPR inspection of concrete bridges, cement and concrete composites, Non-Destructive Testing, 28, 384–392.

Huisman, J. A., S. S. Hubbard, J. D. Redman, and A. P. Annan, 2003, Measuring soil water content with Ground Penetrating Radar, A review, Vadose Zone Journal, 2, 476–491.

Jacob, R. W., and J. F. Hermance, 2004, Assessing the precision of GPR velocity and vertical two-way travel time estimates, Journal of Environmental and Engineering Geophysics, 9, 143–153.

Jadoon, K. Z., S. Lambot, B. Scharnagl, J. van der Kruk, E. Slob, and H. Vereecken, 2012, Quantifying field-scale surface soil water content from proximal GPR signal inversion in the time domain, Near Surface Geophysics, 8, 483–491.

Jiao, Y., G.A. McMechan, and E. Pettinelli, 2000, In situ 2-D and 3-D measurements of radiation patterns of half-wave dipole GPR antennas, Journal of Applied Geophysics, 43, 69–89.

Kalogeropoulos, A., J. van der Kruk, J. Hugenschmidt, S. Busch, and K. Merz, 2011 Chlorides and moisture assessment in concrete by GPR full waveform inversion, Near Surface Geophysics, 9, 277–285.

Klotzsche, A., J. van der Kruk, G. A. Meles, J. Doetsch, H. Maurer, and N. Linde, 2010, Full-waveform inversion of cross-hole ground-penetrating radar data to characterize a gravel aquifer close to the Thur River, Switzerland, Near Surface Geophysics, 8, 635–649.

Klotzsche, A., J. van der Kruk, G.A. Meles, and H. Vereecken, 2012, Crosshole GPR full-waveform inversion of waveguides acting as preferential flow paths within aquifer systems, Geophysics, 4, H57–2H62.

Klysz, G., and J.-P. Balayssac, 2007, Determination of volumetric water content of concrete using ground-penetrating radar, Cement and Concrete Research, 37, 1164–1171.

Kool, J.B., and J.C. Parker, 1988, Analysis of the inverse problem for transient unsaturated soil water flow, Water Resources Research, 24, 817–830.

Kowalsky, M. B., S. Finsterle, J. Peterson, S. Hubbard, Y. Rubin, E. Majer, A. Ward, and G. Gee, 2005, Estimation of field-scale soil hydraulic and dielectric parameters through joint inversion of GPR and hydrological data, Water Resources Research, 41, W11425.

Kuroda, S., H. Jiang, and H. J. Kim, 2009, Time-lapse borehole radar monitoring of an infiltration experiment in the vadose zone, Journal of Applied Geophysics, 4, 361–366.

Lagarias, J. C., J. A. Reeds, M. H. Wright, and P. E. Wright, 1998, Convergence properties of the Nelder-Mead simplex method in low dimensions, Siam Journal on Optimization, 9, 112–147.

Lambot, S, E. C. Slob, J. Rhebergen, O. Lopera, K. Z. Jadoon, and H. Vereecken, 2009, Remote estimation of the hydraulic properties of a sand using full-waveform integrated hydrogeophysical inversion of time lapse, off-ground GPR data, Vadose Zone Journal, 8, 743–754.

Lambot, S., E. C. Slob, I. van den Bosch, B. Stockbroeckx, and M. Vanclooster, 2004c, Modeling of Ground-Penetrating Radar for accurate characterization of subsurface electric properties, IEEE Transactions on Geosciences and Remote Sensing, 42, 2555–2568.

Lambot, S., E. C. Slob, I. van den Bosch, B. Stockbroeckx, B. Scheers, and M. Vanclooster, 2004b, Estimating soil electric properties from monostatic ground-penetrating radar signal inversion in the frequency domain, Water Resources Research, 40, W04205.

Lambot, S., E. C. Slob, M. Vanclooster, and H. Vereecken, 2006b, Closed loop GPR data inversion for soil hydraulic and electric property determination, Geophysical Research Letters, 33, L21405.

Lambot, S., I. van den Bosch, B. Stockbroeckx, P. Druyts, M. Vanclooster, and E. C. Slob, 2005, Frequency dependence of the soil electromagnetic properties derived from ground-penetrating radar signal inversion, Subsurface Sensing Technologies and Applications, 6, 73–87.

Lambot, S., J. Rhebergen, I. van den Bosch, E. C. Slob, and M. Vanclooster, 2004a, Measuring the soil water content profile of a sandy soil with off-ground monostatic ground penetrating radar, Vadose Zone Journal, 3, 1063–1071.

Lambot, S., L. Weihermüller, J.A. Huisman, H. Vereecken, M. Vanclooster, and E.C. Slob, 2006c, Analysis of air-launched ground-penetrating radar techniques to measure the soil surface water content, Water Resources Research, 42, W11403.

Lambot, S., M. Antoine, M. Vanclooster, and E.C. Slob, 2006a, Effect of soil roughness on the inversion of off-ground monostatic GPR signal for noninvasive quantification of soil properties, Water Resources Research, 42, doi:10.1029/2005WR004416.

Lavoué, F., J. van der Kruk, J. Rings, F. André, D. Moghadas, L. A. Huisman, S. Lambot, L. Weihermüller, J. Vanderborght, and H. Vereecken, 2010, Electromagnetic induction calibration using apparent electrical conductivity modelling based on electrical resistivity tomography, Near Surface Geophysics, 8, 553–561.

Leidenberger, P., B. Oswald, and K. Roth, 2006, Efficient reconstruction of dispersive dielectric profiles using time domain reflectometry (TDR), Hydrology and Earth System Sciences, 10, pp. 209–232.

Lenormand, R., 1990, Liquids in porous media, Journal of Physics: Condensed Matter, 2, SA79–SA88.

Loeffler, O., and M. Bano, 2004, GPR measurements in a controlled vadose zone: Influence of the water content, Vadose Zone Journal, 3, 1082–1092.

Looms, M. C., A. Binley, K. H. Jensen, L. Nielsen, and T. M. Hansen, 2008, Identifying unsaturated hydraulic parameters using an integrated data fusion approach on cross-borehole geophysical data, Vadose Zone Journal, 7, 238–248.

Mboh, C. M., J. A, Huisman, and H. Vereecken, 2011, Feasibility of sequential and coupled inversion of time domain reflectometry data to infer soil hydraulic parameters under falling head infiltration, Soil Science Society of America Journal, 75, 775–786.

Meles, G. A., J. van der Kruk, S. A. Greenhalgh, J. R. Ernst, H. Maurer, and A. G. Green, 2010, A new vector waveform inversion algorithm for simultaneous updating of conductivity and permittivity parameters from combination Crosshole/Borehole-to-Surface GPR data, IEEE Transactions on Geoscience and Remote Sensing, 48, 3391–3407.

Mester, A., J. van der Kruk, E. Zimmerman, and H. Vereecken, 2011, Quantitative two-layer conductivity inversion of multi-configuration electromagnetic induction measurements, Vadose Zone Journal, 10, 1–12.

Mora, P., 1987, Nonlinear two-dimensional elastic inversion of multioffset seismic data, Geophysics, 52, 9, 1211–1228.

Mualem, Y., 1976, A new model for predicting the hydraulic of unsaturated porous media, Water Resources Research, 12, 513–522.

Noon, D. A., G. F. Stickley, and D. Longstaff, 1998, A frequency-independent characterisation of GPR penetration and resolution performance, Journal of Applied Geophysics, 40, 127–137.

Pan, X., U. Wollschläger, and K. Roth, 2012, Optimization of multi-channel ground-penetrating radar for quantifying field-scale soil water dynamics, Journal of Applied Geophysics, 82, 101–109.

Peters, A., and W. Durner, 2008, A simple model for describing hydraulic conductivity in unsaturated porous media accounting for film and capillary flow, Water Resources Research, 44, W11417.

Peters, A., and W. Durner, 2010, Reply to comment by N. Shokri and D. Or on "A simple model for describing hydraulic conductivity in unsaturated porous media accounting for film and capillary flow", Water Resources Research, 46, W06802.

Pratt, R. G., 1990a, Frequency-domain elastic wave modeling by finite-differences - A tool for crosshole seismic imaging, Geophysics, 55, 5, 626–632.

Pratt, R. G., 1990b, Inverse-theory applied to multisource cross-hole tomography. 2. Elastic wave-equation method, Geophysical Prospecting, 38, 311–329.

Pratt, R. G., 1999, Seismic waveform inversion in the frequency domain, Part 1: Theory and verification in a physical scale model, Geophysics, 64, 3, 888–901.

Pratt, R. G., and M. H. Worthington, 1990, Inverse-Theory Applied to multisource cross-hole tomography. 1. Acoustic wave-equation method, Geophysical Prospecting, 38, 287–310.

Radzevicius, S.J. and J. J. Daniels, 2000, GPR H-plane antenna patterns for a horizontal dipole on a halfspace interface, in Proceedings of the Eighth International Conference on Ground-Penetrating Radar, Gold Coast, Australia, 712–717.

Ramirez, A., W. Daily, D. LaBrecque, E. Owen, and D. Chesnut, 1993, Monitoring an underground steam injection process using electrical resistance tomography, Water Resources Research, 29, no. 1, 73–87.

Redman, J.D., J. L. Davis, L. W. Galagedara, and G. W. Parkin, 2002, Field studies of GPR air lunched surface reflectivity measurements of soil water content, in Proceedings of the Nineth Conference of Ground-Penetrating Radar. Proc. SPIE 4758, pp, 156–161.

Rhoades, J. D., P. A. C. Raats, and R. J. Prather, 1976, Effects of liquid phase electrical conductivity, water content, and surface conductivity on bulk soil electrical conductivity, Soil Science Society of America Journal, 40, 651–655.

Robert, A., 1998, Dielectric permittivity of concrete between 50 MHz and 1 GHz and GPR measurements for building materials evaluation, Journal of Applied Geophysics, 40, 89–94.

Robinson, D. A., C. M. K. Gardner, and J. D. Cooper, 1999, Measurement of relative permittivity in sandy soils using TDR, capacitance and theta probes, comparison, including the effects of bulk soil electrical conductivity, Journal of Hydrology, 223, 198–211.

Robinson, D. A., S. B. Jones, J. M. Wraith, D. Or, and S. P. Friedman, 2003, A review of advances in dielectric and electrical conductivity measurement in soils using time domain reflectometry, Vadose Zone Journal, 2, 44–475.

Rucker, D., and P. A. Ferré, 2004, Parameter Estimation for soil hydraulic properties using zero-offset borehole radar: Analytical method, Soil Science Society of America Journal, 68, 1560–1567.

Saarenketo, T., and T. Scullion, 2000, Road evaluation with ground penetrating radar, Journal of Applied Geophysics, 43, 119–138.

Saey, T., D. Simpson, K. Vermeersch, L. Cockx, and M. Van Meirvenne, 2009, Comparing the EM38DD and DUALEM-21S sensors for depth-to-clay mapping, Soil Science Society of America Journal, 73, 7–12.

Saito, H., J. Šimůnek, and, B. P. Mohanty, 2006, Numerical analysis of coupled water, vapor, and heat transport in the vadose zone, Vadose Zone Journal, 5, no. 2, 784-800, doi: 10.2136/vzj2006.0007.

Sarani, N., and P. Afrasjab, 2012, Effect of soil texture on moisture measurement accuracy with Theta probe ML2 in Sistan region, International Conference on Chemical, Ecology and Environmental Sciences, 114–117.

Sbartai, Z. M., S. Laurens, J.-B. Balayssac, G. Arliguie, and G. Ballivy, 2006, Ability of the direct wave of radar ground-coupled antenna for NDT of concrete structures, NDT & E International, 39, 400–407.

Sensors & Software Inc, Subsurface Views, www.sensoft.ca, vol. 6, no. 23, July 2010.

Shin, C., and Y. G. Cha, 2008, Waveform inversion in the Laplace-domain, Geophysical Journal International, 173, 922–931.

Šimůnek, J., M. Sejna, and M. T. Van Genuchten, 2008, Code for simulating the one-dimensional movement of water, heat, and multiple solutes in variably saturated porous media, PC-Progress, Prague, Czech Republic.

Slob, E., and J. Fokkema, 2002, Coupling effects of two electric dipoles on an interface, Radio Science, 37, 1073.

Slob, E., M. Sato, and G. Olhoeft, 2010, Surface and borehole ground-penetrating-radar developments, Geophysics, 75, 75A103–75A120.

Smith, G. S., 1984, Directive properties of antennas for transmission into a material half-space, IEEE Transactions on Antennas and Propagation, 32, 232–246.

Soutsos, M. N., J. H. Bungey, S. G. Millard, M. R. Shaw, and A. Patterson, 2001, Dielectric properties of concrete and their influence on radar testing, NDT&E International, 34, 419–425.

Steelman, C. M., A. L. Endres, and J. P. Jones, 2012, High-resolution ground-penetrating radar monitoring of soil moisture dynamics: Field results, interpretation, and comparison with unsaturated flow model, Water resources Research, 48, W09538.

Steelman, C. M., and A. L. Endres, 2010, An examination of direct ground wave soil moisture monitoring over an annual cycle of soil conditions, Water Resources Research, 46, W11533.

Steenpass, C., J. Vanderborght, M. Herbst, J. Šimůnek, and H. Vereecken, 2010, Estimating soil hydraulic properties from infrared measurements of soil surface temperatures and TDR data, Vadose Zone Journal, 9, no. 4, 910-924, doi: 10.2136/vzj2009.0176.

Streich, R., and J. van der Kruk, 2007a, Accurate imaging of multicomponent GPR data based on exact radiation patterns, IEEE Transactions on Geoscience and Remote Sensing, 45, 93–103.

Streich, R., and J. van der Kruk, 2007b, Characterizing a GPR antenna system by near-field measurements, Geophysics, 72, no 5, A51–A55.

Sudduth, K. A., S. T. Drummond, and N. R. Kitchen, 2001, Accuracy issues in electromagnetic sensing of soil electrical conductivity for precision agriculture, Computers and Electronics in Agriculture, 31, 239–264.

Tabbagh, A., C. Camerlynck, and P. Cosenza, 2000, Numerical modeling for investigating the physical meaning of the relationship between relative dielectric permittivity and water content of soils, Water Resources Research, 36, 2771–2776.

Tarantola, A., 1984a, Inversion of seismic-reflection data in the acoustic approximation, Geophysics, 49, 8, 1259–1266.

Tarantola, A., 1984b, Linearized inversion of seismic-reflection data, Geophysical Prospecting, 32, 998–1015.

Tillard, S., and J. C. Dubois, 1995, Analysis of GPR data - Wave-propagation velocity determination, Journal of Applied Geophysics, 33, 77–91.

Toledo, P., R. Novy, H. Davis, and L. Scriven, 1990, Hydraulic conductivity of porous media at low water content, Soil Science Society of America Journal, 54, 673–679.

Topp, G. C., J. L. Davis, and A. P. Annan, 1980, Electromagnetic determination of soil water content, Measurements in coaxial transmission lines, Water Resources Research, 16, 574–582.

Triantafilis, J., G. M. Laslett, and A. B. McBratney, 2000, Calibrating an electromagnetic induction instrument to measure salinity in soil under irrigated cotton, Soil Science Society of America Journal, 64, 1009–1017.

Tuller, M., and D. Or, 2005, Water films and scaling of soil characteristic curves at low water contents, Water Resources Research, 41,W09403, doi:10.1029/2005WR004142.

van der Kruk, J., 2001, Three-dimensional imaging of multicomponent ground penetrating radar data, Ph.D. thesis, Delft University of Technology.

van der Kruk, J., and E. C. Slob, 2002, Effective source wavelet determination, Proceedings Ninth international conference on Ground Penetrating Radar, Expanded Abstracts, 144–149.

van der Kruk, J., C. P. A. Wapenaar, J. T. Fokkema, and P. M. van den Berg, 2003, Improved three-dimensional image reconstruction technique for multi-component Ground Penetrating Radar data, Subsurface Sensing Technologies and Applications, 4, 61–99.

van der Kruk, J., R. Streich, and A. G. Green, 2006, Properties of surface waveguides derived from separate and joint inversion of dispersive TE and TM GPR data, Geophysics, 71, 1, K19–K29.

van Genuchten, M. T., 1980, A closed-form equation for predicting the hydraulic conductivity of unsaturated soils, Soil Science Society of America Journal, 44, 892–898.

van Overmeeren, R. A., S. V. Sariowan, and J. C. Gehrels, 1997, Ground penetrating radar for determining volumetric soil water content; Results of comparative measurements at two test sites, Journal of Hydrology, 197, 316–338.

Vanderborght, J., A. Graf, C. Steenpass, B. Scharnagl, N. Prolingheuer, M. Herbst, H. J. Hendricks Franssen, and H. Vereecken, 2010, Within-field variability of bare soil evaporation derived from eddy covariance measurements, Vadose Zone Journal, 9, 943–954.

Virieux, J., and S. Operto, 2009, An overview of full-waveform inversion in exploration geophysics, Geophysics, 74, 6, WCC1–WCC26.

Weihermüller, L., J. S. Huisman, S. Lambot, M. Herbst, and H. Vereecken, 2007, Mapping the spatial variation of soil water content at the field scale with different ground penetrating radar techniques, Journal of Hydrology, 340, 205–216.

Wharton, R. P., G. A. Hazen, R. N. Rau, and D. L. Best, 1980, Electromagnetic propagation logging: advances in technique and interpretation, SPE Paper 9267.

Wollschläger, U., T. Pfaff, and K. Roth, 2009, Field-scale apparent hydraulic parameterisation obtained from TDR time series and inverse modelling, Hydrology and Earth System Sciences, 13, 1953–1966.

Wu, Z., and C. Liu, 1999, An Image Reconstruction Method Using GPR Data, IEEE Transactions on Geoscience and Remote Sensing, 37, 327–335.

Yetton, M. D., 2002, Paleoseismic investigation of the north and west Wairau sections of the Alpine Fault, South Island, New Zealand, Earthquake Commission, Wellington, New Zealand, Earthquake Comm., Res. Rep. 99/353.

Yilmaz, O., 1987, Seismic data processing, Society of Exploration Geophysicists, Tulsa, Okla.

Zhou, Q. Z., J. Shimada, and A. Sato, 2001, Three-dimensional spatial and temporal monitoring of soil water content using electrical resistivity tomography, Water Resources Research, 37, no. 2, 273–285.

Acknowledgement

This research was funded by the Forschungszentrum Jülich (FZJ, Germany) through the Research Group "Hydrogeophysical Imaging and Characterization" of the Agrosphere Institute (IBG-3). By that time, I have worked with a great number of people whose contribution in assorted ways to the research and the making of the thesis deserved special mention.

First and foremost, I would like to express my gratitude to Prof. Dr. Jan van der Kruk, whose encouragements, guidance and support from the initial to the final level. Further, I would like to show my gratitude to Prof. Dr. Harry Vereecken, Head of the IBG-3, for support, excellent conditions, and pleasant working environment at Forschungszentrum Jülich.

I am grateful for collaborating with Dr. Jutta Bikowski during my research period in FZJ. I benefited from her advices, guidance and support for realizing my thesis.

It is a pleasure to thank Prof. Dr. Anthony L. Endres for welcoming me at the Department of “Earth and Environmental Sciences” at the University of Waterloo, Ontario, Canada, during the period October-December 2011. He deserves my gratitude and thanks for giving me access to his experimental facilities, as well as for his constructive ideas.

I wish to further express my thanks to my co-authors Prof. Dr. Jan van der Kruk, Prof. Dr. Harry Vereecken, Dr. Jutta Bikowski, Dr. Lutz Weihermüller, Prof. Dr. Johann A. Huisman, Dr. Colby M. Steelman and Prof. Dr. Anthony L. Endres as well as my examiners for their support, constructive comments and criticism in realizing this research project.

I’m deeply indebted to my parents and my sister. Without their constant support, kindness and endless love over the years, I would never have been able to complete my dissertation. I want to reserve special words of gratitude to Xinxin Li. She deserves all my heartfelt thanks for her love and understanding, endless patience and encouragement when it was most required.

Last but not least, my apologies to all those who I forgot to mention…

Band / Volume 189
Entwicklung und Herstellung von metallgestützten Festelektrolyt-Brennstoffzellen (MSC-SOFC) mit einem Sol-Gel-Elektrolyten
S. D. Vieweger (2013), xviii, 176 pp
ISBN: 978-3-89336-904-1

Band / Volume 190
Mobile Brenngaserzeugungssysteme mit Mitteldestillaten für Hochtemperatur-PEFC
C. Wiethege (2013), iii, 179 pp
ISBN: 978-3-89336-905-8

Band / Volume 191
Verbundvorhaben Öko-effiziente Flugzeugsysteme für die nächste Generation (EFFESYS) - Teilprojekt Brennstoffzelle, Infrastruktur, Komponenten und System (BRINKS) – Schlussbericht
J. Pasel, R.C. Samsun, H. Janßen, W. Lehnert, R. Peters, D. Stolten (2013), xii, 152 pp
ISBN: 978-3-89336-908-9

Band / Volume 192
Analyse des Betriebsverhaltens von Hochtemperatur-Polymerelektrolyt-Brennstoffzellen
L. Lüke (2013), 150 pp
ISBN: 978-3-89336-909-6

Band / Volume 193
Full-waveform inversion of crosshole GPR data for hydrogeological applications
A. Klotzsche (2013), X, 164 pp
ISBN: 978-3-89336-915-7

Band / Volume 194
Long Term Stability and Permeability of Mixed Ion Conducting Membranes under Oxyfuel Conditions
X. Li (2013), III, 143 pp
ISBN: 978-3-89336-916-4

Band / Volume 195
Innovative Beschichtungs- und Charakterisierungsmethoden für die nasschemische Herstellung von asymmetrischen Gastrennmembranen auf Basis von SiO_2
J. Hoffmann (2013), V, 152 pp
ISBN: 978-3-89336-917-1

Band / Volume 196
**Aerosol processes in the Planetary Boundary Layer:
High resolution Aerosol Mass Spectrometry on a Zeppelin NT Airship**
F. Rubach (2013), iii, 141 pp
ISBN: 978-3-89336-918-8

Band / Volume 197
**Institute of Energy and Climate Research
IEK-6: Nuclear Waste Management - Report 2011 / 2012
Material Science for Nuclear Waste Management**
M. Klinkenberg, S. Neumeier, D. Bosbach (Eds.) (2013), 195 pp
ISBN: 978-3-89336-980-1

Band / Volume 198
Material migration in tokamak plasmas with a three-dimensional boundary
R. Laengner (2013), vi, 140, XVII pp
ISBN: 978-3-89336-924-9

Band / Volume 199
Improved characterization of river-aquifer interactions through data assimilation with the Ensemble Kalman Filter
W. Kurtz (2013), xxv, 125 pp
ISBN: 978-3-89336-925-6

Band / Volume 200
Innovative SANEX process for trivalent actinides separation from PUREX raffinate
A. Sypula (2013), 220 pp
ISBN: 978-3-89336-927-0

Band / Volume 201
Transport and deposition of functionalized multi-walled carbon nanotubes in porous media
D. Kasel (2013), VI, 103 pp
ISBN: 978-3-89336-929-4

Band / Volume 202
Full-waveform inversion of surface ground penetrating radar data and coupled hydrogeophysical inversion for soil hydraulic property estimation
S. Busch (2013), X, 110 pp
ISBN: 978-3-89336-930-0

Weitere ***Schriften des Verlags im Forschungszentrum Jülich*** unter
http://wwwzb1.fz-juelich.de/verlagextern1/index.asp

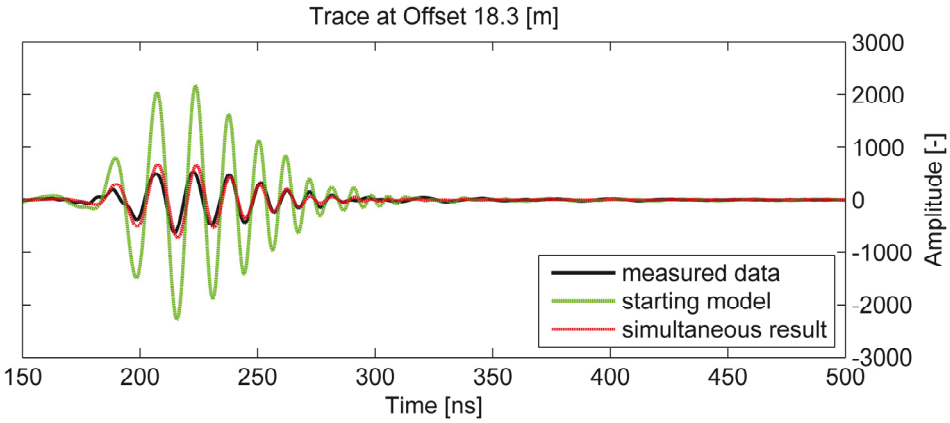

Energie & Umwelt / Energy & Environment
Band / Volume 202
ISBN 978-3-89336-930-0

JÜLICH
FORSCHUNGSZENTRUM